

Copyright

by

John Thomas Tencer

2013

**The Dissertation Committee for John Thomas Tencer Certifies that this is the  
approved version of the following dissertation:**

**Error Analysis for Radiation Transport**

**Committee:**

---

John R. Howell, Supervisor

---

Ofodike Ezekoye

---

Robert Moser

---

James Morel

---

Halil Berberoglu

**Error Analysis for Radiation Transport**

**by**

**John Thomas Tencer, B.S.M.E; M.S.E.**

**Dissertation**

Presented to the Faculty of the Graduate School of

The University of Texas at Austin

in Partial Fulfillment

of the Requirements

for the Degree of

**Doctor of Philosophy**

**The University of Texas at Austin**

**December 2013**

## **Dedication**

For my daughter, Nora.

## **Acknowledgements**

This material is based in part upon work supported by the Department of Energy [National Nuclear Security Administration] under Award Number [DE-FC52-08NA28615].

# Error Analysis for Radiation Transport

John Thomas Tencer, Ph.D.

The University of Texas at Austin, 2013

Supervisor: John R. Howell

All relevant sources of error in the numerical solution of the radiative transport equation are considered. Common spatial discretization methods are discussed for completeness. The application of these methods to the radiative transport equation is not substantially different than for any other partial differential equation. Several of the most prevalent angular approximations within the heat transfer community are implemented and compared. Three model problems are proposed. The relative accuracy of each of the angular approximations is assessed for a range of optical thickness and scattering albedo. The model problems represent a range of application spaces. The quantified comparison of these approximations on the basis of accuracy over such a wide parameter space is one of the contributions of this work.

The major original contribution of this work involves the treatment of errors associated with the energy-dependence of intensity. The full spectrum correlated-k distribution (FSK) method has received recent attention as being a good compromise between computational expense and accuracy. Two approaches are taken towards quantifying the error associated with the FSK method. The Multi-Source Full Spectrum k-Distribution (MSFSK) method makes use of the convenient property that the FSK method is exact for homogeneous media. It involves a line-by-line solution on a coarse grid and a number of k-distribution solutions on subdomains to effectively increase the

grid resolution. This yields highly accurate solutions on fine grids and a known rate of convergence as the number of subdomains increases.

The stochastic full spectrum k-distribution (SFSK) method is a more general approach to estimating the error in k-distribution solutions. The FSK method relies on a spectral reordering and scaling which greatly simplify the spectral dependence of the absorption coefficient. This reordering is not necessarily consistent across the entire domain which results in errors. The SFSK method involves treating the absorption line blackbody distribution function not as deterministic but rather as a stochastic process. The mean, covariance, and correlation structure are all fit empirically to data from a high resolution spectral database. The standard deviation of the heat flux prediction is found to be a good error estimator for the k-distribution method.

## Table of Contents

List of Figures .....	x
List of Illustrations .....	xv
Chapter 1: Introduction .....	1
Chapter 2: Spatial Discretization .....	4
Finite-Volume .....	5
Collocation .....	6
Galerkin Finite Element .....	7
Chapter 3: Angular Integration .....	8
Discrete Ordinates Method .....	8
Moment Methods .....	17
The Maximum Entropy Closure .....	18
Flux-limited Diffusion Equations .....	22
Spherical Harmonics .....	27
Simplified Spherical Harmonics .....	33
Comparison of Angular Approximations.....	37
Case 1 .....	39
Case 2 .....	46
Case 3 .....	55
Angular Approximation Conclusions .....	60
Chapter 4: Spectral Integration .....	62
Using HITRAN and HITEMP Spectral Databases .....	62
The Full Spectrum k-Distribution Method .....	66
The Multi-Source Full Spectrum k-Distribution Method .....	72
Computational Cost of the MSFSK Method.....	79
MSFSK Results and Discussion .....	80
The Stochastic Full Spectrum k-Distribution Method .....	91
Estimating Parameters for the SFSK Method.....	102

SFSK Results and Discussion .....	109
SFSK Conclusions .....	119
Spectral Integration Conclusions .....	120
Chapter 5: Summary and Conclusions.....	123
Appendix A .....	130
Appendix B .....	131
Appendix C .....	132
References .....	133

## List of Figures

Figure 3.1: Comparison of various quadrature rules for discrete ordinates approximation method .....	16
Figure 3.2: Comparison of several flux-limiters from the literature.....	26
Figure 3.3: Relative error in the $S_4$ prediction of Case 1 heat flux; Square enclosure with single hot wall and homogeneous participating medium. Error reported is the $L^2$ norm of the error in the heat flux prediction on the wall opposite the hot wall .....	41
Figure 3.4: Relative error in the $S_6$ prediction of Case 1 heat flux; Square enclosure with single hot wall and homogeneous participating medium. Error reported is the $L^2$ norm of the error in the heat flux prediction on the wall opposite the hot wall .....	42
Figure 3.5: Relative error in the M1 prediction of Case 1 heat flux; Square enclosure with single hot wall and homogeneous participating medium. Error reported is the $L^2$ norm of the error in the heat flux prediction on the wall opposite the hot wall .....	43
Figure 3.6: Relative error in the P1 prediction of Case 1 heat flux; Square enclosure with single hot wall and homogeneous participating medium. Error reported is the $L^2$ norm of the error in the heat flux prediction on the wall opposite the hot wall .....	44
Figure 3.7: Relative error in the SP3 prediction of Case 1 heat flux; Square enclosure with single hot wall and homogeneous participating medium. Error reported is the $L^2$ norm of the error in the heat flux prediction on the wall opposite the hot wall .....	45

Figure 3.8: Relative error in the  $S_6$  prediction of Case 2 heat flux; infinitely long hot cylinder surrounded by homogeneous moderator. Error reported is the  $L^2$  norm of the error in the heat flux prediction on a plane perpendicular to the axis of the cylinder ..... 48

Figure 3.9: Relative error in the  $S_8$  prediction of Case 2 heat flux; infinitely long hot cylinder surrounded by homogeneous moderator. Error reported is the  $L^2$  norm of the error in the heat flux prediction on a plane perpendicular to the axis of the cylinder ..... 49

Figure 3.10: Relative error in the M1 prediction of the Case 2 heat flux; infinitely long hot cylinder surrounded by homogeneous moderator. Error reported is the  $L^2$  norm of the error in the heat flux prediction on a plane perpendicular to the axis of the cylinder ..... 50

Figure 3.11: Relative error in the P1 prediction of the Case 2 heat flux; infinitely long hot cylinder surrounded by homogeneous moderator. Error reported is the  $L^2$  norm of the error in the heat flux prediction on a plane perpendicular to the axis of the cylinder ..... 51

Figure 3.12: Relative error in the P3 prediction of the Case 2 heat flux; infinitely long hot cylinder surrounded by homogeneous moderator. Error reported is the  $L^2$  norm of the error in the heat flux prediction on a plane perpendicular to the axis of the cylinder ..... 52

Figure 3.13: Relative error in the SP3 prediction of the Case 2 heat flux; infinitely long hot cylinder surrounded by homogeneous moderator. Error reported is the  $L^2$  norm of the error in the heat flux prediction on a plane perpendicular to the axis of the cylinder ..... 54

Figure 3.14: Relative error in the S <sub>4</sub> prediction of the Case 3 heat flux; square medium with a linearly varying temperature profile with temperature gradient parallel to two walls. Error reported is the L <sup>2</sup> norm of the error in the heat flux prediction on low temperature wall .....	55
Figure 3.15: Relative error in the S <sub>6</sub> prediction of the Case 3 heat flux; square medium with a linearly varying temperature profile with temperature gradient parallel to two walls. Error reported is the L <sup>2</sup> norm of the error in the heat flux prediction on low temperature wall .....	56
Figure 3.16: Relative error in the M1 prediction of the Case 3 heat flux; square medium with a linearly varying temperature profile with temperature gradient parallel to two walls. Error reported is the L <sup>2</sup> norm of the error in the heat flux prediction on low temperature wall .....	57
Figure 3.17: Relative error in the P1 prediction of the Case 3 heat flux; square medium with a linearly varying temperature profile with temperature gradient parallel to two walls. Error reported is the L <sup>2</sup> norm of the error in the heat flux prediction on low temperature wall .....	58
Figure 3.18: Relative error in the SP3 prediction of the Case 3 heat flux; square medium with a linearly varying temperature profile with temperature gradient parallel to two walls. Error reported is the L <sup>2</sup> norm of the error in the heat flux prediction on low temperature wall .....	59
Figure 4.1: Demonstration spectral integration domain for generating k-distributions [113] .....	67
Figure 4.2: Example k-distribution for CO <sub>2</sub> at 600K, 1 atm .....	69
Figure 4.3: Schematic illustration of multilayer system and geometric nomenclature [101] .....	74

Figure 4.4: Heat flux distribution in a non-isothermal medium bounded by cold black walls; Comparison of MSFSK results to line-by-line and k-distribution results .....	81
Figure 4.5: Heat flux distribution in a medium with linear temperature profile bounded by cold black walls; comparison of MSFSK and line-by-line results for CO <sub>2</sub> with a molar concentration of 10% .....	84
Figure 4.6: Heat flux distribution in a medium with quadratic temperature profile bounded by cold black walls; comparison of MSFSK and line-by-line results for CO <sub>2</sub> with a molar concentration of 10% .....	86
Figure 4.7: Convergence in relative error for the multilayer approximation for quadratic temperature profile example problem; L <sup>2</sup> error of MSFSK heat flux prediction relative to line-by-line prediction for CO <sub>2</sub> with a molar concentration of 10% .....	87
Figure 4.8: Steady-state temperature profiles for a slab with fixed temperature boundary conditions using line-by-line and MSFSK methods .....	89
Figure 4.9: Example of CO <sub>2</sub> spectrum in normal wavenumber space .....	94
Figure 4.10: CO <sub>2</sub> spectrum in reordered wavenumber space.....	95
Figure 4.11: Example k-distribution .....	96
Figure 4.12: Consistent spectral reordering .....	99
Figure 4.13: Error associated with inconsistent spectral reordering .....	101
Figure 4.14: Histogram of error due to spectral reordering .....	102
Figure 4.15: Scatter plot of log-error as a function of $g$ .....	106
Figure 4.16: Example correlation function .....	108
Figure 4.17: Heat flux distribution in slab with large temperature jump.....	110
Figure 4.18: Heat flux distribution in slab with linear temperature variation ....	113

Figure 4.19: Heat flux distribution in slab with quadratic temperature variation	114
Figure 4.20: Heat flux distribution in slab with cosine temperature variation ...	115
Figure 4.21: Actual vs. assumed spectral intensity at left wall in a slab with a cosine temperature variation; Intensity units are arbitrary .....	116
Figure 4.22: Heat flux distribution in slab with sine temperature variation .....	118
Figure 4.23: Heat flux distribution in slab with exponential temperature variation	119

## **List of Illustrations**

Illustration 3.1: Depiction of basal triangle [25].....	14
Illustration 3.2: Nomenclature for $P_3$ boundary conditions [42].....	31
Illustration 3.3: Depiction of ray-effects in low-order ( $N=6$ ) discrete ordinates solutions; contours of radiative energy density in medium from Case 1 with unity optical side-length and no scattering .....	40
Illustration 3.4: Case 2 geometry explanation; infinitely long hot cylinder surrounded by homogeneous moderator .....	47

## Chapter 1: Introduction

Radiation transport is an important phenomenon occurring in many physical systems. We will focus on radiation heat transfer through participating media. This involves the transport of photons through a translucent material. Photons may be emitted, absorbed, and scattered within the medium according to Equation (1.1).

$$\frac{1}{c} \frac{\partial I_\eta}{\partial t} + \vec{\Omega} \cdot \vec{\nabla} I_\eta(\vec{\Omega}) + \sigma_T I_\eta(\vec{\Omega}) = \kappa I_{b,\eta} + \frac{\sigma_s}{4\pi} \int I_\eta(\vec{\tilde{\Omega}}) d\tilde{\Omega} \quad (1.1)$$

The radiation transport equation (RTE) defines the intensity,  $I$  as a function of seven independent variables: three spatial coordinates, two angular coordinates, one spectral coordinate, and one temporal coordinate. For almost all heat transfer problems, the intensity field may be assumed to be steady-state. That is to say that the time scales involved in the RTE are significantly shorter than those associated with conduction or convection heat transfer. This is not to say that the heat transfer is steady-state nor that the intensity field is independent of time. The temporal derivative in Equation (1.1) is commonly neglected because of the speed of light in the denominator. The actual energy transfer in a combined-mode problem generally varies with time and is governed by Equation (1.2).

$$\rho c_p \frac{DT}{D\tau} = \beta T \frac{DP}{D\tau} + \nabla \cdot (k \nabla T - q_r) + q'' + \Phi_d \quad (1.2)$$

The intensity field enters through the divergence of the radiative flux vector. This quantity is expressed most conveniently through Equation (1.3). The radiative flux divergence is a function of only the 3 spatial coordinates and time. Note that although

the time-derivative term in Equation (1.1) may be neglected that the intensity field and consequently the flux divergence are generally time-dependent.

$$\nabla \cdot q_r = \int_{\eta=0}^{\infty} \left( 4\pi \kappa I_{b,\eta} - \int_{\Omega=0}^{4\pi} \kappa I_{\eta}(\Omega) d\Omega \right) d\eta \quad (1.3)$$

Equation (1.3) integrates out the dependence of the radiative flux divergence on direction and wavenumber. There are errors introduced when the RTE is spatially discretized and solved on a computer. This is true for numerical solutions to all partial differential equations. These errors are well-understood and may be driven arbitrarily small if provided sufficient computational resources. There are also errors introduced when evaluating the integrals in Equation (1.3) numerically. These errors are more difficult to eliminate. Straight-forward discretization of the spectral and angular domains in the same manner as the spatial domain is generally too computationally expensive for combined-mode problems. The exact angular distribution of the intensity is often unknown. In order to reduce the computational expense, low order approximations are commonly used to represent the angular dependence of the intensity. The spectral absorption coefficient,  $\kappa$  is a highly oscillatory function of the wavenumber. As a result, hundreds of thousands of quadrature points in the spectral coordinate must be taken to compute this integral directly. This is known as the line-by-line approach and is prohibitively expensive for most problems of interest.

One alternative to the line-by-line approach is the k-distribution method which will be discussed in detail in Chapter 4. The basic idea behind the k-distribution method is to take advantage of the fact that the absorption coefficient obtains the same value many times across the spectral domain. These disjoint spectral intervals result in

identical equations to be solved. In order to exploit this, the wavenumber space is reordered and scaled so that these spectral regions are no longer disjoint. There is a one-to-one correspondence between the original wavenumber space and this modified wavenumber space. The absorption coefficient is a smooth monotonically increasing function of this modified wavenumber. Integration over the modified wavenumber space is much less computationally expensive since the absorption coefficient and resulting intensity are smooth functions of the modified wavenumber.

## Chapter 2: Spatial Discretization

The most familiar source of error in the numerical solution to the RTE is spatial discretization. Numerical solution of any partial differential equation necessitates such a discretization. The most common methods for discretizing the spatial variables in the RTE are well known from other fields. They are collocation, finite-volume methods, and Galerkin finite element methods. Finite-volume and finite element methods are considerably more common. The spatial discretization scheme for the RTE is usually chosen to be compatible with the spatial discretization scheme for the energy equation. For pure radiation problems the choice is left up to the analyst. Familiarity and convenience are often deciding factors.

It has been shown [1] that convergence plateaus when the spatial grid is refined independently of the order of the angular approximation. Essentially, it is over-kill to solve approximate partial differential equations numerically to a very high precision. The errors introduced in the angular and spectral approximations tend to dwarf the spatial discretization error for combined mode problems. A fine spatial discretization is commonly required to resolve convection phenomena. As a result, radiation transport is resolved on a much finer grid than may otherwise be necessary. This leaves very little computational power left over for pursuing higher order angular or spectral discretization schemes for the radiative transport equation.

The angular and spectral approximation methods will be described in Chapter 3 and Chapter 4 respectively. Regardless of the method, the result is the transformation of the 6-dimensional transport equation (neglecting the temporal derivative) into a finite set of coupled partial differential equations in the 3 spatial variables. This set may include only a single partial differential equation as is the case with a gray P1 approximation or

an arbitrarily large number of equations. The number of dependent parameters to be solved for as well as the degree of coupling depends upon which approximation method is used. This set of partial differential equations is then solved numerically by conventional means. Most often, this involves collocation, finite element, or finite volume methods. These three techniques will now be briefly described. Detailed derivations of each of these methods should be available in any fundamental textbook on numerical analysis [2, 3, 4].

## **FINITE-VOLUME**

One of the most common methods for spatially discretizing the RTE is the finite-volume method [5, 6]. This is the same finite-volume method that is used in many commercial PDE-solver applications. In the finite-volume method, the domain is divided into a set of small volume elements. This mesh may be either structured or unstructured. The governing partial differential equation is then integrated over each volume element. The divergence theorem, Equation (2.1) is then used to convert integrals over the volume into integrals over the bounding surfaces.

$$\iiint_V (\vec{\nabla} \cdot \vec{F}) dV = \oint_{\partial V} (\vec{F} \cdot \vec{n}) dS \quad (2.1)$$

There are many natural advantages to the finite-volume method. The method is inherently conservative. The flux leaving one volume is always equal to the flux entering an adjacent volume. The common application of finite volume methods for solving conduction and convection problems makes it a natural choice for combined mode problems involving radiative transport. Additionally, the finite volume method is very

commonly combined with the discrete ordinates approximation for radiation transport problems.

The finite-volume discretization approach may also be applied to the angular discretization. This method is similar to the discrete ordinates method both in concept and in accuracy. It will not be discussed in Chapter 3.

## COLLOCATION

In the collocation method [7, 8] a set of basis functions is defined. The solution to the given partial differential is approximated as a linear combination of these basis functions. The combination of basis functions is chosen such that the partial differential equation is satisfied at a specified set of discrete points (called collocation points). After choosing a set of collocation points and a family of basis functions a set of algebraic equations is found by analytically differentiating the basis functions and substituting into the original PDE.

It should be noted that satisfying the differential equation at the collocation points is not equivalent to having 0 error between the approximate and exact solutions at the collocation points. As a result, the approximate solution is not exact at the collocation points. Instead, the residual is zero. However, the approximate solution is expected to converge to the exact solution as the number of collocation points and basis functions increases.

The family of basis functions chosen has a great effect on the flexibility of the method and the conditioning of the resulting algebraic system of equations. Families of basis functions with global support result in so-called spectral methods. Basis functions with finite support are used in finite element methods. Spectral methods are considerably less common today than finite element methods.

## GALERKIN FINITE ELEMENT

The requirement that the residual be identically zero at the collocation points may be seen as too restrictive. As an alternative, rather than setting the residual to zero at a set of predetermined points, the residual is minimized in a more global sense. The residual is required to be orthogonal to the finite set of basis functions used to represent the function. This is known as a Galerkin projection. This is a special case of the method of weighted residuals.

The Galerkin finite element method [9, 10, 11] was first widely adopted for the solution of solid mechanics problems. It has since been successfully applied to heat transfer and fluid flow problems including solution to the RTE.

The Galerkin finite-element method is one of the most popular solution techniques for sets of partial differential equations. It is easily applied on unstructured meshes. Greater accuracy may be achieved either by refining the spatial grid or increasing the order of the basis functions.

## Chapter 3: Angular Integration

The intensity field specified by the RTE is a function of direction. In two- or three-dimensional problems, two angular variables are required to fix this direction: a circumferential angle and an azimuthal angle. In a one-dimensional slab geometry, only one angular variable is needed. In this case, symmetry dictates that the intensity does not vary with the circumferential angle.

The quantity of interest, the radiative flux divergence is not a function of direction. The dependence upon the circumferential and azimuthal angles has been integrated out. There have been many techniques developed for representing the directional dependence of the intensity [12]. A few of the most common are discussed in detail in this chapter. The accuracy of each method is evaluated as a function of opacity and scattering albedo. In order to limit the scope of the work, all scattering is treated as isotropic.

### DISCRETE ORDINATES METHOD

One of the most commonly used radiative transport solution techniques is the method of discrete ordinates [13, 14, 15]. It is so widely used largely because of the intuitive derivation of the equations and boundary conditions and the theoretical guarantee that it will converge to the correct solution as the number of ordinate directions goes to infinity. Unfortunately, this convergence is slow and the method may produce unrealistically oscillatory solutions known as ‘ray effects’ when discontinuous boundary conditions are present.

The discrete ordinates method is a general term for a class of solution methods to the radiative transport equation that rely upon some manner of discretization of the angular variables. The transport equation is satisfied exactly along a set of discrete

directions and a quadrature rule is used to approximate any integrals over the angular space such as those in the in-scattering term or in the definitions of the radiative flux and flux divergence. The choice of quadrature rule is left up to the user and may have a significant impact upon the quality of results obtained. There has been substantial research effort applied to the development and analysis of quadrature rules for integration over the unit sphere [16, 17, 18]. The solution of the radiative transport equation using the discrete ordinates method may be found by stepping through the domain [19, 20, 21, 22]. This is easily accomplished in structured meshes. However, in unstructured meshes, this solution technique may involve significant additional overhead and may not be ideal. The discrete ordinates method has also been applied to unstructured meshes using stepping schemes and other more general solution techniques [23, 24, 25].

For a given angular quadrature, the integral in the in-scattering term may be approximated as a summation as shown in Equation (3.1).

$$\frac{\sigma_s}{4\pi} \int I(\vec{\Omega}) d\vec{\Omega} \approx \frac{\sigma_s}{4\pi} \sum_i w_i I(\vec{\Omega}_i) \quad (3.1)$$

The weights and nodes of the quadrature scheme are  $w_i$  and  $\vec{\Omega}_i$  respectively. The weights are normalized such that they sum to  $4\pi$ .

In this way, it is trivial to see that the transport equation may be written as a system of linear first order equations in the ordinate directions.

$$\vec{\Omega}_i \cdot \vec{\nabla} I_i + \sigma_T I_i = \kappa I_b + \frac{\sigma_s}{4\pi} \sum_j w_j I_j \quad (3.2)$$

With diffuse walls, this equation is subject to the boundary condition

$$I_i = \varepsilon I_{bw} + \frac{1-\varepsilon}{\pi} \sum_{\vec{n} \cdot \vec{\Omega}_j < 0} w_j I_j |\vec{n} \cdot \vec{\Omega}_j| \quad (3.3)$$

Since the equation is first order, a boundary condition is only required on half the boundary for each directional intensity. The boundary condition above only applies if  $\vec{n} \cdot \vec{\Omega}_j > 0$ . That is, we only apply a condition on the intensity leaving an opaque surface.

The first-order discrete ordinates equation has stability problems when using the Galerkin finite element method. Equation (3.2) is a set of coupled convection-diffusion-reaction equations with zero diffusion coefficient. The Galerkin finite element method is known to be unstable if the element Péclet number (Pe) and Damköhler number (Da) product is larger than one. If this product is less than or equal to unity, the method may or may not be stable. This instability condition is trivially satisfied when diffusion is absent from the equation to be solved implying that the Galerkin finite element solution to the first-order discrete ordinates equation is inherently unstable.

$$2DaPe = \frac{|\sigma_T| h^2}{c} > 1 \quad (3.4)$$

Here,  $c$  is the diffusion coefficient and  $h$  is the mesh element size. Unfortunately, the absence of a diffusion term means that there is not necessarily a mesh resolution fine enough to make the discretization stable. This implies that further mesh refinement will not remove the spurious oscillations in every case. For this reason, a stabilization method is required.

In the Streamline Upwind Petrov-Galerkin (SUPG) stabilization method, the test function  $\tilde{I}_l$  is replaced with  $\tilde{I}_l + \tau \vec{\Omega}_l \cdot \vec{\nabla} \tilde{I}_l$  where  $\tau$  is a stabilization parameter. For our

case (no diffusion) the stabilization parameter is determined to be approximately  $h/2$ . A commonly used “optimal” value of  $\tau$  is found to be

$$\tau = \frac{h}{2\|\vec{\Omega}\|} \left( \coth Pe - \frac{1}{Pe} \right) \quad (3.5)$$

which reduces to  $h/2$  since  $\vec{\Omega}$  is a unit vector and  $Pe \rightarrow \infty$ .

Alternatively, the second-order discrete ordinates equations may be used. A standard property of all commonly used discrete ordinates quadrature rules is invariance under rotations of  $90^\circ$ . Of course, this immediately implies invariance under rotations of  $180^\circ$  as well which implies that if a direction  $\vec{\Omega}$  is part of a quadrature set that  $-\vec{\Omega}$  is as well and that both directions have equal weight. Following the development of Lewis and Miller [19], we define the even and odd parity intensities as

$$\begin{aligned} I^+(\vec{\Omega}) &= \frac{1}{2}(I(\vec{\Omega}) + I(-\vec{\Omega})) \\ I^-(\vec{\Omega}) &= \frac{1}{2}(I(\vec{\Omega}) - I(-\vec{\Omega})) \end{aligned} \quad (3.6)$$

We then obtain a second-order partial differential equation for the even parity intensity.

$$-\vec{\Omega} \cdot \vec{\nabla} \left( \frac{1}{\sigma_T} \vec{\Omega} \cdot \vec{\nabla} I^+ \right) + \sigma_T I^+ = \kappa I_b + \frac{\sigma_s}{2\pi} \int I^+(\vec{\Omega}) d\vec{\Omega} \quad (3.7)$$

The odd parity intensity is related to the even parity intensity by

$$\vec{\Omega} \cdot \vec{\nabla} I^+ = -\sigma_T I^- \quad (3.8)$$

The same discretization procedure is applied as with the first-order equation.

$$-\vec{\Omega}_i \cdot \vec{\nabla} \left( \frac{1}{\sigma_T} \vec{\Omega}_i \cdot \vec{\nabla} I_i^+ \right) + \sigma_T I_i^+ = \kappa I_b + \frac{\sigma_s}{2\pi} \sum_j w_j I_j^+ \quad (3.9)$$

The corresponding boundary condition for a diffusely emitting and reflecting opaque boundary is given by

$$I_i^+ - \text{sign}(\vec{n} \cdot \vec{\Omega}) \frac{1}{\sigma_T} \vec{\Omega} \cdot \vec{\nabla} I_i^+ = \epsilon I_{bw} + \frac{1-\epsilon}{\pi} \sum_j w_j |\vec{n} \cdot \vec{\Omega}_j| (2I_j^+ - I_{bw}) \quad (3.10)$$

The second-order formulation has the advantage of being naturally diffusive and does not require additional stabilization. It also involves half as many unknowns as the first-order formulation. It has the comparative disadvantage of generating a less sparse matrix. While the first-order formulation allows for rapid solution by use of a stepping scheme for structured meshes, the second-order formulation is not well-suited for such acceleration techniques.

There has been substantial research applied to the development and analysis of quadrature rules for integration over the unit sphere [16, 17, 18]. The most intuitive quadrature rule is the level symmetric scheme tabulated in Appendix A. The level symmetric scheme is invariant to rotations of multiples of 90°. Level symmetric quadrature rules are popular for general applications because of their rotational symmetry [19, 26, 27, 28, 29, 30, 31]. There is, however a limit to the degree of accuracy that may be obtained using level symmetric quadrature rules. Negative weights are present in the S<sub>22</sub> quadrature set. As a result, level symmetric schemes may not be capable of reproducing strongly anisotropic intensity fields. The S<sub>22</sub> quadrature scheme uses 66

ordinates per octant. This results in 264 independent variables for a 2D problem and 528 for a 3D problem. This large a number of ordinates is neither necessary nor feasible for most applications, so level symmetric quadrature rules are deemed to be a good choice for general problems.

There have been some improvements to the level symmetric schemes. Koch et al proposed the DCT quadrature schemes and showed that the DCT-020-1246 and DCT-111-1246810 provide more accurate results than the  $S_6$  and  $S_8$  schemes respectively while using the same number of ordinate directions [17]. The DCT schemes maintain the same rotational invariances that make the level symmetric scheme attractive for general problems.

The  $T_N$  quadrature sets developed by Thurgood [32] are the two-dimensional extension of the rectangle rule. An equilateral triangle (basal triangle) is defined within the first octant by the points  $(1,0,0)$ ,  $(0,1,0)$ , and  $(0,0,1)$  as shown in Illustration 3.1.

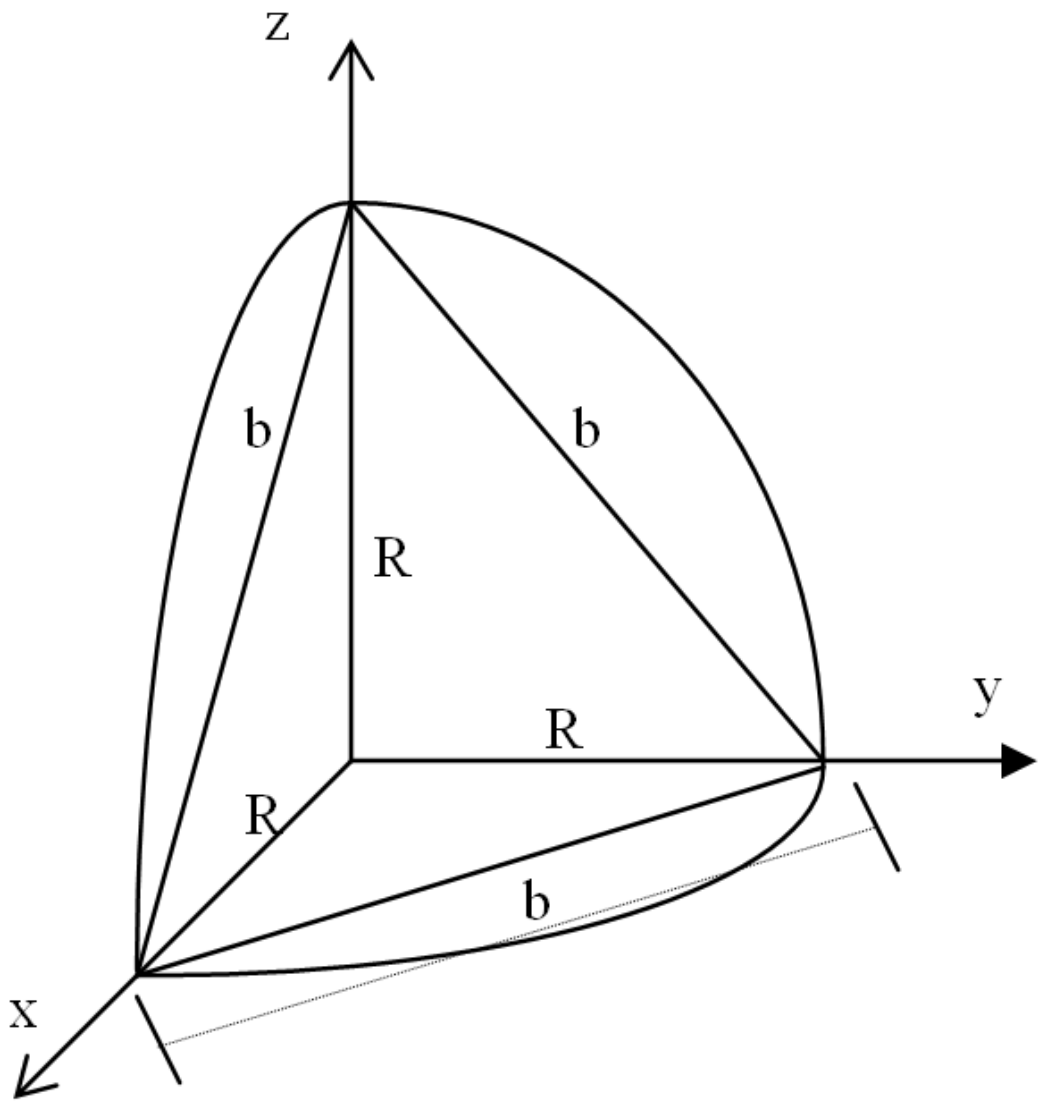


Illustration 3.1: Depiction of basal triangle [33]

The basal triangle is then tessellated with smaller similar triangles with side length  $\sqrt{2}/N$  resulting in  $N^2$  smaller triangles. The ordinate set is defined as the set of angles passing through the centroids of these small triangles with weights equal to the solid angle subtended by each triangle.

The solid angle subtended by a given triangle may be found by utilizing L'Huilier's Theorem. This is also known as the spherical excess,  $E$ . A spherical triangle with semiperimeter  $s$  and sides of lengths  $a, b$ , and  $c$  has a spherical excess given by Equation (3.11).

$$\tan\left(\frac{1}{4}E\right) = \sqrt{\tan\left(\frac{s}{2}\right)\tan\left(\frac{s-a}{2}\right)\tan\left(\frac{s-b}{2}\right)\tan\left(\frac{s-c}{2}\right)} \quad (3.11)$$

The  $P_N$ -EW <sub>$N$</sub> , and  $P_N$ -T <sub>$N$</sub>  quadrature sets [34] both use the roots of the  $N^{\text{th}}$  order Legendre polynomial to define levels along the z-axis. Each level has a total weight given by the corresponding Gauss-Legendre quadrature set. In the  $P_N$ -EW <sub>$N$</sub>  quadrature each level is then divided equally again following the level symmetric approach. In the  $P_N$ -T <sub>$N$</sub>  quadrature the azimuthal angles for each level are set equal to the roots of the Chebyshev polynomials. This list of quadrature rules is by no means exhaustive. There are additional sets [35, 18, 36] not considered here which have been omitted in the interest of brevity.

Although there have been many studies comparing the relative accuracies of the different quadrature rules, an additional comparison is provided here. A test problem of a square duct with a single hot wall is selected as a basis for comparison. The medium is purely absorbing. It neither scatters nor emits radiation. All four walls are black. An analytical series solution to this problem has been developed by Crosbie and Schrenker [37]. This technique was later expanded to inhomogeneous media with isotropic scattering [38] although those cases will not be considered here.

The purely absorbing case with black walls was chosen to accentuate the ‘ray-effects’ which appear as a result of the angular discretization. The quantity of interest is

the spatially resolved heat flux on the wall opposite the heated surface. Again, this was chosen to accentuate the error due to ‘ray-effects.’

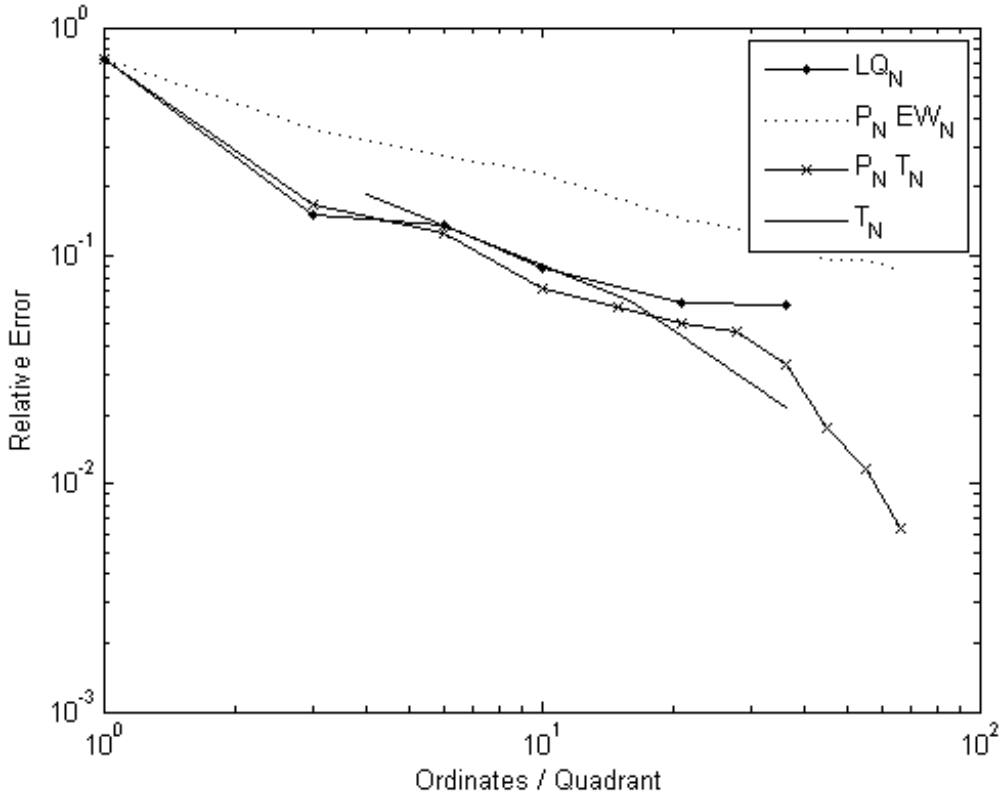


Figure 3.1: Comparison of various quadrature rules for discrete ordinates approximation method

The  $P_N EW_N$  quadrature rule is seen to be generally less accurate and to converge more slowly than the other quadrature rules. This finding is consistent with the literature [34]. The other quadrature rules perform similarly which is also consistent with the literature. The  $P_N T_N$  quadrature rule is selected for comparisons to the other angular approximation techniques. This is because it does not possess the disadvantages of the  $LQ_N$  and  $T_N$  quadrature rules. Namely, it is not limited with respect to the maximum achievable order and the number of ordinates per octant is less sensitive to changes in  $N$ .

The number of ordinate directions required in the  $T_N$  rule is  $N^2$  while the other, level-symmetric rules require only  $\frac{1}{4}N\left(\frac{N}{2}+1\right)$  ordinates. This difference in the definition of the subscript,  $N$  is important to note when comparing various quadrature rules. The rapid growth in ordinate directions with  $N$  for the Thurgood quadrature set allows for less control of the accuracy of the solution by varying  $N$ .

## MOMENT METHODS

Moment methods originally developed for nuclear engineering applications are becoming more popular for solving heat transfer problems. They are an inexpensive alternative to discrete ordinates expansions. At their core, moment methods involve taking angular moments of the RTE and recasting them as a series of partial differential equations in terms of the moments of intensity. This is attractive since only the 0<sup>th</sup> and 1<sup>st</sup> moments of intensity enter the general energy equation.

A problem arises as the  $n^{\text{th}}$  moment of the RTE always involves the  $(n+1)^{\text{th}}$  moment of the intensity. The series of equations is not closed. To close the set of equations, a relation between the  $(n+1)^{\text{th}}$  moment of intensity and the lower order moments of intensity is required. One such closure condition is the maximum entropy closure. This choice gives rise to the so-called M1 method.

The M1 method based on the maximum entropy closure developed by Minerbo [39] is derived and examined. Issues with the stability of this method are addressed by recasting the telegrapher's equation as a flux-limited diffusion equation. This transformation prevents the formation of unphysical shocks in the energy density solution when the assumption of an axially symmetric intensity is poor. In an optically thin problem with multiple heat sources and partially reflecting boundaries this assumption is

almost never justified. Therefore, the more robust flux-limited diffusion description is used.

### The Maximum Entropy Closure

The steady-state radiative transport equation with isotropic scattering is repeated for convenience. The subscripts denoting the spectral dependence of the intensity have been suppressed.

$$\vec{\Omega} \cdot \vec{\nabla} I(\vec{\Omega}) + \sigma_T I(\vec{\Omega}) = \kappa I_b + \frac{\sigma_s}{4\pi} \int I(\vec{\Omega}') d\vec{\Omega}' \quad (3.12)$$

Taking the 0<sup>th</sup> and 1<sup>st</sup> moments of this equation yields

$$\vec{\nabla} \cdot \vec{F} = 4\pi\kappa I_b - \kappa c E \quad (3.13)$$

$$c\vec{\nabla} \cdot \vec{P} = -\kappa \vec{F} \quad (3.14)$$

where  $E$ ,  $F$ , and  $P$  are the radiative energy density, flux, and pressure respectively. They are defined by

$$E = \frac{1}{c} \int I(\vec{\Omega}) d\Omega \quad (3.15)$$

$$\vec{F} = \int \vec{\Omega} I(\vec{\Omega}) d\Omega \quad (3.16)$$

$$\vec{P} = \frac{1}{c} \int \vec{\Omega} \otimes \vec{\Omega} I(\vec{\Omega}) d\Omega \quad (3.17)$$

As a matter of personal preference, we shall work with the dimensionless quantities:

$$\Phi = \frac{I}{cE} \quad (3.18)$$

$$\vec{f} = \frac{\vec{F}}{cE} \quad (3.19)$$

$$\vec{T} = \frac{1}{E} \vec{P} \quad (3.20)$$

$\vec{T}$  is classically referred to as the Eddington tensor. Because it is defined as the second moment of the nonnegative energy density,  $\Phi$  on the unit sphere we have the following constraints [40, 41]:

$$tr(\vec{T}) = 1 \quad (3.21)$$

$$\vec{T} - \vec{f} \otimes \vec{f} \geq 0 \quad (3.22)$$

Taken together, these conditions imply that  $\|\vec{f}\| \leq 1$  or in other words that the solution is flux-limited.

In order to close the above equations, a relationship must be found between the Eddington tensor and the energy density and flux. If we assume that the intensity is symmetric about the direction of the flux the form of  $\vec{T}$  may be reduced to:

$$\vec{T} = \vec{I} \left( \frac{1-\chi}{2} \right) + \vec{n} \otimes \vec{n} \left( \frac{3\chi-1}{2} \right) \quad (3.23)$$

where  $\vec{I}$  is the identity matrix,  $\vec{n} = \vec{f} / \|\vec{f}\|$ , and  $\chi$  is the Eddington factor which may be written explicitly as:

$$\chi = \int (\vec{\Omega} \cdot \vec{n})^2 \Phi d\Omega = 2\pi \int_{-1}^1 \mu^2 \Phi(\mu) d\mu \quad (3.24)$$

The goal is to define the Eddington factor as a function of the magnitude of the dimensionless flux. This has been accomplished in a variety of ways. Kershaw [41] suggested the simple relationship

$$\chi(f) = \frac{(1+2f^2)}{3} \quad (3.25)$$

This relationship is simple but is also not derived from any physical intuition. It is expected that other Eddington factors which are motivated by physical arguments will provide more accurate results. By maximizing the entropy relationship derived by assuming Maxwell-Boltzmann statistics, Minerbo [39] derived the following transcendental relationship for  $\chi$ .

$$\begin{aligned} \chi &= 1 - \frac{2}{Z} f \\ f &= \coth(Z) - \frac{1}{Z} \end{aligned} \quad (3.26)$$

This is the basis for the M1 model which has recently been gaining popularity as advancements in numerical techniques and increased computing resources have made treating the resulting ill-conditioned nonlinear system tractable for interesting problems [42, 43, 44, 45, 46, 47]. Because the transcendental relationship is difficult to solve and is divergent from theoretical values at the endpoints  $f = \{0,1\}$  it is common practice to use various approximations. Minerbo [39] originally suggested

$$\chi = \frac{1}{3} + \frac{0.01932f + 0.2694f^2}{1 - 0.5953f + 0.02625f^2} \quad (3.27)$$

This relationship does not exhibit the correct behavior as  $f \rightarrow 1$  and so Ripoll [45] developed an alternative

$$\chi = \frac{3+4f^2}{5+2\sqrt{4-3f^2}} \quad (3.28)$$

More recently, Brown and Pierce [47] proposed a curve fit of the form

$$\chi = \frac{1}{3}Cf^2 + \left( \frac{2}{3} - C \right)f^4 \quad (3.29)$$

where  $C$  is a constant which was found to be equal to 0.335696. A fit of this form was motivated by the desire to have an expression for  $\chi$  that was accurate, well behaved, and able to be evaluated very quickly for use in a fast running code.

It has been observed [42, 47, 48] that solutions derived using the maximum entropy closure may exhibit non-physical discontinuities. Brunner [48] demonstrated that the equations only require that the product of the Eddington factor and the energy density,  $\chi E$  be continuous (as well as the flux,  $F$ ). This allows both  $\chi$  and  $E$  to be independently discontinuous. These discontinuities represent a significant difficulty when coupling with other heat transfer modes in a general problem. The energy density is directly related to the flux divergence which enters the general energy equation. Additionally, specialized numerical methods are required in order to attain converged solutions in general cases. These numerical shocks arise in regions for which more than one direction is significant and the assumption that the intensity is axially symmetric about the direction of the flux is a poor one.

## Flux-limited Diffusion Equations

The Eddington tensor closures are related to flux-limited diffusion theory. Every Eddington factor relationship has a corresponding flux limiter. Unlike when using a telegrapher's equation description of radiative transfer, when formulated as a flux-limited diffusion equation, the 0<sup>th</sup> and 1<sup>st</sup> moment equation are comparatively well behaved and do not generate shocks [40]. It is therefore preferable to express the 2<sup>nd</sup> moment closure as a nonlinear form of Fick's law when generating solutions. Valuable physical insight may be gained by expressing a given closure in the more physically meaningful telegrapher's form but this form is less robust numerically.

The flux-limited diffusion method includes the same 0<sup>th</sup> and 1<sup>st</sup> moment equations as above. The difference is that rather than expressing the 2<sup>nd</sup> order Eddington tensor explicitly, the divergence of the radiative pressure is modeled as a nonlinear function of the dimensionless energy density gradient. As a result, the 1<sup>st</sup> moment equation may be expressed (neglecting the temporal derivative) in the form of Fick's first law with a nonlinear diffusion coefficient.

$$\vec{F} = \frac{-c}{\omega \sigma_T} \lambda(R) \vec{\nabla} E \quad (3.30)$$

where  $\vec{R} = -(1/\omega \sigma_T)(\nabla E/E)$  is the dimensionless gradient and the effective albedo is given by  $\omega = (\sigma_S E + \kappa B)/(\sigma_T E)$  and  $B$  is the black body energy density defined analogously to the radiative energy density,  $E$ . Pomraning [49] proposed a more generalized form of this equation.

$$\vec{F} = \frac{-c}{\omega \sigma_T \gamma(R)} \lambda(R) \vec{\nabla} (\gamma(R) E) \quad (3.31)$$

Here,  $\gamma(R)$  is an arbitrary function that is slowly varying in space. Pomraning made use of the added flexibility in order to develop interface conditions. He proposed using Equation (3.32) in order to generate correct results for a model problem. The model problem chosen was the generalized Milne problem which involves the interface of two half-spaces.

$$\gamma(R) = \frac{1 + 0.5959R}{2.1313 + 0.5959R} \quad (3.32)$$

Pomraning [49] also proposed a slightly different definition of the parameter  $R$  for problems in general geometries.

$$R = \frac{-\vec{\nabla} \cdot \vec{F}}{\sigma_T \omega c E} = \frac{1 - \omega}{\omega} \quad (3.33)$$

Once again,  $\omega$  in Equations (3.30), (3.31), and (3.33) is the effective albedo which includes in its definition one of the solution variables,  $E$ . This author has found that the definition of  $R$  in Equation (3.33) provides a more stable system of equations when using the finite element method in higher dimensional geometries than the dimensionless gradient. In particular, this choice of  $R$  results in increased stability in the limits of pure scattering and small internal sources.

There is a notable complication with this definition. It allows for  $R$  to become negative in strongly emitting regions. This is not a problem for the maximum entropy flux limiter or any of the other limiters derived from Eddington factors. However, it does present a problem for some of the ad hoc limiters used in the literature as well as some of the curve fits proposed since these expressions are generally fit using only positive data and are usually only plotted for positive  $R$ . The solution is to note that all of the flux-

limiters derived from Eddington factors are even functions so that the curve fits will perform reasonably well if  $|R|$  is used instead of  $R$ .

The diffusion formulation of the maximum entropy closure possesses another advantage as well. The boundary conditions when using this formulation are the same as those used by the well-documented P1 approximation with the above alternative definition of the flux used. These conditions are expressed easily and their implementation is trivially checked against generic diffusion solutions. The Marshak boundary condition is

$$2\vec{F} \cdot \vec{n} = \frac{\epsilon}{2-\epsilon} (4E_{bw} - E) \quad (3.34)$$

The nonlinear parameter  $\lambda$  in Equation (3.31) is called the flux limiter. It is related to the Eddington factor derived before by

$$\lambda(R) = \chi(f) - f^2 \quad (3.35)$$

While any arbitrary function may be introduced to define a flux limiter, those derived from Eddington factors tend to be more physically significant. The equivalent flux limiter to the Kershaw Eddington factor is

$$\lambda(R) = \sqrt[3]{(3 + \sqrt{9 + 4R^2})} \quad (3.36)$$

The maximum entropy flux limiter is once again defined by a transcendental equation.

$$\lambda = \frac{1}{Z^2} - \operatorname{csch}^2(Z)$$

$$R = \frac{\coth(Z) - 1/Z}{\lambda} \quad (3.37)$$

To the author's knowledge, no alternative fit analogous to the ones used for the maximum entropy Eddington factor has been proposed for the maximum entropy flux limiter. A fit of the form

$$\lambda(R) \equiv \frac{2}{3\pi} \cot^{-1}(\alpha R) \quad (3.38)$$

is proposed. An optimal value for  $\alpha$  was found to be 0.2673. Visually, this fit matches the solution to the transcendental equation. Pomraning [49] proposed a rational fit to a flux limiter derived from previous work by Levermore and Pomraning [50].

$$\lambda(R) \equiv \frac{1 + 0.1440R}{3 + 1.0320R + 0.1440R^2} \quad (3.39)$$

Although their physical basis is very dissimilar, Eddington factors derived by Minerbo [39] and Levermore and Pomraning [50] provide very similar quantitative results [51]. Not surprisingly, the rational fit proposed by Pomraning is very similar to the single parameter fit proposed above.

However, both of these fits are less than ideal. Values for the flux-limiter may include large ( $\sim 20\%$ ) relative errors as  $R \rightarrow \infty$  as well as significant absolute errors in the neighborhood of  $R=3$ . They are also not well behaved in the diffusion limit since they decrease too rapidly away from  $1/3$  as  $R$  increases from 0. With these limitations understood, the above equation is attractive for its analytical simplicity and its relatively

small errors for intermediate values of  $R$ . It is also noted that solutions of the RTE are relatively insensitive to accurate evaluation of the flux-limiter. This is one of the reasons that so many different flux-limiters have been proposed and used over the years.

The results are very similar and a priori it is impossible to know which will perform best for a particular application. The Pomraning fit will probably be preferable in most applications despite not being derived from the maximum entropy Eddington factor since it is both simple to implement and fast to evaluate. A variety of flux-limiters is plotted below. An index of flux-limiters from the literature is included in Appendix B.

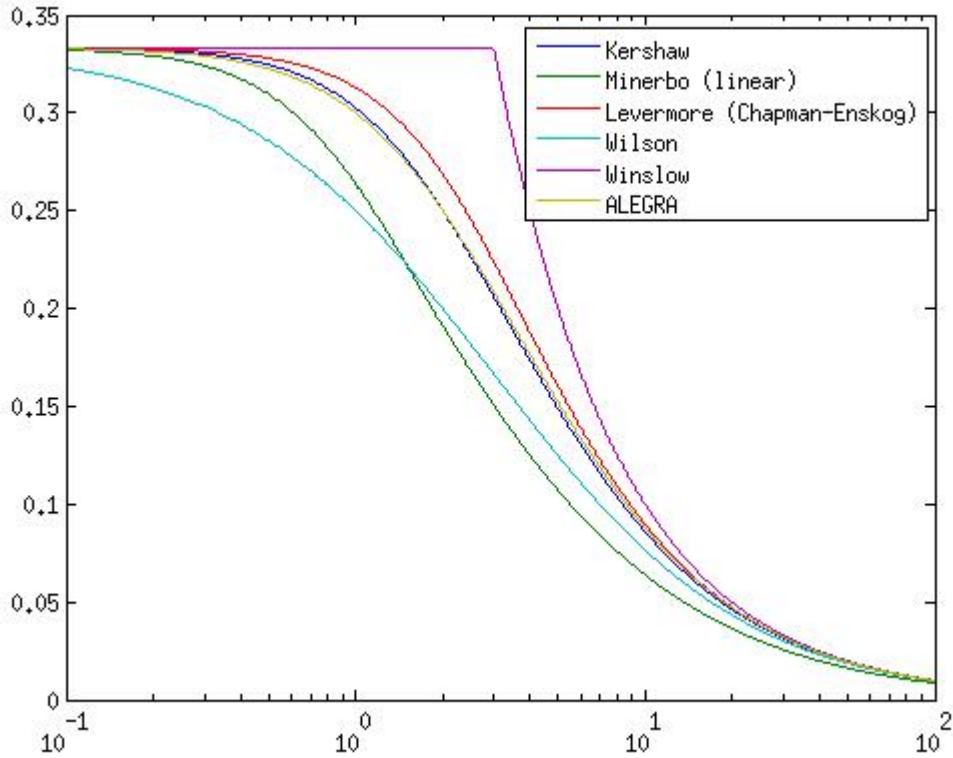


Figure 3.2: Comparison of several flux-limiters from the literature

The Arbitrary-Lagrangian-Eulerian General Research Applications (ALEGRA) code is a shock physics code from Sandia National Labs. Its radiation package includes a unique flux-limiter. A list of the functional forms of a large number of flux-limiters, including the ALEGRA flux-limiter, is included in Appendix B.

The M1 method is very fast and is significantly less memory-intensive than the discrete ordinates method. When cast as a flux-limited diffusion equation, the solutions are smooth and stable. It does not suffer from the ‘ray effect’ problem common to all discrete ordinate methods. However, the M1 method does result in a nonlinear partial differential equation which does require iteration to solve. This makes it more computationally expensive than some of the linear methods to follow such as the P1 and SP3 approximations.

## **Spherical Harmonics**

In the spherical harmonics method [52, 53, 54, 55], the directional intensity is expanded in a series of spherical harmonics. The coefficients in the series become the unknown quantities. Unlike the discrete ordinates method, the spherical harmonics method provides a continuous rather than a discrete representation of the angular intensity. As a result, solutions to the resulting equations do not suffer from the ‘ray effects’ which have proven to be so troubling for the discrete ordinates method.

The moment methods are limited in their level of accuracy by the impracticality of providing higher order closure conditions. The method of spherical harmonics does not have this problem, at least not directly. High order spherical harmonics expansions have been developed and used in a wide variety of applications [52, 19]. However, the number of unknowns increases rapidly with the order of the approximation and the

derivations become quite long. As a result, higher order expansions are rarely used for heat transfer applications [56].

Following the work of Modest and Yang [52] the RTE is recast as  $N(N+1)/2$  coupled second-order elliptic partial differential equations. As presented by Davison [57], the angular intensity at a given point is represented as an infinite series.

$$I(\Omega) = \frac{1}{4\pi} \sum_n (2n+1) J_n(\Omega) \quad (3.40)$$

where

$$J_n = \frac{1}{2n+1} \sum_{m=-n}^n I_n^m Y_n^m(\Omega) \quad (3.41)$$

The dual-indexed coefficients in the expansion,  $I_n^m$  may vary with position and wavenumber. The spherical harmonics functions are defined in terms of the circumferential ( $\theta$ ) and azimuthal ( $\phi$ ) angles [58].

$$Y_n^m(\theta, \phi) = \begin{cases} \cos(m\phi) P_n^m(\cos\theta) & m \geq 0 \\ \sin(m\phi) P_n^m(\cos\theta) & m < 0 \end{cases} \quad (3.42)$$

The associated Legendre polynomials are

$$P_n^m(x) = (-1)^m \frac{(1-x^2)^{|m|/2}}{2^n n!} \frac{d^{n+|m|}}{dx^{n+|m|}} (x^2 + 1)^n \quad (3.43)$$

Substituting Equation (3.40) into the RTE

$$\sum_n^N (2n+1) \vec{\Omega} \cdot \vec{\nabla} J_n = - \left[ \sum_n^N (2n+1) J_n \right] + 4\pi\kappa I_b + \frac{\sigma_s}{4\pi} \int \sum_n^N (2n+1) J_n (\vec{\tilde{\Omega}}) d\tilde{\Omega} \quad (3.44)$$

The in-scattering term may be simplified using the orthogonality of the spherical harmonics functions over the unit sphere.

$$\frac{\sigma_s}{4\pi} \int \sum_n^N (2n+1) J_n (\vec{\tilde{\Omega}}) d\tilde{\Omega} = \sigma_s J_0 (\vec{\Omega}) = \sigma_s I_0^0 \quad (3.45)$$

The streaming term may be rewritten as well.

$$[\vec{\Omega} \cdot \vec{\nabla} J_n]_{R=1} = \left[ \vec{\Omega} \cdot \vec{\nabla} J_n - \frac{R^2}{2n+1} \vec{\nabla}_s \cdot \vec{\nabla} J_n \right]_{R=1} + \left[ \frac{1}{2n+1} \vec{\nabla}_s \cdot \vec{\nabla} J_n \right]_{R=1} \quad (3.46)$$

The first term on the right is the spherical harmonic of order  $n+1$  while the second term is the spherical harmonic of order  $n-1$ . Equations (3.45) and (3.46) may be substituted into Equation (3.44).

$$\vec{\nabla}_s \cdot \vec{\nabla} J_{n+1} + (2n+1) J_n + (2n-1) \vec{\Omega} \cdot \vec{\nabla} J_{n-1} - R^2 \vec{\nabla}_s \cdot \vec{\nabla} J_{n-1} = 4\pi\kappa I_b \delta_{n,0} + \sigma_s A_n J_n \quad (3.47)$$

For a two-dimensional geometry, the resulting 6 equations are reduced to 4 equations for the harmonics  $I_0, I_2^{-2}, I_2^0$ , and  $I_2^2$ .

$$\begin{aligned} & \frac{\partial}{\partial x} \left[ 2\gamma_{8,3} \frac{\partial I_2^{-2}}{\partial x} - \gamma_{1,1} \frac{\partial I_2^0}{\partial y} + 2\gamma_{7,-3} \frac{\partial I_2^2}{\partial y} + \frac{5}{\alpha_1} \frac{\partial I_0}{\partial y} \right] \\ & + \frac{\partial}{\partial y} \left[ 2\gamma_{8,3} \frac{\partial I_2^{-2}}{\partial y} - \gamma_{1,1} \frac{\partial I_2^0}{\partial x} - 2\gamma_{7,-3} \frac{\partial I_2^2}{\partial x} + \frac{5}{\alpha_1} \frac{\partial I_0}{\partial x} \right] - 2\alpha_2 I_2^{-2} = 0 \end{aligned} \quad (3.48)$$

$$\frac{\partial}{\partial x} \left[ \gamma_{6,1} \frac{\partial I_2^0}{\partial x} - 6\gamma_{1,1} \frac{\partial I_2^2}{\partial x} - 6\gamma_{1,1} \frac{\partial I_2^{-2}}{\partial y} - \frac{5}{\alpha_1} \frac{\partial I_0}{\partial x} \right] + \frac{\partial}{\partial y} \left[ \gamma_{6,1} \frac{\partial I_2^0}{\partial y} + 6\gamma_{1,1} \frac{\partial I_2^2}{\partial y} - 6\gamma_{1,1} \frac{\partial I_2^{-2}}{\partial x} - \frac{5}{\alpha_1} \frac{\partial I_0}{\partial y} \right] - \alpha_2 I_2^0 = 0 \quad (3.49)$$

$$\frac{\partial}{\partial x} \left[ 2\gamma_{8,3} \frac{\partial I_2^2}{\partial x} - \gamma_{1,1} \frac{\partial I_2^0}{\partial x} - 2\gamma_{7,-3} \frac{\partial I_2^{-2}}{\partial y} + \frac{5}{\alpha_1} \frac{\partial I_0}{\partial x} \right] + \frac{\partial}{\partial y} \left[ 2\gamma_{8,3} \frac{\partial I_2^2}{\partial y} + \gamma_{1,1} \frac{\partial I_2^0}{\partial y} + 2\gamma_{7,-3} \frac{\partial I_2^{-2}}{\partial x} - \frac{5}{\alpha_1} \frac{\partial I_0}{\partial y} \right] - 2\alpha_2 I_2^2 = 0 \quad (3.50)$$

$$\frac{\partial}{\partial x} \left[ \frac{5}{\alpha_1} \frac{\partial I_0}{\partial x} - \frac{1}{\alpha_1} \frac{\partial I_2^0}{\partial x} + \frac{6}{\alpha_1} \frac{\partial I_2^2}{\partial x} + \frac{6}{\alpha_1} \frac{\partial I_2^{-2}}{\partial y} \right] + \frac{\partial}{\partial y} \left[ \frac{5}{\alpha_1} \frac{\partial I_0}{\partial y} - \frac{1}{\alpha_1} \frac{\partial I_2^0}{\partial y} - \frac{6}{\alpha_1} \frac{\partial I_2^2}{\partial y} + \frac{6}{\alpha_1} \frac{\partial I_2^{-2}}{\partial x} \right] = 5\alpha_0 (I_0 - 4\pi I_b) \quad (3.51)$$

The coefficients are defined as

$$\begin{aligned} \gamma_{i,j} &= \begin{pmatrix} i \\ \alpha_3 \\ j \\ \alpha_1 \end{pmatrix} \\ \alpha_n &= \begin{cases} (2n+1) & n \geq 1 \\ 1-\omega & n = 0 \end{cases} \end{aligned} \quad (3.52)$$

If anisotropic scattering is considered an additional term appears in the  $\alpha_n$  definition which corresponds to the expansion coefficients of the scattering phase function. Here, we are only considering isotropic scattering so that term is omitted. A more complete derivation is given by Modest and Yang [52].

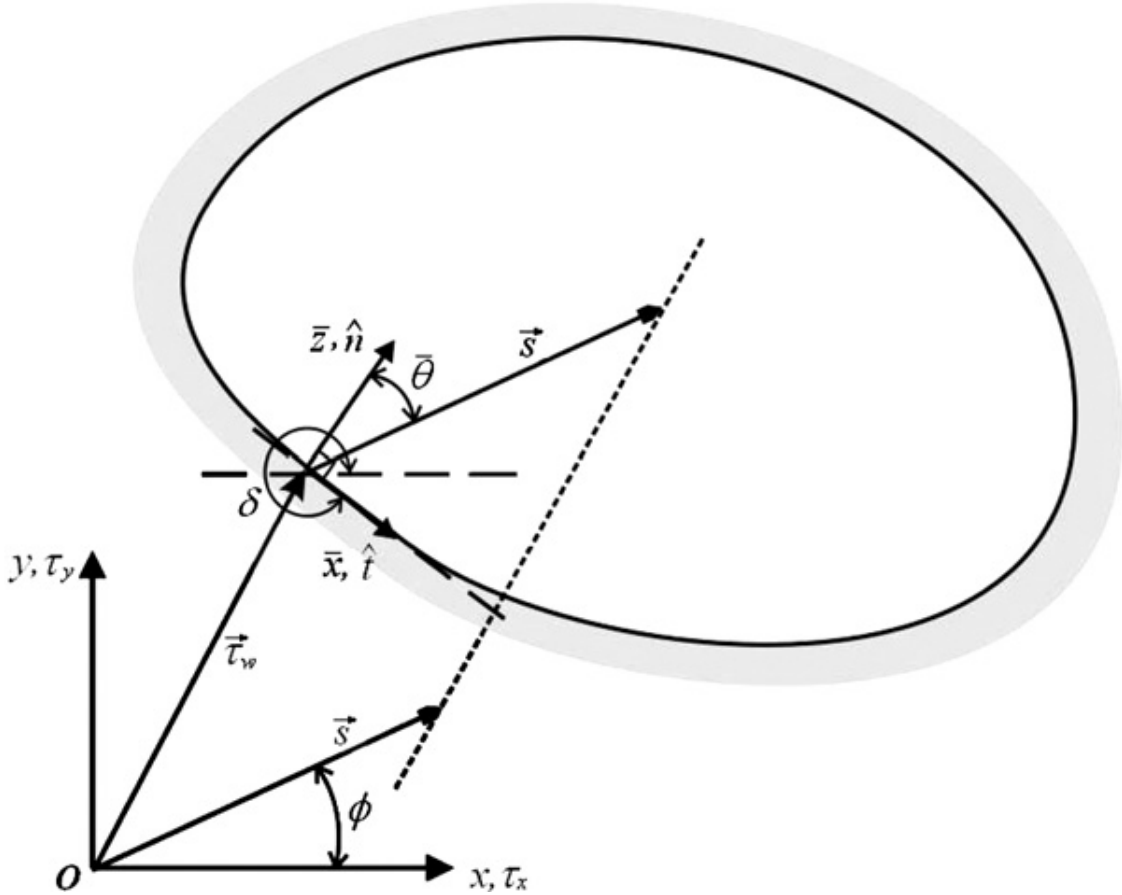


Illustration 3.2: Nomenclature for  $P_3$  boundary conditions [52]

The boundary conditions for the  $P_3$  equations are found by minimizing the approximation error in the surface intensity. Results may vary depending upon the definition of this minimum. The most popular choices are those of Mark [59, 60, 57] and Marshak [61]. The Marshak boundary conditions are considered to be more widely applicable [62] and will be the only ones considered here. The Marshak boundary condition requires that the outgoing intensity at a surface predicted by the  $P_3$  approximation be equivalent to the known outgoing intensity at that surface in the integral sense. That is to say that while the angular distribution of the intensity may be inaccurate at the boundary, the angularly integrated intensity should be correct.

$$\int_{\hat{n} \cdot \Omega > 0} I \bar{Y}_{2i-1}^m d\Omega = \int_{\hat{n} \cdot \Omega > 0} I_s \bar{Y}_{2i-1}^m d\Omega, \quad i = 1, 2, L \cdot \frac{1}{2}(N+1), \text{ all relevant } m \quad (3.53)$$

The overbar on the spherical harmonics in Equation (3.53) indicates the use of the local reference frame as opposed to the global reference frame. The local reference frame is defined relative to the wall normal as shown in Illustration 3.2.

After a great deal of tedious algebra, the final boundary conditions to be used are Equations (3.54)-(3.57). Interested parties may find a more complete derivation in [52].

$$I_0 - \frac{3}{4} \sin(2\delta) I_2^{-2} - \frac{1}{8} I_2^0 - \frac{3}{4} \cos(2\delta) I_2^2 - \frac{12}{5\sigma_T \alpha_1} \frac{\partial}{\partial \bar{x}} [\cos(2\delta) I_2^{-2} - \sin(2\delta) I_2^2] \quad (3.54)$$

$$- \frac{2}{5\sigma_T \alpha_1} \frac{\partial}{\partial \bar{z}} [5I_0 - 6\sin(2\delta) I_2^{-2} - I_2^0 - 6\cos(2\delta) I_2^2] = 4\pi I_s \\ - \frac{3}{2} \cos(2\delta) I_2^{-2} + \frac{3}{2} \sin(2\delta) I_2^2 + \frac{2}{5\sigma_T \alpha_1} \frac{\partial}{\partial \bar{x}} [5I_0 - I_2^0 + 6\sin(2\delta) I_2^{-2} + 6\cos(2\delta) I_2^2] \quad (3.55)$$

$$+ \frac{12}{5\sigma_T \alpha_1} \frac{\partial}{\partial \bar{z}} [\cos(2\delta) I_2^{-2} - \sin(2\delta) I_2^2] = 0 \\ I_0 + 3\sin(2\delta) I_2^{-2} + \frac{1}{2} I_2^0 + 3\cos(2\delta) I_2^2 - \frac{48}{5\sigma_T \alpha_3} \frac{\partial}{\partial \bar{x}} [\cos(2\delta) I_2^{-2} - \sin(2\delta) I_2^2] \quad (3.56)$$

$$- \frac{24}{5\sigma_T \alpha_3} \frac{\partial}{\partial \bar{z}} [3\sin(2\delta) I_2^{-2} + \frac{1}{2} I_2^0 + 3\cos(2\delta) I_2^2] = 4\pi I_s \\ \frac{1}{2} \sin(2\delta) I_2^{-2} - \frac{1}{4} I_2^0 + \frac{1}{2} \cos(2\delta) I_2^2 - \frac{16}{5\sigma_T \alpha_3} \frac{\partial}{\partial \bar{x}} [\cos(2\delta) I_2^{-2} - \sin(2\delta) I_2^2] \quad (3.57)$$

$$- \frac{4}{5\sigma_T \alpha_3} \frac{\partial}{\partial \bar{z}} [2\sin(2\delta) I_2^{-2} - I_2^0 + 2\cos(2\delta) I_2^2] = 0$$

The boundary conditions are in terms of normal and tangential derivatives as well as evaluations of  $I_0$ ,  $I_2^{-2}$ ,  $I_2^0$ , and  $I_2^2$ . Solving for the surface normal derivatives allows for easy input into commercial PDE solvers.

The heat flux on a surface is given by [63]

$$q_n = \frac{6}{5\alpha_1\sigma_T} \left( \frac{\partial I_2^{-2}}{\partial x} \cos\delta + \frac{\partial I_2^{-2}}{\partial y} \sin\delta \right) - \frac{1}{5\alpha_1\sigma_T} \left( \frac{\partial I_2^0}{\partial x} \sin\delta + \frac{\partial I_2^0}{\partial y} \cos\delta \right) \\ + \frac{6}{5\alpha_1\sigma_T} \left( \frac{\partial I_2^2}{\partial x} \sin\delta + \frac{\partial I_2^2}{\partial y} \cos\delta \right) + \frac{1}{\alpha_1\sigma_T} \left( \frac{\partial I_0}{\partial x} \sin\delta + \frac{\partial I_0}{\partial y} \cos\delta \right) \quad (3.58)$$

## SIMPLIFIED SPHERICAL HARMONICS

The simplified spherical harmonics (SPN) equations are (potentially) higher order diffusion-type equations derived from any odd order spherical harmonics (PN) expansion [64]. The SPN approximation has been familiar to the nuclear engineering community for some time [65] but has only recently gained popularity among the heat transfer community [66, 67]. The SPN approximation is not only related to the PN approximation, but to the discrete ordinates (SN) and variable Eddington factor (VEF) approximations as well [68, 69, 70]. The mathematical properties of the SPN equations are analyzed in [71]. Due to the simplified nature of the SPN equations, fast and robust solvers have been implemented for their solution [72].

The most rigorous derivation of the SPN approximation involves diffusively scaling the transport equation and performing an asymptotic expansion of the differential operator [64, 73, 74, 75]. Alternatively, the SPN equations and boundary conditions may be derived from the 1-D PN equations and boundary conditions by replacing 1-D differential operators with equivalent 2-D or 3-D equivalents [76, 65, 77]. A small diffusive scaling parameter is defined as the inverse optical thickness.

$$\epsilon = \frac{1}{\sigma_T x_{ref}} \quad (3.59)$$

For the following asymptotic expansion to be valid, it is required that  $\varepsilon \ll 1$ .

Scaling the streaming operator, we have

$$\left(1 + \frac{\varepsilon}{\sigma_T} \vec{\Omega} \cdot \vec{\nabla}\right) I = (1 - \omega) I_b + \frac{\omega}{4\pi} \int I d\vec{\Omega} \quad (3.60)$$

The operator on the left hand side of Equation (3.60) is inverted using Neumann's series.

$$I = \left(1 - \frac{\varepsilon}{\sigma_T} \vec{\Omega} \cdot \vec{\nabla} + \frac{\varepsilon^2}{\sigma_T^2} (\vec{\Omega} \cdot \vec{\nabla})^2 - \dots\right) \left( (1 - \omega) I_b + \frac{\omega}{4\pi} \int I d\vec{\Omega} \right) \quad (3.61)$$

The resulting equation is angularly integrated over the unit sphere. Using the property that

$$\int_{4\pi} (\vec{\Omega} \cdot \vec{\nabla})^n d\vec{\Omega} = \left[1 + (-1)^n\right] \frac{2\pi}{n+1} \vec{\nabla}^n \quad (3.62)$$

the transport equation becomes

$$cE = \left(1 + \frac{\varepsilon^2}{3\sigma_T^2} \vec{\nabla}^2 + \frac{\varepsilon^4}{5\sigma_T^4} \vec{\nabla}^4 + \dots\right) ((1 - \omega) 4\pi I_b - \omega cE) \quad (3.63)$$

Using Neumann's series again and multiplying by the extinction coefficient yields

$$\left(-\frac{\varepsilon^2}{3\sigma_T} \vec{\nabla}^2 - \frac{4\varepsilon^4}{45\sigma_T^3} \vec{\nabla}^4 - \dots\right) cE = \kappa (4\pi I_b - cE) \quad (3.64)$$

Truncating this series after a certain number of terms and performing a sequence of substitutions provides the corresponding SPN equations. The algebra will be omitted, but interested parties may follow the references [74] for details. The SP1 and P1 equations are equivalent. For 1-D slab geometries, the SPN and PN equations are equivalent as well. However, for more general geometries the SPN equations are fewer and simpler than the corresponding PN equations.

The SP3 approximation may be rewritten as a set of two diffusion equations coupled only through their boundary conditions.

$$-\vec{\nabla} \cdot \left( \frac{\mu_1^2}{\sigma_T} \vec{\nabla} \psi_1 \right) + \kappa \psi_1 = 4\pi \kappa I_b \quad (3.65)$$

$$-\vec{\nabla} \cdot \left( \frac{\mu_2^2}{\sigma_T} \vec{\nabla} \psi_2 \right) + \kappa \psi_2 = 4\pi \kappa I_b \quad (3.66)$$

The constants,  $\mu$  are defined as

$$\begin{aligned} \mu_1^2 &= \frac{3}{7} - \frac{2}{7} \sqrt{\frac{6}{5}} \\ \mu_2^2 &= \frac{3}{7} + \frac{2}{7} \sqrt{\frac{6}{5}} \end{aligned} \quad (3.67)$$

The values of the constants are related to roots of the corresponding Legendre polynomial. The new dependent variables are related to the energy density by

$$\psi_n = E + \frac{5}{7} \left( 1 + (-1)^n \sqrt{\frac{54}{5}} \right) \left( 1 - \frac{11\varepsilon^2}{21\sigma_T^2} \Delta \right)^{-1} \left( \frac{2\varepsilon^2}{15\sigma_T^2} \Delta E \right) \quad (3.68)$$

The radiative heat flux is found to be a linear combination of these two new solution variables.

$$\vec{F} = \frac{-1}{\sigma_T} \vec{\nabla} (a_1 \psi_1 + a_2 \psi_2) \quad (3.69)$$

The relative weights,  $a_1$  and  $a_2$  are found to be

$$a_1 = \frac{1}{30} \left( 5 - 3\sqrt{\frac{5}{6}} \right) \quad (3.70)$$

$$a_2 = \frac{1}{30} \left( 5 + 3\sqrt{\frac{5}{6}} \right)$$

The appropriate boundary conditions for the SPN equations are derived from a variational principle [74, 78, 79]. For nonblack walls the boundary conditions are slightly more complicated and are given in [74]. For black walls, the boundary conditions for the SP3 equations simplify to

$$\alpha_1 \psi_1 + \frac{1}{\sigma_T} (\vec{n} \cdot \vec{\nabla} \psi_1) = -\beta_2 \psi_2 + \eta_1 I_{b,w} \quad (3.71)$$

$$\alpha_2 \psi_2 + \frac{1}{\sigma_T} (\vec{n} \cdot \vec{\nabla} \psi_2) = -\beta_1 \psi_1 + \eta_2 I_{b,w} \quad (3.72)$$

with constant coefficients defined as

$$\begin{aligned}
\alpha_1 &= \frac{5}{96} \left( 34 + 11\sqrt{\frac{6}{5}} \right) & \alpha_2 &= \frac{5}{96} \left( 34 - 11\sqrt{\frac{6}{5}} \right) \\
\beta_1 &= \frac{5}{96} \left( 2 - \sqrt{\frac{6}{5}} \right) & \beta_2 &= \frac{5}{96} \left( 2 + \sqrt{\frac{6}{5}} \right) \\
\eta_1 &= \frac{5\pi}{2} \left( 3 + \sqrt{\frac{6}{5}} \right) & \eta_2 &= \frac{5\pi}{2} \left( 3 - \sqrt{\frac{6}{5}} \right)
\end{aligned} \tag{3.73}$$

In the case of a 1-D slab geometry, these boundary conditions are equivalent to the previously discussed Marshak boundary conditions. The SPN approximations are expected to perform well when the intensity field is almost isotropic and when the diffusive scaling parameter,  $\varepsilon$  is very small.

Solution time for the SPN approximations tends to increase with decreasing optical thickness. This is because the resulting matrix equations become poorly conditioned as the opacity approaches zero. This trend holds true for all of the second order forms regardless of angular approximation.

### COMPARISON OF ANGULAR APPROXIMATIONS

All of the previously discussed angular approximations have advantages and disadvantages. One of the challenges that an analyst faces is the appropriate choice of method. Will the method provide results quickly enough to be useful? Is the method capable of replicating the angular intensity distribution in a particular problem? Will the errors introduced by inaccurately modeling the angular intensity distribution make the solution unusable?

The question of the relative speed of the methods is a complicated one. The wall-clock time for a simulation is dependent not only upon the method employed but also upon the problem, the implementation, and the computer architecture being used to perform the simulation. It is nearly impossible to control for all of these variables and

still provide a useful comparison. This is especially true when considering the rapid advancements in computer architectures. To further complicate matters, some methods like the discrete ordinates method may be modified to minimize processing times for problems with particular geometries and structured grids. The way in which different methods interact with domain decomposition makes the scale of the problem important in determining which method will provide the fastest results.

For this reason, we will focus only on question of accuracy. The question of which method is ‘best’ for a particular problem is left unanswered. The accuracy of a given solution method for a particular test case is defined as the relative error in a heat flux prediction, usually at a boundary. Other quantities of interest such as the radiative flux divergence at a point or within a volume could have been chosen and the resulting accuracies would be different. The relative error in the heat flux prediction is defined in the  $L^2$  sense.

$$\sqrt{\frac{\int (q''_{\text{exact}} - q''_{\text{approx}})^2 ds}{\int (q''_{\text{exact}})^2 ds}} \quad (3.74)$$

A comparison is sought between the accuracy of the different methods for a set of two-dimensional test cases. This set is by no means exhaustive. The cases were chosen to represent a wide array of physical phenomena. The equations were all solved numerically on fine spatial meshes so that spatial discretization error is negligible relative to the errors introduced by the various angular approximations.

## Case 1

Consider first the test problem of a square duct with a single hot wall. The medium is absorbing and isotropically scattering but is non-emitting (cold). All four walls are black. Considering only the black-wall case is sufficient since all of the methods considered perform best in cases with nearly isotropic intensity and reflecting walls tend to reduce anisotropy in the intensity. Additionally, only the case of a single hot wall need be considered for this geometry since superposition allows for any combination of the walls to be heated. Non-isothermal walls present an additional complication and are included in Case 3. An analytical series solution to this problem has been developed by Crosbie and Schrenker [37]. This technique was later expanded to inhomogeneous media with isotropic scattering [38]. Due to the discontinuous boundary conditions, the low order discrete ordinates methods perform poorly and exhibit distinctive ‘ray-effects.’ Although a number of techniques have been developed to mitigate ray-effects, they have proven to be highly problem dependent [80]. Because of the variability of the effectiveness of any one of these techniques no efforts to mitigate ray-effects are included here.

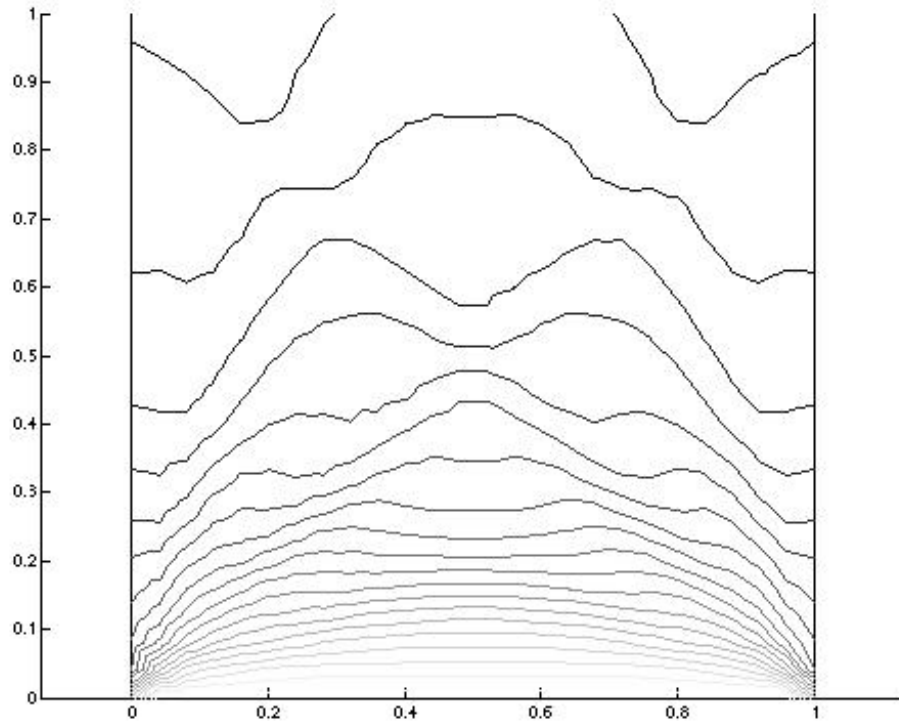


Illustration 3.3: Depiction of ray-effects in low-order ( $N=6$ ) discrete ordinates solutions; contours of radiative energy density in medium from Case 1 with unity optical side-length and no scattering

The relative error is found to be greatest when calculating the heat flux on the wall opposite the hot wall. The spatially varying heat flux on the top wall is calculated with each of the methods.

The relative error is calculated in the  $L^2$  sense and plotted as a function of optical thickness and scattering albedo in order to quantify the sensitivity of the error to these parameters. Illustration 3.3 shows the oscillatory solution for the radiative energy density calculated using the  $P_N-T_N$  quadrature with  $N=6$ . Ray effects completely dominate the solution for lower order cases. It is noted that the shape of the error contours is common for all orders of  $S_N$ .

Like all the methods considered, the relative error is minimized for optically thick, purely scattering media. The intensity is nearly isotropic for these cases and the angular dependence is represented well by each of the methods.

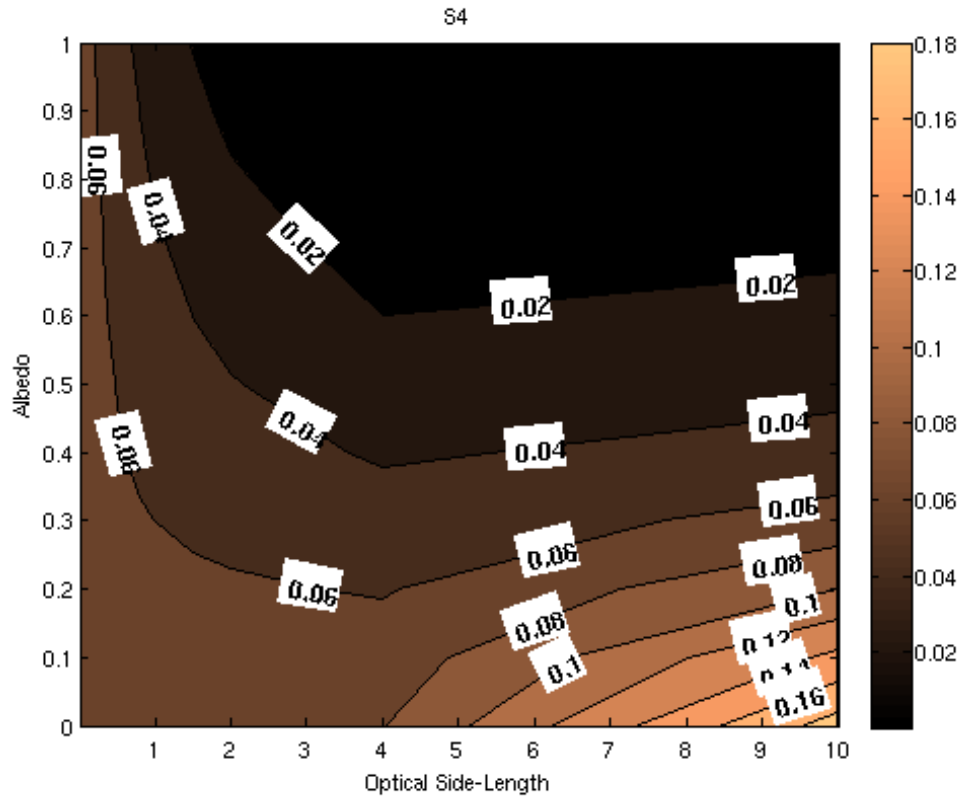


Figure 3.3: Relative error in the  $S_4$  prediction of Case 1 heat flux; Square enclosure with single hot wall and homogeneous participating medium. Error reported is the  $L^2$  norm of the error in the heat flux prediction on the wall opposite the hot wall

As the order increases, the relative error decreases for all parameter values. However, the general behavior remains unchanged. For this reason, only the error in discrete ordinate approximations of order less than or equal to the  $S_8$  solution will be plotted for additional cases. As the discrete ordinates approximation order is increased the error becomes less and less sensitive to the optical thickness.

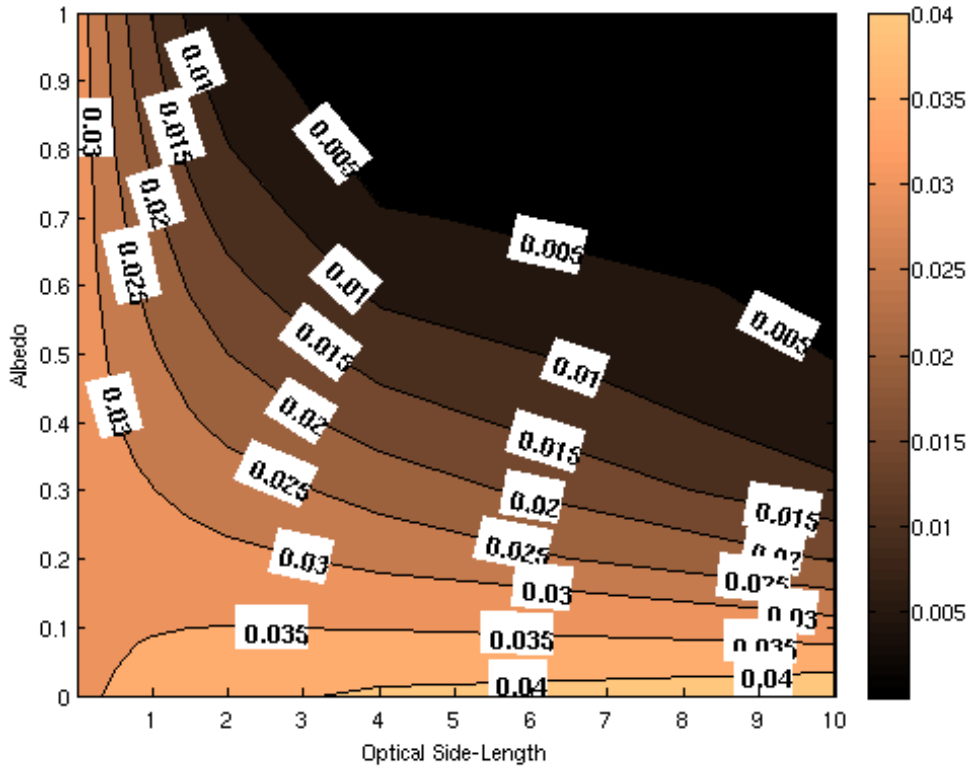


Figure 3.4: Relative error in the  $S_6$  prediction of Case 1 heat flux; Square enclosure with single hot wall and homogeneous participating medium. Error reported is the  $L^2$  norm of the error in the heat flux prediction on the wall opposite the hot wall

The M1 method error has a similar parametric dependence to the discrete ordinates method for this problem. It is observed to be generally less accurate than the  $S_6$  method. However, there are many applications where it would remain preferable since it involves only a single unknown and produces smooth solutions. It is also noted that absent an internal source that the full capability of the M1 method remains untested. The flux-limiter is not spatially varying in this example problem although the method allows for it to vary spatially.

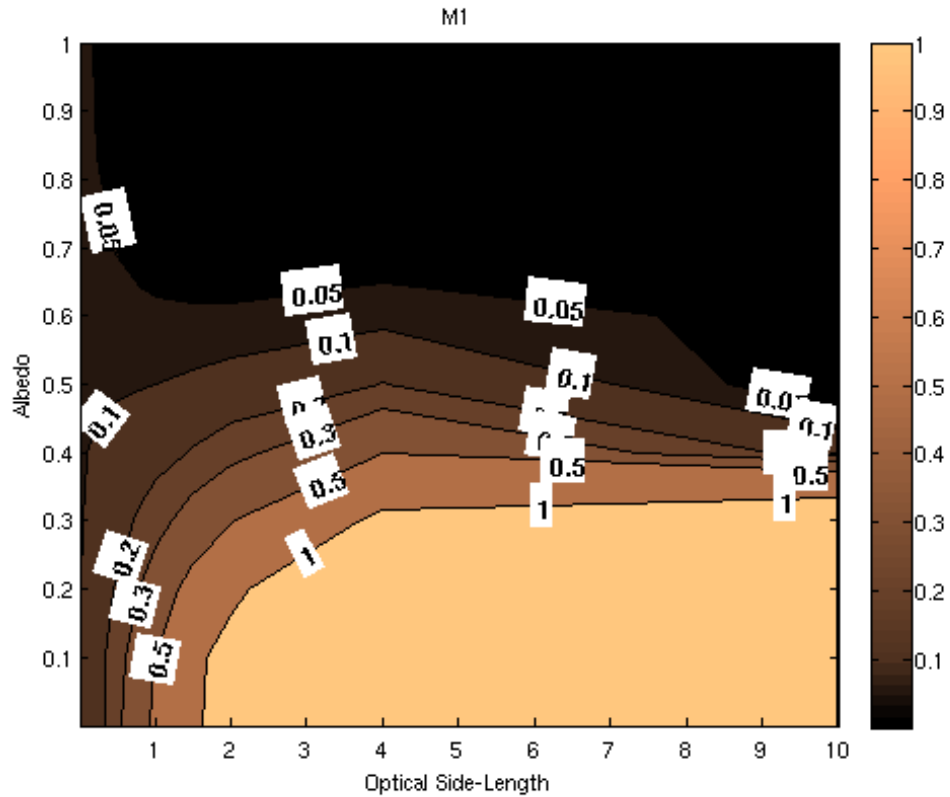


Figure 3.5: Relative error in the M1 prediction of Case 1 heat flux; Square enclosure with single hot wall and homogeneous participating medium. Error reported is the  $L^2$  norm of the error in the heat flux prediction on the wall opposite the hot wall

The contours are essentially horizontal for optical thicknesses larger than 5. The accuracy of the M1 method for large optical thicknesses is a function only of the scattering albedo.

The P1 method behaves entirely differently than the other methods. For small optical thicknesses ( $\tau_L < 1$ ), the error is almost entirely independent of the scattering albedo.

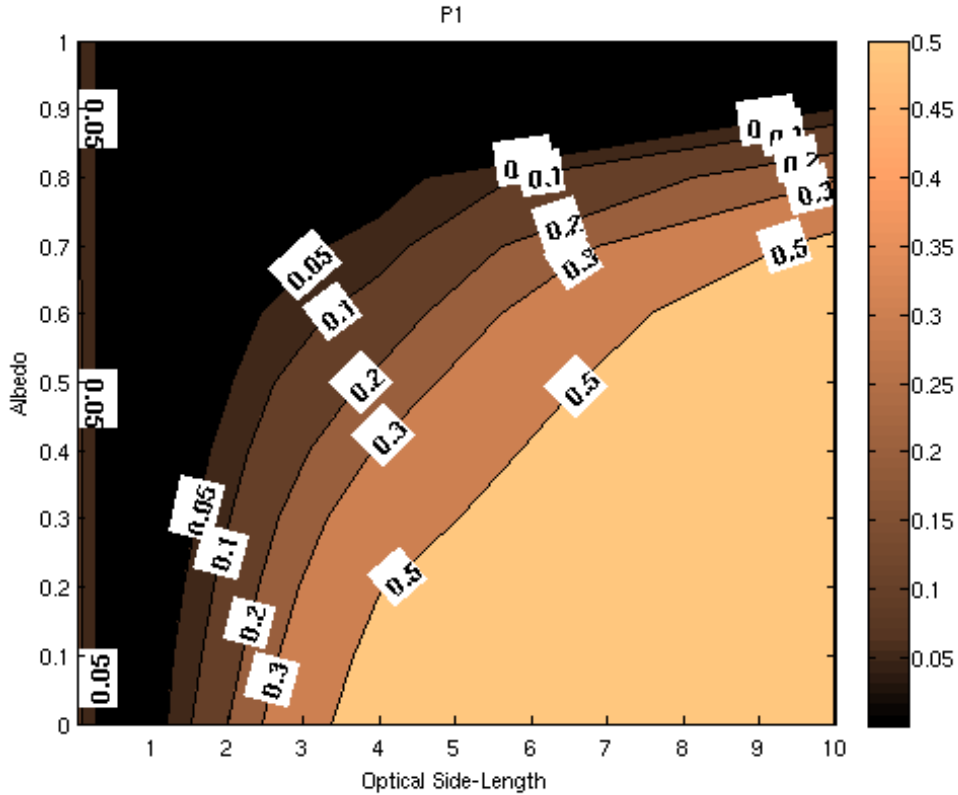


Figure 3.6: Relative error in the P1 prediction of Case 1 heat flux; Square enclosure with single hot wall and homogeneous participating medium. Error reported is the  $L^2$  norm of the error in the heat flux prediction on the wall opposite the hot wall

The P1 method is seen to be significantly more accurate than the M1 method for optical thicknesses approaching unity but less accurate for some highly scattering optically thick cases.

The P3 method is seen to be less accurate than the P1 method for predicting the flux of interest for this case. This counterintuitive result is consistent with observations in the literature involving this geometry [52]. In addition, geometries where only a portion of the bottom wall is heated have been reported to result in nonphysical behavior (negative energy density) in the corner regions. The P3 method is seen to outperform the

P1 method in the prediction of other quantities of interest such as the side-wall heat flux and the shape of the energy density contours. However, its relative failings in predicting our ‘conservative’ quantity of interest are concerning.

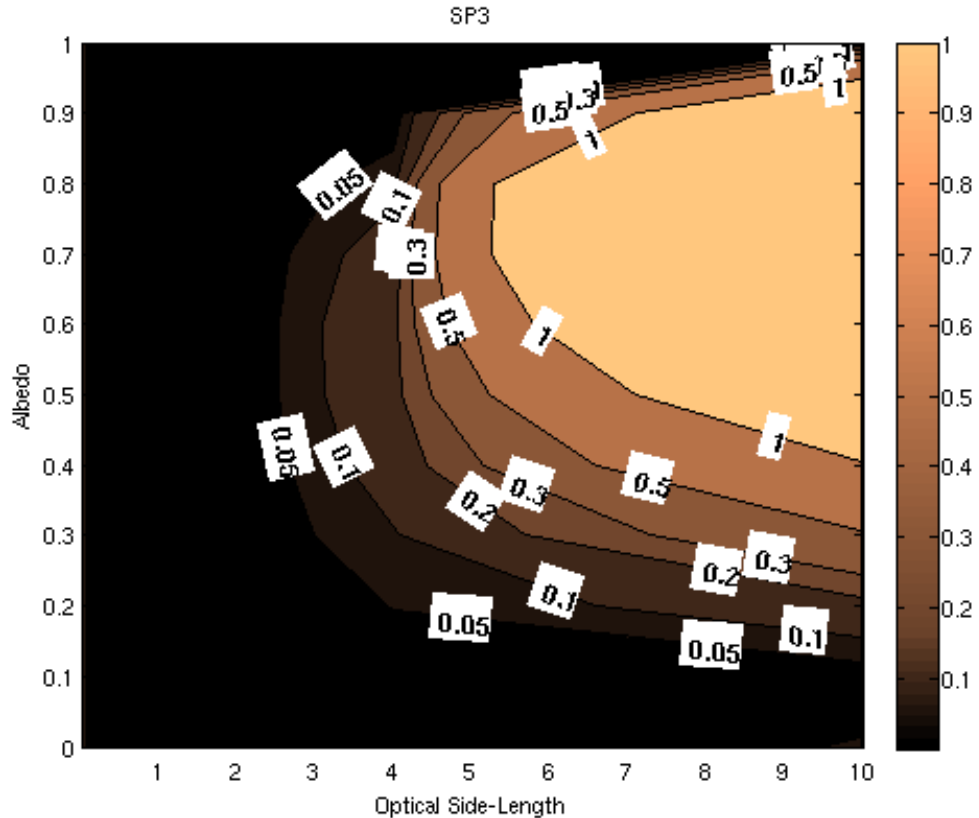


Figure 3.7: Relative error in the SP3 prediction of Case 1 heat flux; Square enclosure with single hot wall and homogeneous participating medium. Error reported is the  $L^2$  norm of the error in the heat flux prediction on the wall opposite the hot wall

The SP3 approximation performs reasonably well for this case, outperforming the P1 and M1 methods in the optically thin and low scattering regimes. It does produce large errors for optically thick cases with intermediate levels of isotropic scattering. This apparently odd error behavior is a result of two competing interests. The SP3

approximation performs well when the solution is either nearly isotropic or locally 1D. That is, that the direction of the energy density gradient varies slowly in space. In this problem, the solution is not nearly isotropic for optically thick cases unless the scattering albedo is very large. Additionally, the presence of the cold side walls makes the solution inherently 2D away from the symmetry plane. Large opacities exacerbate this problem if the scattering albedo is not large enough to compensate or low enough to limit the influence of the boundary conditions.

## Case 2

As a second example problem, consider another square enclosure. The boundaries are cold and black. There is a circle in the center of the domain with a uniform temperature and a zero scattering albedo and unity absorption coefficient. Outside the circle, the medium is cold and has uniform absorption and isotropic scattering cross-sections. The circle is of a size such that the square of the radius is one tenth of the side-length. The optical side-length is computed using the extinction coefficient outside of the source circle.

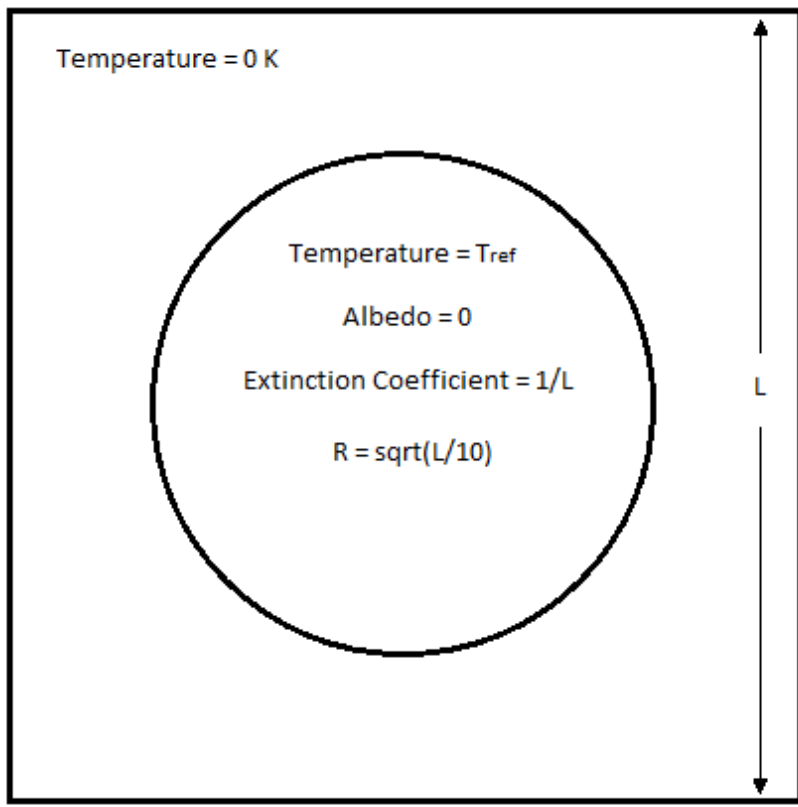


Illustration 3.4: Case 2 geometry explanation; infinitely long hot cylinder surrounded by homogeneous moderator

The discrete ordinates method demonstrates the same error behavior for this case as for the previous example. The error in this example is seen to be relatively smaller for both the  $S_6$  and  $S_8$  approximations. This is partially attributed to the decreased optical distance between the source and the walls as well as the volumetrically distributed nature of the source. The lack of any discontinuities in the boundary conditions is also credited with some decrease in overall error.

Successively higher order discrete ordinates approximations were taken until sufficient convergence was observed. The relative errors plotted in figures 3.8 – 3.13 are

computed using the heat flux corresponding to the highest order discrete ordinates solution as a reference.

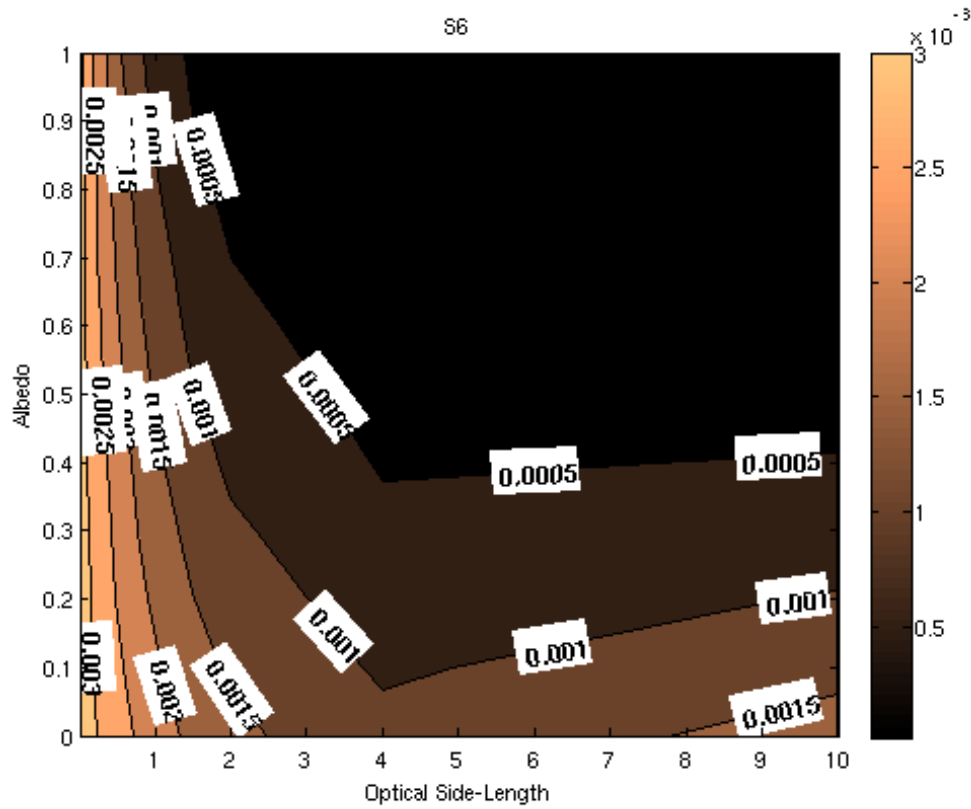


Figure 3.8: Relative error in the  $S_6$  prediction of Case 2 heat flux; infinitely long hot cylinder surrounded by homogeneous moderator. Error reported is the  $L^2$  norm of the error in the heat flux prediction on a plane perpendicular to the axis of the cylinder

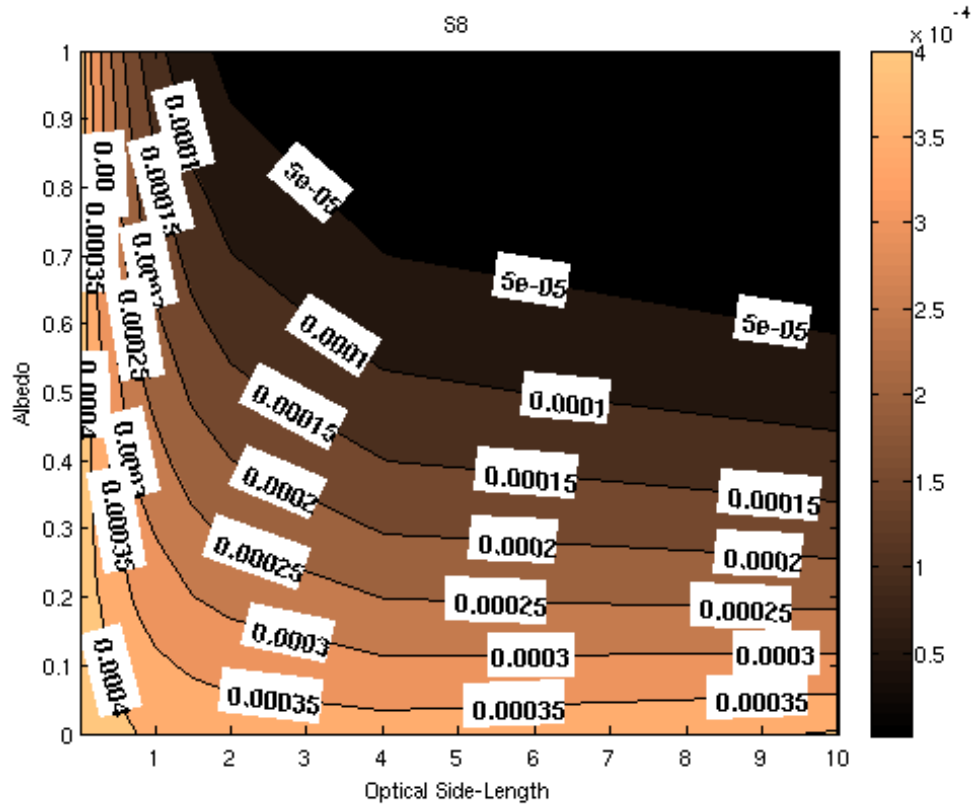


Figure 3.9: Relative error in the  $S_8$  prediction of Case 2 heat flux; infinitely long hot cylinder surrounded by homogeneous moderator. Error reported is the  $L^2$  norm of the error in the heat flux prediction on a plane perpendicular to the axis of the cylinder

The M1 method does not perform very well for this case for small to moderate optical thicknesses or low scattering albedos. Generally speaking, conditioning becomes an issue as optical thickness decreases. The intensity distribution becomes increasingly anisotropic as the scattering albedo decreases which results in large errors for these low-order approximations. The oscillatory heat flux provided by the discrete ordinates approximation may be reasonably close when integrated over a sufficiently large spatial area but is unsatisfactory qualitatively.

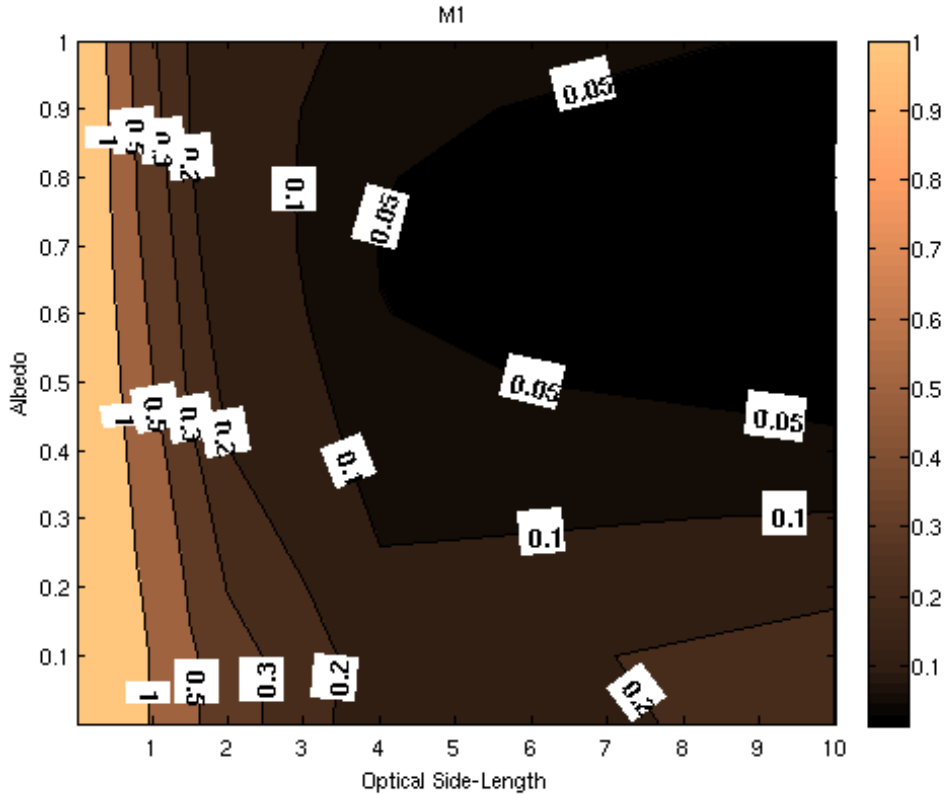


Figure 3.10: Relative error in the M1 prediction of the Case 2 heat flux; infinitely long hot cylinder surrounded by homogeneous moderator. Error reported is the  $L^2$  norm of the error in the heat flux prediction on a plane perpendicular to the axis of the cylinder

The P1 approximation provides a generally more accurate solution than the M1 method for this case. This contradicts the expectation that the M1 method would be particularly advantageous for this type of problem [43]. This expectation was based primarily upon the performance of the M1 method in 1-D test cases and comparisons for a particular pool fire. In the cited study, the M1 method is compared to Monte-Carlo results, the discrete transfer method, and a pair of discrete ordinates quadrature schemes. It was seen to perform well when predicting the energy density (as was observed here). However, in that study as well as this one, significant errors are shown in the radiative

heat flux. Since most methods predict the energy density more accurately than the heat flux, the error in the heat flux is reported here as a conservative representation.

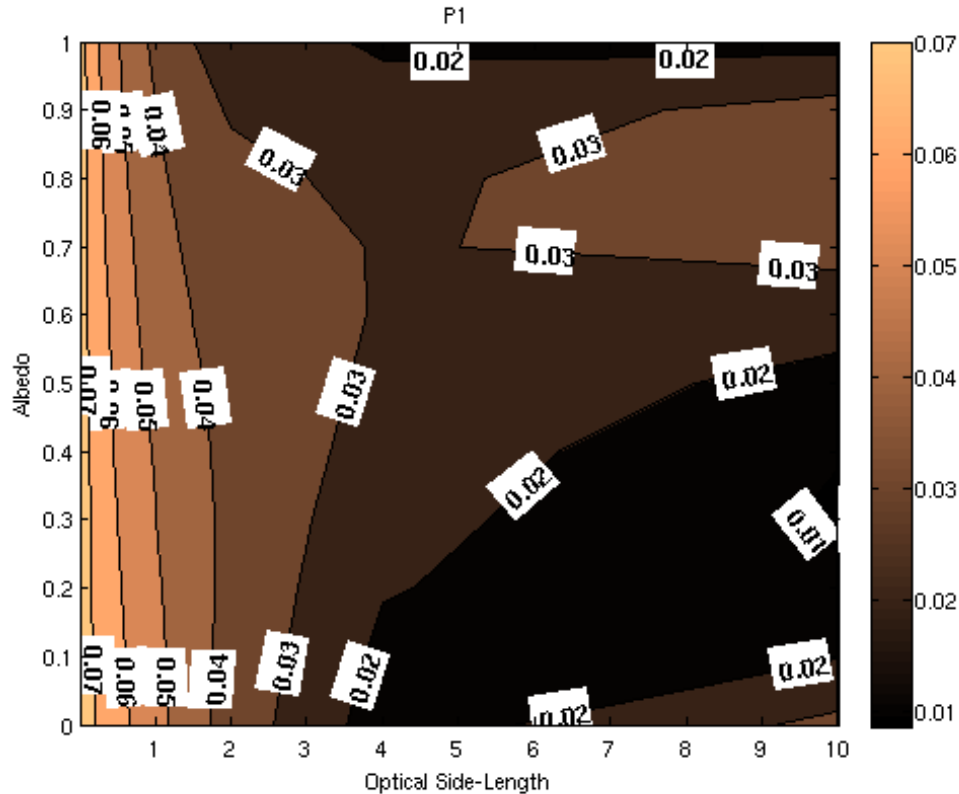


Figure 3.11: Relative error in the P1 prediction of the Case 2 heat flux; infinitely long hot cylinder surrounded by homogeneous moderator. Error reported is the  $L^2$  norm of the error in the heat flux prediction on a plane perpendicular to the axis of the cylinder

In 1-D cases, the M1 method is capable of accurately modeling streaming in either the positive or negative direction. However, the method becomes unstable when multiple directions are significant. In 2-D cases with 1-D or 2-D sources it appears that multiple directions are often significant and the M1 method offers little improvement over the P1 method. The M1 and P1 method both produce consistently smooth results.

This is an advantage over discrete ordinates schemes whose oscillatory predictions can cause stability issues in multi-mode heat transfer codes.

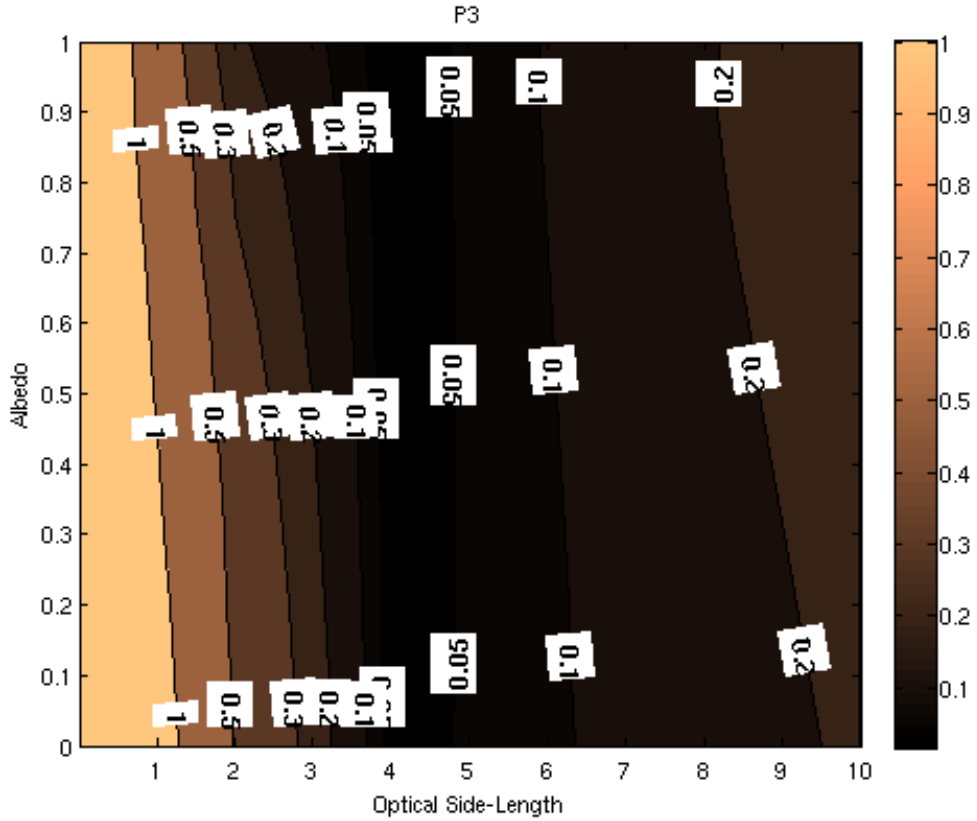


Figure 3.12: Relative error in the P3 prediction of the Case 2 heat flux; infinitely long hot cylinder surrounded by homogeneous moderator. Error reported is the  $L^2$  norm of the error in the heat flux prediction on a plane perpendicular to the axis of the cylinder

The P3 method once again fails to accurately predict the wall heat flux. Additionally, large residuals are present near the corners of the geometry requiring additional mesh refinement in those regions. The poor behavior near the boundaries and in particular near the corners is attributed to the intensity being uniformly zero over a

large portion of the angular domain [52]. This leads to an under prediction of the intensity near the boundaries and especially in the corners.

Once again, the P3 method reproduces the energy density distribution in a qualitative sense. However, it fails to accurately predict the wall heat fluxes which are the quantities of interest for this case. The lack of physical meaning for the three additional spherical harmonic coefficients makes intuitive interpretation of these results difficult. However, it is safe to assume that the PN solutions do not converge monotonically at all orders for these problems. Therefore, care should be taken when applying the P3 method to new applications.

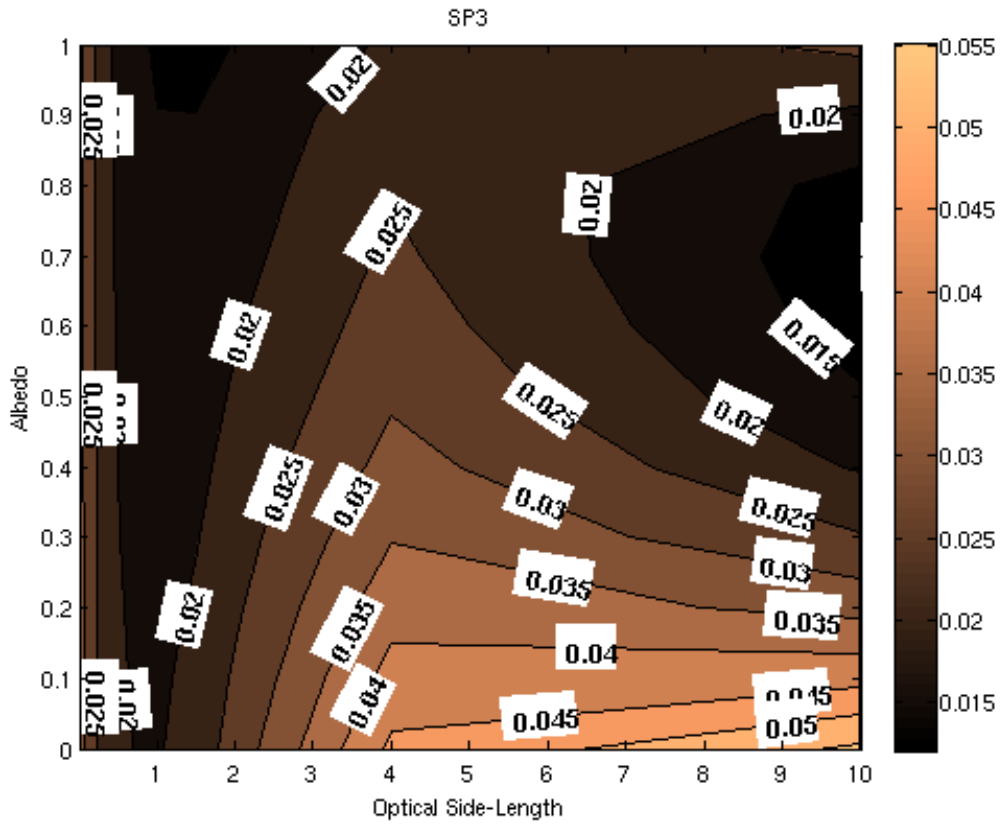


Figure 3.13: Relative error in the SP3 prediction of the Case 2 heat flux; infinitely long hot cylinder surrounded by homogeneous moderator. Error reported is the  $L^2$  norm of the error in the heat flux prediction on a plane perpendicular to the axis of the cylinder

The SP3 approximation performs exceptionally well for this problem. The localized source in the center of the geometry generates a solution that is locally 1D everywhere within the domain. The SP3 approximation results in relative errors less than 6% regardless of optical thickness or scattering albedo. Greater accuracy should be expected from higher order SPN approximations. Additionally, the SPN solutions do not generate ray effects which remain a prominent feature of the discrete ordinates solutions for this problem.

### Case 3

A third case is also considered. Like Case 1, the geometry is a square enclosure with black walls and a medium with uniform optical properties. The top wall temperature is held constant at 500K while the bottom wall temperature is held constant at 300K. It is assumed that the problem is conduction dominated yielding a linear temperature distribution within the medium and on both side walls.

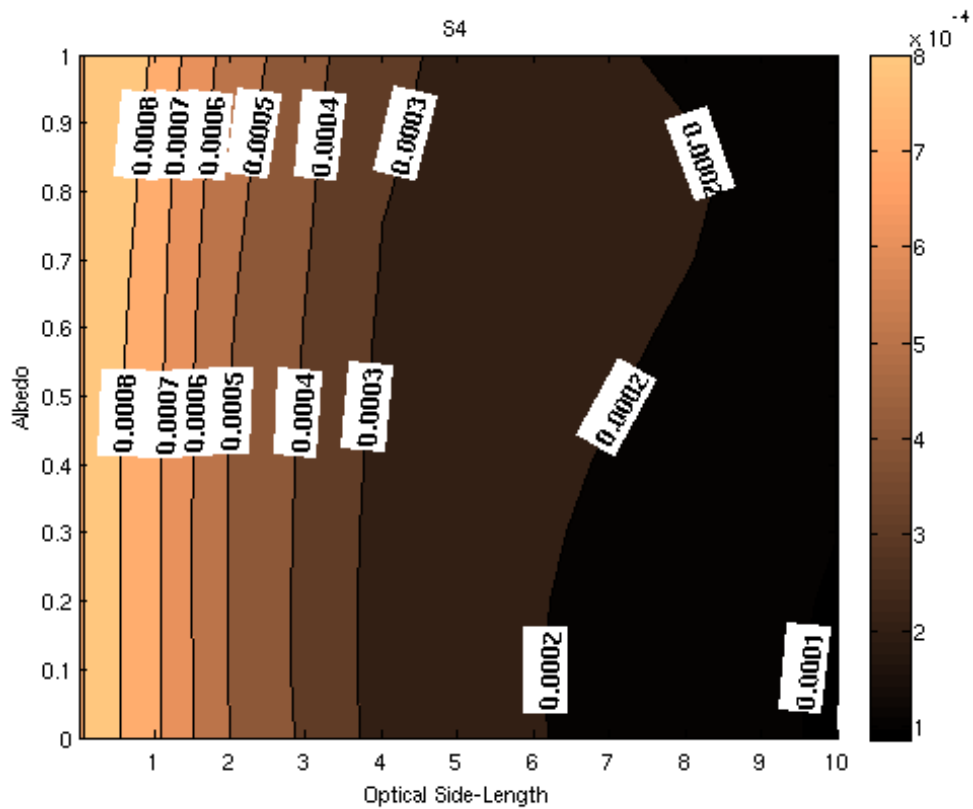


Figure 3.14: Relative error in the  $S_4$  prediction of the Case 3 heat flux; square medium with a linearly varying temperature profile with temperature gradient parallel to two walls. Error reported is the  $L^2$  norm of the error in the heat flux prediction on low temperature wall

The discrete ordinates approximations provide very accurate results for this case. There are no discontinuities in the volumetric source, boundary conditions, or optical

properties. The result is a smooth and accurate solution from even lower order discrete ordinates approximations.

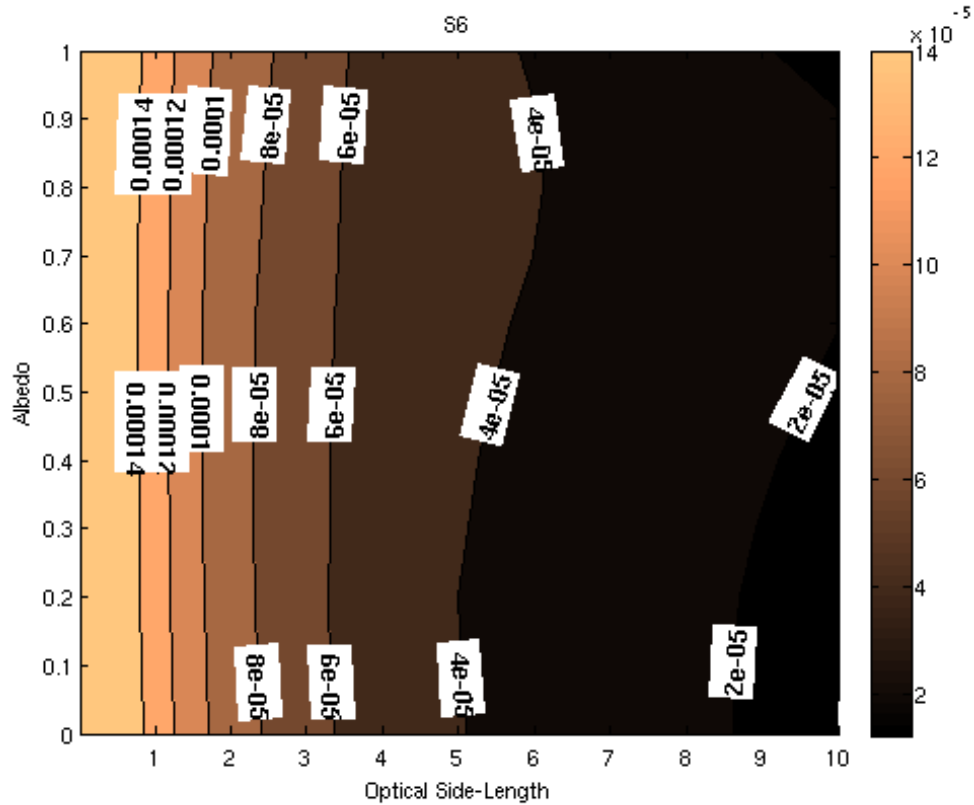


Figure 3.15: Relative error in the  $S_6$  prediction of the Case 3 heat flux; square medium with a linearly varying temperature profile with temperature gradient parallel to two walls. Error reported is the  $L^2$  norm of the error in the heat flux prediction on low temperature wall

Higher-order approximations than  $S_6$  are seen to be nearly identical for this case. The error in the heat flux predictions of the discrete ordinates method is nearly independent of scattering albedo for the range of opacities considered. This behavior is consistent with the previous cases for small opacities.

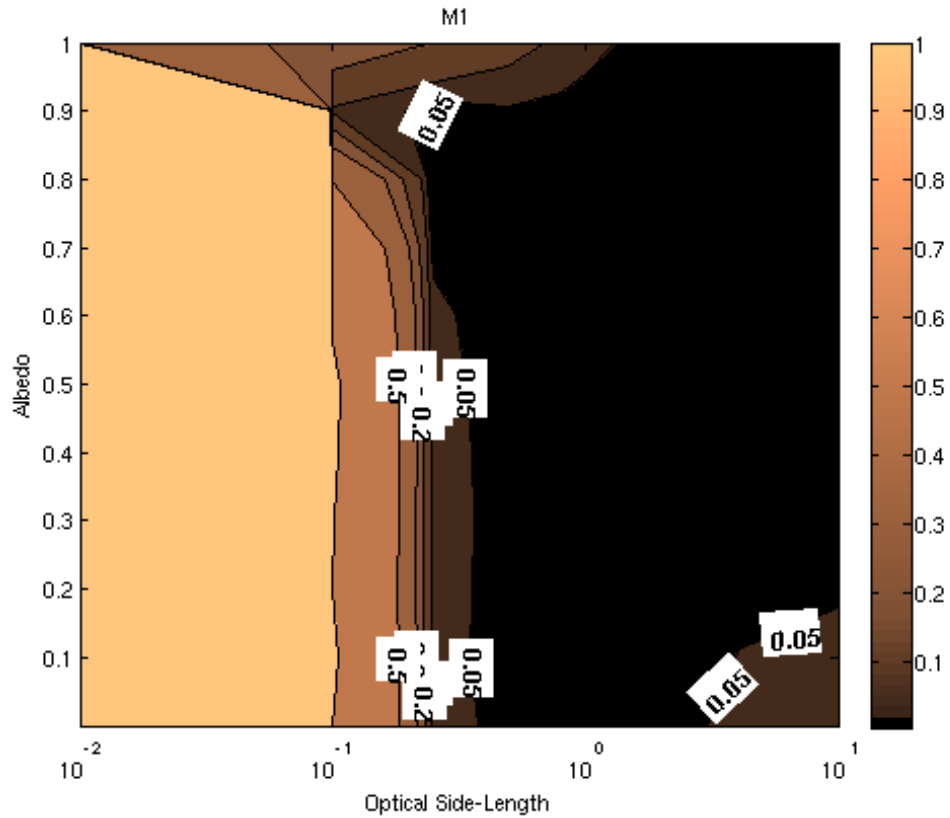


Figure 3.16: Relative error in the M1 prediction of the Case 3 heat flux; square medium with a linearly varying temperature profile with temperature gradient parallel to two walls. Error reported is the  $L^2$  norm of the error in the heat flux prediction on low temperature wall

The M1 method is seen to perform poorly for optical thicknesses below 1 for this case. The reason for this is similar to the explanation of the poor performance of all methods at small optical thicknesses.

The equations become more ill-conditioned as the optical thickness decreases. Additionally, the temperature gradient within the medium adds to the nonlinearity of the M1 equation. Large optical thicknesses provide increased accuracy as do scattering albedos approaching unity.

Like the discrete ordinates approximations, the P1 error is largely independent of albedo. The errors are seen to be less than for the M1 method for small optical thicknesses, but much greater for intermediate and large optical thicknesses. Since both methods are essentially invalid at small optical thickness, it may be said that the M1 method provides a more accurate solution for this case than the P1 method. However, neither is as accurate as the  $S_4$  or SP3 approximations.

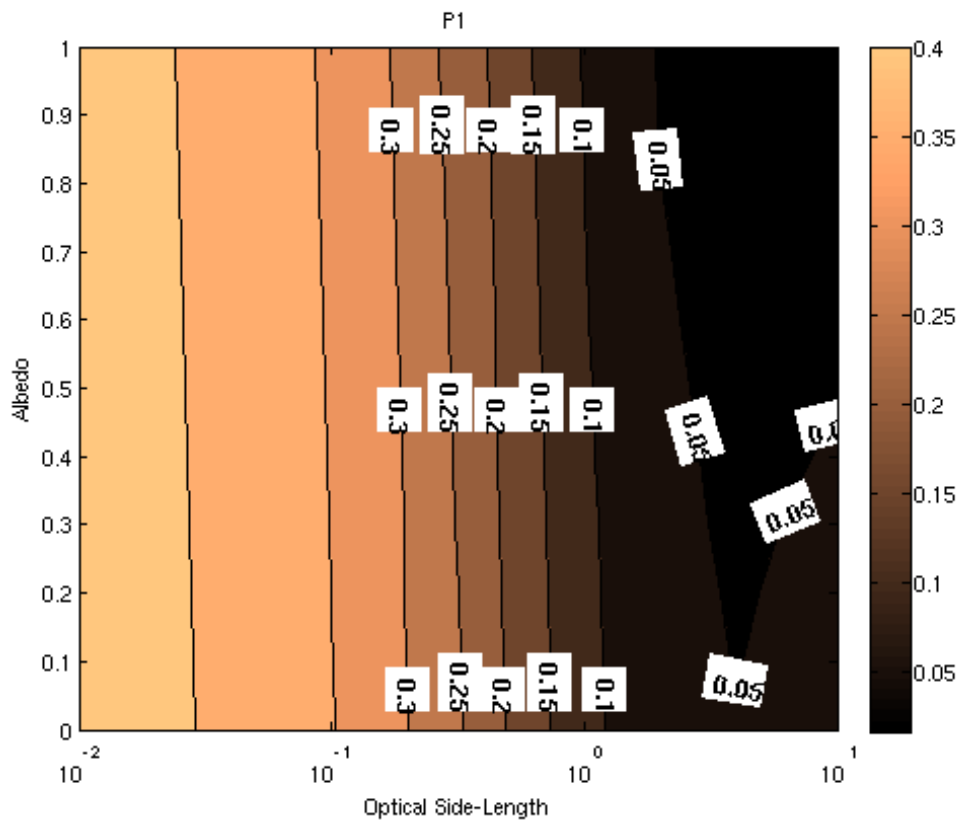


Figure 3.17: Relative error in the P1 prediction of the Case 3 heat flux; square medium with a linearly varying temperature profile with temperature gradient parallel to two walls. Error reported is the  $L^2$  norm of the error in the heat flux prediction on low temperature wall

It might be suggested that distance from the nearest discontinuity be used as a more meaningful length scale for describing the error of the discrete ordinates

approximation. This is reasonable because the ray effects emanating from a discontinuity dominate the error behavior in problems with strong discontinuities such as Case 1 and Case 2.

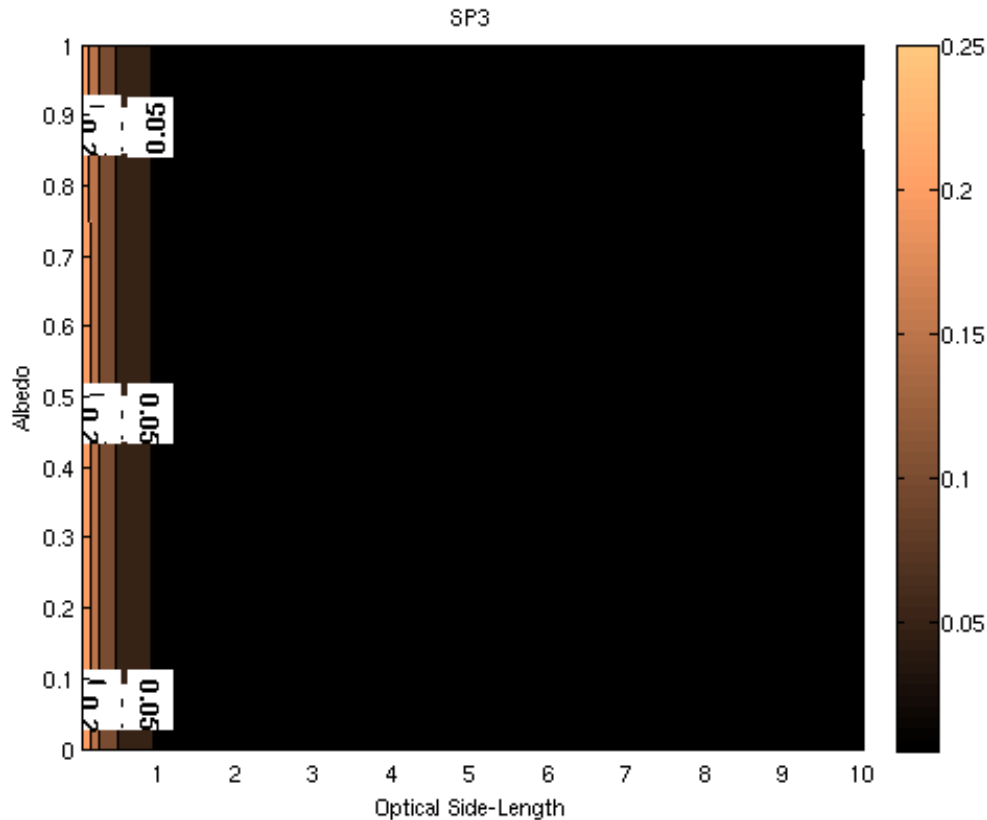


Figure 3.18: Relative error in the SP3 prediction of the Case 3 heat flux; square medium with a linearly varying temperature profile with temperature gradient parallel to two walls. Error reported is the  $L^2$  norm of the error in the heat flux prediction on low temperature wall

The SP3 approximation is seen to produce smaller errors than the P1 or M1 approximations everywhere within the parameter space for this problem. However, significant errors are present as the optically thin limit is approached. The SP3 results are

seen to be independent of scattering albedo for the third test problem. All of the methods demonstrated this lack of sensitivity to the scattering albedo for this particular case.

### ANGULAR APPROXIMATION CONCLUSIONS

Consistent with the literature, the first-order discrete ordinates equations were seen to be more accurate than the second-order equations of the same order [81]. However, the second order formulation requires half the number of unknowns and consequently requires less memory than the first-order alternative. This disadvantage of the first-order form may be mitigated or even eliminated by taking advantage of the sparse nature of the resulting matrix equations when performing scattering source iterations. The second-order formulation does not require additional stabilization in order to be solved using traditional Petrov-Galerkin finite element methods.

Examining the convergence of each of the quadrature sets demonstrated that the  $P_N-T_N$  and level symmetric sets provide the fastest convergence. Since the level symmetric scheme is restricted in the maximum allowable number of ordinate directions, the  $P_N-T_N$  quadrature set is recommended.

The M1 method is shown to be advantageous over the P1 method for a very small subset of the test space for the first 2 problems considered. Since the M1 method is nonlinear and potentially unstable, it is not recommended for 2-D problems of this type. The M1 method does have several nice properties such as being flux limited and outperformed the P1 method for intermediate and large optical thicknesses in the conduction dominated Case 3.

The SP3 approximation is seen to be superior to the P1 and M1 approximations for applications where the solution tends to be locally 1-D. Only one of the cases considered, Case 1 exploited its deficiency in non-locally 1-D applications. It is further

suggested that a very wide class of problems yield locally 1-D solutions and therefore lend themselves to solution by the SPN approximation methods. Higher order SPN approximations are expected to yield greater accuracy, particularly in the diffusion limit. However, it is not expected that the shortcomings of the SPN approximations when the solution is truly 2-D or 3-D will be significantly mitigated by the inclusion of additional terms in the asymptotic expansion.

The discrete ordinates methods are seen to be highly accurate in problems without ray-effect inducing discontinuities. For problems with such features, the large number of ordinate directions required to mitigate the ray-effect oscillations may make the discrete ordinates methods computationally intractable.

Of the low-order angular approximations considered, the SP3 method outperformed the M1, P1, and P3 methods in situations when the solution was approximately locally 1-D. When the solution was fully 2-D, the P1 method appeared to provide the most effective trade-off between accuracy and computational expense although there were regions where the M1 and P3 methods were more accurate than the P1 method.

## Chapter 4: Spectral Integration

The spectral integration of the intensity presents a unique challenge for uncertainty quantification. The absorption coefficient as a function of wavenumber is a sum of hundreds of thousands of individual lines. Assuming Lorentz profiles for the line shapes, each line is defined by three different parameters: a location parameter, a width parameter, and an intensity parameter. Treating all of these parameters individually is not feasible for problems of interest in much the same way that solving the RTE using a line-by-line approach is impractical for most problems. There have been numerous techniques developed to make the evaluation of the spectrally integrated intensity tenable for real problems.

### USING HITRAN AND HITEMP SPECTRAL DATABASES

Spectral databases like HITRAN [82] or HITEMP [83] provide a list of all transitions that a gas molecule may undergo in the process of absorbing a photon. Each transition is described by a number of parameters. For our application, the most important parameters are the transition wavenumber ( $\nu$ ), line intensity ( $S$ ), and line width ( $\gamma$ ). The databases provide this information for a reference state. For the HITRAN and HITEMP databases, that reference state corresponds to a temperature of 296K and a pressure of 1atm. Since 2001, the HITRAN and HITEMP databases have used a 160 character format to describe each transition. This format is detailed in Appendix C. The HITRAN database has recently been updated with the release of HITRAN 2012 [84]. These updates have not been incorporated in the results presented here.

In order to extrapolate this information to other states, additional parameters are tabulated. These parameters include the air-broadened line width ( $\gamma_{air}$ ), temperature

dependence exponent ( $n_{air}$ ), and the pressure shift ( $\delta_{air}$ ). The pressure broadened absorption line half-width is given by (4.1).

$$\gamma_{air}(T) = \gamma_{air}(T_0) \left( \frac{p}{p_0} \right) \left( \frac{T_0}{T} \right)^{n_{air}} \quad (4.1)$$

The exponent,  $n_{air}$  is determined empirically and tabulated in the HITEMP database. The adjusted line intensity is given by (4.2).

$$S_i(T) = S_i(T_0) \frac{\exp\left(-hcE_{L,i}/\sigma T_0\right)}{\exp\left(-hcE_{L,i}/\sigma T\right)} \frac{Q_T(T_0)}{Q_T(T)} \frac{1 - \exp\left(-hcv_{0,i}/\sigma T\right)}{1 - \exp\left(-hcv_{0,i}/\sigma T_0\right)} \quad (4.2)$$

The total internal partition sums,  $Q_T$  are recorded in a separate data file and provided along with the HITRAN or HITEMP database. Values for  $Q_T$  are given in 1K increments over a temperature range of 70 – 3000K [85, 86].

The HITEMP2010 spectral database includes 11,193,608 transitions for CO<sub>2</sub> and 114,241,164 transitions for H<sub>2</sub>O. For each transition, a Lorentz line shape is used. This is appropriate for heat transfer applications at moderate temperatures and pressures.

$$f(\nu - \nu_i) = \frac{\gamma_i/\pi}{(\nu - \nu_i)^2 + \gamma_i^2} \quad (4.3)$$

For low pressure systems, Doppler broadening dominates and the Voigt profile is more appropriate [87, 88]. The monochromatic absorption cross-section for a given wavenumber is found by summing the contributions from each individual line.

$$C(\nu) = \sum_i S_i f(\nu - \nu_i; \gamma_i) \quad (4.4)$$

Since there are millions of terms in the summation in (4.4) and the line widths tend to be narrow relative to the spectral range of interest, the summation is carried out over only those lines which contribute significantly to  $C(\nu)$ . Usually, absorption lines with centers within  $25 \text{ cm}^{-1}$  of  $\nu$  are used. Using equations (4.1) - (4.4) and the default units provided by the HITEMP database, the molecular absorption cross-section,  $C(\nu)$  has units [ $\text{cm}^2 / \text{molecule}$ ].

This allows for the continuous definition of the absorption cross-section as a function of wavenumber. In order to numerically solve the radiative transport equation with this absorption cross-section, it must be discretized. The spectral region of interest is subdivided into a series of intervals over which the absorption cross-section may be assumed to be constant. In order to resolve the complex spectral behaviour of the absorption cross-section, the size of these spectral intervals should be less than a characteristic line half-width. The very large number of intervals required is the reason that line-by-line solutions of the radiative transport equation are so expensive.

Band models seek to define representative optical properties within specified wavenumber intervals. It is observed that variations in line intensity have a significant effect on the radiative transport while variations in line width have a relatively smaller impact [89]. It is assumed that all lines within a given band have the same width. The three most common narrow-band models are those of Elsasser, Goody, and Malkmus.

In the Elsasser narrow-band model the lines within a given band are assumed to follow a Lorentz profile and have equal intensity, spacing, and half-width. The lines are assumed to overlap.

In the Goody narrow-band model the lines are again assumed to follow Lorentz profiles with equal widths. Furthermore, the lines are assumed to be randomly positioned within the band. The line intensities are exponentially distributed.

In the Malkmus narrow-band model the line positions are randomly distributed as in the Goody model. The line intensities are also randomly distributed but follow a different distribution. The intensity distribution is cut off above a maximum intensity and below a minimum intensity. The line intensities are exponentially distributed for high-intensity lines as in the Goody model. For low-intensity lines, the distribution is modified to be proportional to the inverse of the intensity. This modification constitutes an improvement over the Goody model [90].

The exponential wide-band model is an empirical correlation in terms of the integrated band intensity ( $\alpha$ ), the line-width parameter ( $B$ ), and the bandwidth parameter ( $\omega$ ). The total band absorption ( $\bar{A}$ ) is found using provided correlations. The necessary parameters have been tabulated for many different gases [91, 92, 93, 94, 95, 96, 97, 98]. The exponential wide-band model is less computationally expensive than the aforementioned narrow-band models but also less accurate.

More recently, full-spectrum models have been developed including the spectral line-weighted sum-of-gray-gases (SLW) [99, 100, 101, 102, 103], cumulative wavenumber (CW) [104, 105, 101], and full-spectrum k-distribution (FSK) [106, 107, 108, 109, 110, 111, 112, 113, 114, 115] methods. It has been shown that the SLW method is a simplified version of the full-spectrum k-distribution method [116]. We focus on the full-spectrum k-distribution method.

## THE FULL SPECTRUM K-DISTRIBUTION METHOD

The k-distribution method represents an alternative to line-by-line calculations which reduces the number of RTE evaluations from the order of a million to the order of ten without any significant loss of accuracy for homogeneous media [117]. This requires the formulation of a weighted cumulative distribution function of the absorption coefficient where the weight function is the Planck distribution.

$$g(\kappa) = \frac{\pi}{\sigma T^4} \int_{\eta \text{ s.t. } \kappa_\eta \leq \kappa} I_{b,\eta} d\eta \quad (4.5)$$

Figure 4.1 demonstrates graphically the regions over which the Planck distribution would be integrated in order to compute  $g$  for a particular value of the absorption coefficient,  $\kappa$  (or equivalently, the absorption cross section,  $C$ ) for a narrow section of a representative spectrum. The Planck distribution is a function of the reference temperature. The spectral absorption coefficient,  $\kappa_\eta$ , is a function of the local state (temperature, pressure, and concentration).

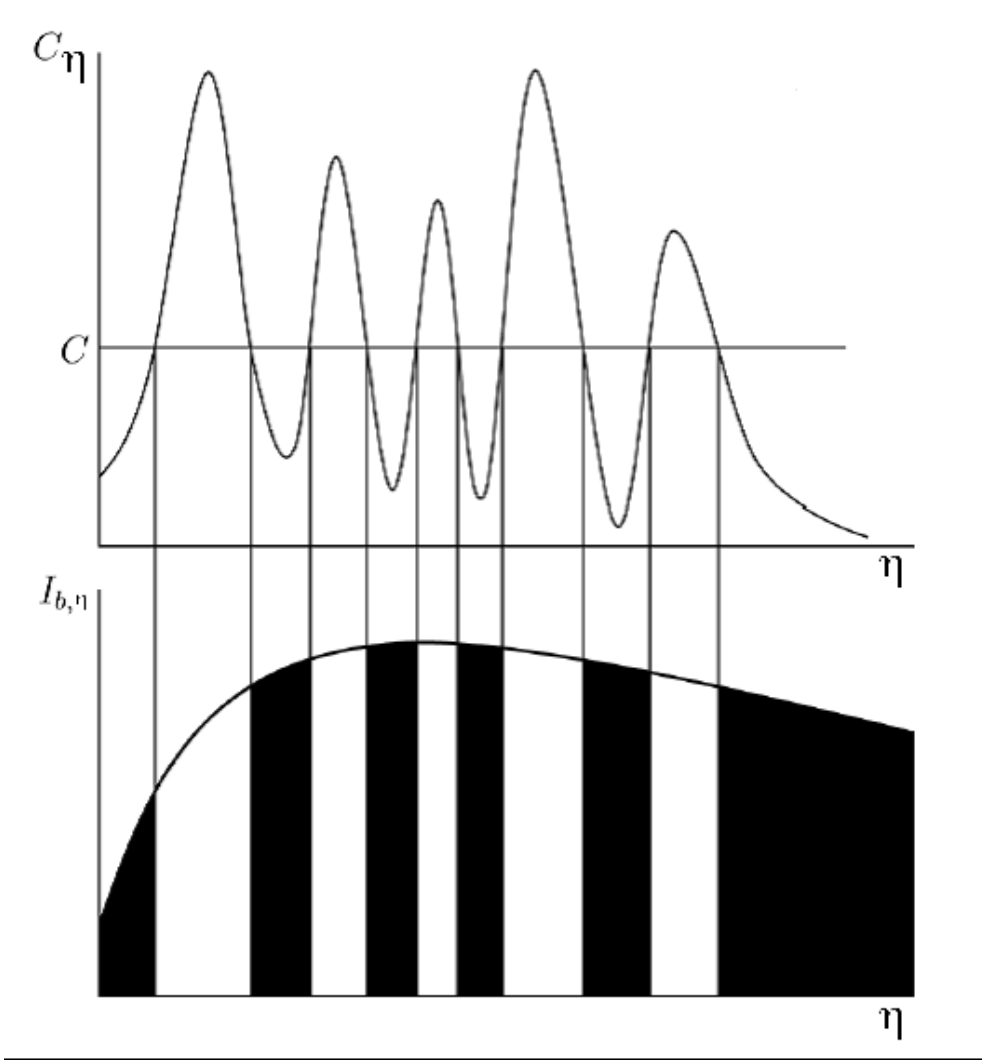


Figure 4.1: Demonstration spectral integration domain for generating k-distributions [113]

$C$  is directly proportional to  $\kappa$ . The constant of proportionality is the number density,  $N$ . Assuming ideal gas behavior for a single absorbing species, this relationship is expressed in Equation (4.6).

$$\kappa = C \cdot N \approx C \cdot \frac{P}{RT} \quad (4.6)$$

where  $P$  is the partial pressure of the absorbing species,  $T$  is the temperature and  $R$  is the universal gas constant expressed in consistent units. Intuitively,  $g$  represents the fraction of energy present in all wavelength intervals for which the absorption coefficient is less than or equal to a given value.

The implicit assumption in equation (4.5) is that the spectral dependence of energy within the system is based only upon the local optical properties and the Planck distribution at a particular reference temperature. This allows for the optical properties to be weighted in a consistent way throughout the medium. For homogeneous systems, this is true. For inhomogeneous systems, this assumption breaks down. For systems with large temperature or concentration gradients, the temperature and concentration dependence of the spectral properties produce large errors. The fundamental problem to be addressed is the difficulty in quantifying these errors for the purposes of predictive simulation.

The cumulative distribution function,  $g$  is a smooth monotonically increasing function of the absorption coefficient,  $\kappa$ . In fact,  $g$  is bijective. This is by construction since despite its rapid oscillations, the spectral absorption coefficient is a continuous function of wavelength. In fact, since Lorentz profiles are assumed, the spectral absorption coefficient is even differentiable. Voigt profiles are also differentiable. The problem with using it to solve radiative transport problems directly is that the highly oscillatory nature of the distribution requires a prohibitively large number of spectral intervals in order to accurately resolve the properties. In essence, what the k-distribution method does is take advantage of the fact that a given absorption coefficient is simultaneously achieved in many disjoint spectral intervals resulting in redundant RTE solves. The k-distribution method identifies and removes this redundancy.

Figure 4.2 shows an example of a k-distribution generated for CO<sub>2</sub> at 600K and 1atm. Since  $g(\kappa)$  is a bijection, it is invertible and a unique function  $\kappa_g$  or  $C_g$  may be defined.

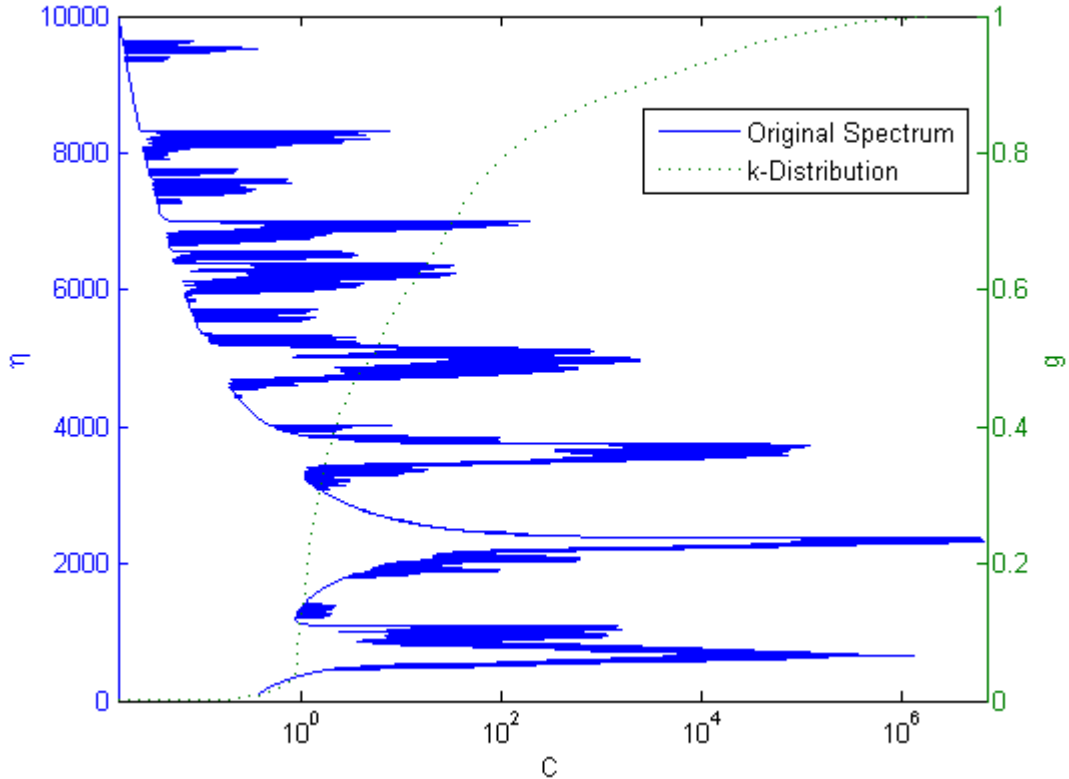


Figure 4.2: Example k-distribution for CO<sub>2</sub> at 600K, 1 atm

We can then rewrite the radiative transport equation as a function of  $g$  rather than  $\eta$ . The  $g$  subscript denotes that the quantity is a function of  $g$  rather than of wavenumber. As a further simplification, we neglect scattering. The full-spectrum k-distribution may be extended to cases with scattering [107, 108, 106] but the scattering term is omitted in this development.

$$\frac{dI_g}{dS} = \kappa_g (I_b - I_g) \quad (4.7)$$

Additionally, we can evaluate the total intensity by integrating over  $g$  rather than  $\eta$ . By using this change of variables, the integration required to obtain the total intensity is simplified.

$$I = \int_0^1 I_g dg \quad (4.8)$$

As can be seen from Figure 4.2,  $\kappa_g$  is a smoothly varying function of  $g$  and consequently,  $I_g$  is a smoothly varying function of  $g$  as well. This allows for a much smaller number of quadrature points to achieve near-line-by-line accuracy. The integration over  $g$  may be accomplished using any available quadrature rule. An 8 point Gaussian quadrature is found to provide good results in most cases although increased accuracy may be achieved by using higher order quadrature schemes.

For each value of  $g$  we find the intensity by solving the RTE for a (potentially inhomogeneous) gray gas. This solution may be found by any of the methods discussed in Chapter 3 or other methods not discussed. The methods range from highly accurate but computationally expensive to extremely fast with only first order accuracy. Which solution method is appropriate may be determined based upon the optical thickness for a given value of  $g$ .

There is an inherent problem with the method just described when analyzing non-isothermal media. The Planck distribution in Equation (4.5) is not only a function of wavenumber, but of temperature as well. Choosing the appropriate temperature for use in defining the k-distribution function a priori is difficult for non-isothermal problems. For cases where temperature variations across the domain are relatively small, this

temperature dependence is negligible and the full spectrum k-distribution method provides good results for any reasonable choice of reference temperature including but not limited to the maximum temperature in the system, the volume averaged temperature, the Planck mean temperature, and the emission weighted temperature [116].

As the temperature variations become large, significant errors can develop as a result of this approximation [114]. One way to solve this temperature dependence problem is to model the absorption coefficient's dependence on the temperature as was done in the Multi-Group Full Spectrum k-Distribution Method (MGFSK) [118].

The MGFSK method provides good results for inhomogeneous media and the accuracy may be increased by the inclusion of an increasing number of groups. However, the method remains approximate and can result in significant errors if an insufficient number of groups is used. As the number of groups included increases, the MGFSK solution approaches the line-by-line solution in both accuracy and computational cost.

A drawback inherent to all of the methods for approximating the spectral intensity is that the assumptions made in their development are not always valid. In fact, these assumptions are most often invalid for inhomogeneous media problems. For the k-distribution method and its extensions, there are two underlying assumptions which are commonly invalid for inhomogeneous media problems. The first assumption is that the spectral energy density within the medium is approximated well by a Planck distribution at a chosen reference temperature. The second assumption is that the spectrum is correlated. This assumption is commonly referred to as the so-called scaling approximation.

$$C(\eta, s) = C(\eta) \cdot u(s) \quad (4.9)$$

This assumption is perfectly valid for many applications [119, 112, 111]. The issue that arises when applying the k-distribution method to problems with inhomogeneous media is that this assumption is not a good one in the presence of strong temperature or concentration gradients [119, 120, 121]. One of the main drawbacks to the method is that not only can these errors become large, but there is currently no established technique for assessing the validity of equation (4.9) quantitatively. In practice this means that the method is either not used, used blindly, or that expert intuition is required to qualify the reliability of the results.

A robust method in keeping with the general requirements of uncertainty quantification is highly desirable. While other researchers have found various ways to reduce these errors [114, 118], there has previously been very little published regarding the estimation of these errors for the purposes of uncertainty quantification.

One option for evaluating the errors introduced by the k-distribution method is to eliminate them and replace them with errors which are easier to quantify. This is the approach taken in the Multi-Source Full Spectrum k-Distribution (MSFSK) Method [122]. The MSFSK method is capable of providing exact results for one dimensional geometries with piecewise constant temperature and absorption coefficient in the same way that the full spectrum k-distribution method is able to provide exact results for homogeneous media. The errors introduced by approximating a continuous temperature or property distribution as piecewise constant are well understood and easily estimated.

## THE MULTI-SOURCE FULL SPECTRUM K-DISTRIBUTION METHOD

For treatment of non-isothermal media, various approximations must be made. It is not feasible to provide a continuous definition of the medium's spectral properties as a function of temperature. As a substitute, the continuous temperature distribution within

the slab is modeled as piecewise constant in what has been called a multilayer approach. Solovjov and Webb applied this method to the SLW and CW methods in 2008 and demonstrated that a relatively small number of layers is actually required in order to achieve good predictions of the radiative heat flux and flux divergence [101].

The non-isothermal slab is divided into  $K$  layers. Each layer has a temperature,  $T_k$ , a spectral absorption coefficient,  $\kappa_\eta^k$  and a width,  $\Delta x_k = x_k - x_{k-1}$ . Within each layer, the total integrated heat flux and flux divergence are sought. The multi-layer approximation is similarly applicable to inhomogeneous media with concentration gradients. If concentration gradients exist, layers should be sufficiently thin so that the spectral absorption coefficient may be modeled as constant within each layer. By treating the temperature distribution as piecewise constant, spatial discontinuities in the source function are introduced. These result in corresponding discontinuities in the radiative flux divergence.

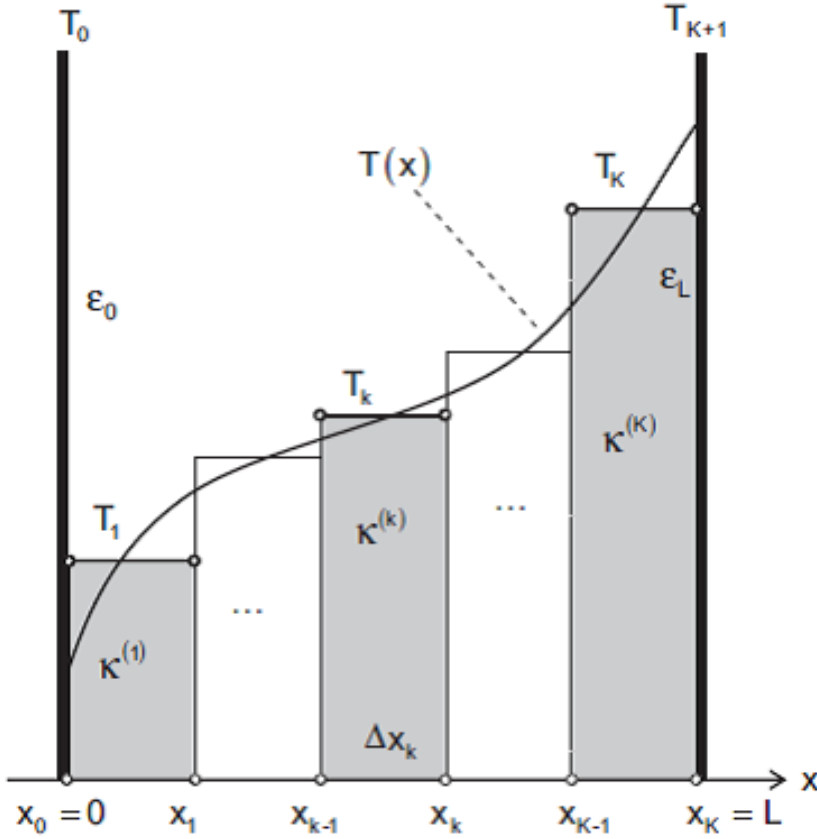


Figure 4.3: Schematic illustration of multilayer system and geometric nomenclature [101]

For isotropic scattering and diffuse boundary conditions, the directionally integrated spectral heat flux is only a function of optical depth and is given by equation (4.10). As previously stated, optical depth is the non-dimensional spatial coordinate.

$$q_{r,\eta}(\tau_\eta) = 2\pi \left\{ I_\eta^+(0)E_3(\tau_\eta) - I_\eta^-(\tau_{L\eta})E_3(\tau_{L\eta} - \tau_\eta) + \cdots + \int_0^{\tau_\eta} \hat{I}_\eta(\tilde{\tau}_\eta)E_2(\tau_\eta - \tilde{\tau}_\eta)d\tilde{\tau}_\eta - \int_{\tau_\lambda}^{\tau_{L\eta}} \hat{I}_\eta(\tilde{\tau}_\eta)E_2(\tilde{\tau}_\eta - \tau_\eta)d\tilde{\tau}_\eta \right\} \quad (4.10)$$

Neglecting scattering, the source function is simply the black-body intensity and is piecewise constant. Inserting the definition of optical depth and simplifying the integrals yields the spectral heat flux as a function of position.

$$q_{r,\eta}(x) = 2\pi \left\{ \begin{array}{l} I_\eta^+(0)E_3(\tau_\eta(x)) - I_\eta^-(L)E_3(\tau_\eta(L) - \tau_\eta(x)) + \dots \\ + \sum_{i=1}^{k-1} I_{b,\eta}(T_i) [E_3(\tau_\eta(x) - \tau_\eta(x_i)) - E_3(\tau_\eta(x) - \tau_\eta(x_{i-1}))] + \dots \\ + \sum_{i=k+1}^K I_{b,\eta}(T_i) [E_3(\tau_\eta(x_i) - \tau_\eta(x)) - E_3(\tau_\eta(x_{i-1}) - \tau_\eta(x))] + \dots \\ + I_{b,\eta}(T_k) \cdot [E_3(\kappa_\eta^k(x - x_{k-1})) - E_3(\kappa_\eta^k(x_k - x))] \end{array} \right\} \quad (4.11)$$

Using the multilayer approach, the definition of the optical depth may be simplified.

$$\tau_\eta(x) = \int_0^x \kappa_\eta(\tilde{x}) d\tilde{x} = \sum_{i=1}^{k-1} \kappa_\eta^i \Delta x_i + \kappa_\eta^k (x - x_{k-1}) \quad (4.12)$$

The k-distribution method may be applied within each layer in order to reduce the number of spectral evaluations required. In order to do this, a reasonable reference temperature should be established. It has been shown [123] that in general non-isothermal problems this is not always feasible and that errors associated with this choice are difficult if not impossible to quantify.

The form of equation (4.11) suggests an alternative to the establishment of a global reference temperature. The problem may be recast as 3K sub-problems, K of which includes emission from exactly one layer at exactly one temperature. The other 2K sub-problems involve purely absorbing media with a (complex) spectral boundary condition. The spectral heat flux at the layer boundaries is found by performing a line-

by-line solution on a significantly coarser spatial grid with only K points. There is no additional assumption introduced here besides the multilayer approximation. The radiative transport equation is linear within each layer and we are representing the solution as a superposition of solutions to simpler problems.

For ease of explanation, we will discuss the contributions to the spectral heat flux at layer boundaries as being due to contributions from each individual layer. The total spectral heat flux is found by summing the contributions from each of the individual layers. In the one-dimensional problem, these contributions may be written explicitly.

The contribution to the spectral heat flux due to emission from the k<sup>th</sup> layer is given by equation (4.13).

$$q_{r,\eta}^k(x) = 2\pi I_{b,\eta}(T_k) \begin{cases} E_3(\tau_\eta(x) - \tau_\eta(x_k)) - E_3(\tau_\eta(x) - \tau_\eta(x_{k-1})) & x_k \leq x \\ E_3(\tau_\eta(x_k) - \tau_\eta(x)) - E_3(\tau_\eta(x_{k-1}) - \tau_\eta(x)) & x \leq x_{k-1} \\ E_3(\kappa_\eta^k(x - x_{k-1})) - E_3(\kappa_\eta^k(x_k - x)) & x \in (x_{k-1}, x_k) \end{cases} \quad (4.13)$$

In order to use the k-distribution method to simplify the numerical spectral integration, an appropriate weighting function for the generation of the absorption line blackbody distribution function (ALBDF) must be defined. Usually, a Planck distribution at a set reference temperature is used as this weighting function. However, the method may be generalized by using a general weighting function which can be defined for each problem.

$$g(\kappa) = \frac{\int_{\eta \text{ s.t. } \kappa_\eta^k < \kappa} w(\eta) d\eta}{\int_{\eta=0}^{\infty} w(\eta) d\eta} \quad (4.14)$$

The  $w(\lambda)$  is a weighting function that may be different for each sub-problem. Consider the K sub-problems representing the flux within a given layer due to emission from within that same layer. For the  $k^{\text{th}}$  sub-problem of this type, the weighting function is simply the Planck distribution at the layer temperature and is given by equation (4.15).

$$w(\eta) = I_{b,\eta}(T_k) \quad (4.15)$$

A database of k-distribution functions using these weighting functions has previously been developed by Modest for CO<sub>2</sub> and H<sub>2</sub>O [117]. The distributions in this database are derived using a different spectroscopic reference than the HITRAN database used here [82]. However, the two databases yield similar results and after the simplification of applying the k-distribution method, the distributions are interchangeable. More recently, a database of k-distribution weighting functions has been updated using the HITEMP 2010 spectral database [115]. There is no geometry information imbedded in equation (4.15) so these functions may be evaluated and inverted offline.

There are an additional K sub-problems representing the heat flux within a given layer due to emission from layers to the left of that layer. For these sub-problems the appropriate weighting function is given by equation (4.16). Note that the weighting functions presented here only equal the spectral heat flux up to a multiplicative constant since any such constant is eliminated in the normalization of  $g$  performed in equation (4.14).

$$w(\eta) = \sum_{l=1}^{k-1} \kappa'_\eta I_{b,\eta}(T_l) \left\{ E_3 [\tau_\eta(x_k) - \tau_\eta(x_l)] - E_3 [\tau_\eta(x_k) - \tau_\eta(x_{l-1})] \right\} \quad (4.16)$$

The remaining K sub-problems represent the heat flux within a given layer due to emission from layers to the right of that layer. The appropriate weighting function in these sub-problems is given by equation (4.17).

$$w(\eta) = \sum_{l=k+1}^K \kappa'_\eta I_{b,\eta}(T_l) \left\{ E_3 [\tau_\eta(x_{k-1}) - \tau_\eta(x_l)] - E_3 [\tau_\eta(x_{k-1}) - \tau_\eta(x_{l-1})] \right\} \quad (4.17)$$

The k-distribution method has the advantage that any standard quadrature rule may be employed to evaluate the spectral integral which has been transformed into an integral over  $g$ . While it is possible to vary the quadrature rule used at different spatial points within the slab, it is generally not very practical to do so. From this point forward, our notation will assume that the same N-point quadrature rule is used at every spatial point.

Within each layer, equation (4.14) is inverted to define a unique function  $\kappa_g$  which is constant within that layer in the same manner as  $\kappa_\eta^k$  and  $T_k$ . The modified wavenumber,  $g$  is in  $[0,1]$  and the choice of quadrature rule defines a set of N transport equations that should be solved within each layer. Any appropriate solution technique may be used to determine the solution within each sub-problem. The solution method may be chosen on the basis of layer optical thickness.

Summing the solutions for the total heat flux or flux divergence from the 3K sub-problems yields an accurate solution to the inhomogeneous problem on a very fine spatial grid. Each of the sub-problems is solved using the k-distribution method with the appropriate weighting function. Because each of the sub-problems consists of either a homogeneous media surrounded by cold black walls or a purely non-emitting media

subject to a spectral boundary condition, the k-distribution method is capable of reproducing line-by-line results exactly.

The significant cost savings provided by this method relative to a full line-by-line solution stems from the significant computational savings and efficiency gained by the use of the k-distribution method. This decrease in cost comes at virtually no cost in accuracy besides that incurred due to the use of the multilayer approximation.

### **Computational Cost of the MSFSK Method**

We will compare the computational cost of the multi-source k-distribution method with the cost of a line-by-line solution and with a standard k-distribution method. The line-by-line solution requires  $N_{lbl}$  solutions of the gray radiative transport equation at  $M$  spatial locations. The cost of a single gray RTE solution scales as  $M^\alpha$  where  $\alpha \in [2,3]$  depends upon the RTE solution technique as well as the linear algebra package employed. The case where  $\alpha = 2$  corresponds to the evaluation of the analytical solution expressed in equation (4.10).  $\alpha = 3$  corresponds to the solution of a general dense matrix. The cost of a line-by-line solution is therefore given by equation (4.18).

$$N_{lbl}M^\alpha \quad (4.18)$$

By contrast, the cost of a solution by the standard k-distribution method is given by equation (4.19). The only difference from equation (4.18) is the number of times the chosen RTE solver must be called in order to generate the solution. The solution time scales linearly with this parameter.

$$N_{kdist}M^\alpha \quad (4.19)$$

Here,  $N_{kdist} \ll N_{lbl}$  is the number of quadrature points used in the k-distribution spectral integration. The number of RTE evaluations involved in the k-distribution method is always considerably less than the number involved in a line-by-line solution. This commonly represents up to 5 or 6 orders of magnitude improvement in computational cost over the line-by-line method. However, for non-isothermal media, this improvement comes at a cost in accuracy which can be large in some cases and has yet to be effectively bounded in general.

The cost of the multi-source k-distribution method is between the two and is given by equation (4.20) where  $K$  is the number of layers used in the multilayer approximation.

$$N_{lbl}K^\alpha + 3N_{kdist}K\left(\frac{M}{K}\right)^\alpha \quad (4.20)$$

For simplicity, it is assumed that the number of spatial points per layer is uniform. For this method to be viable,  $K \ll M$ . Ideal applications for this method are those requiring a high order of accuracy on a fine spatial grid.

## MSFSK Results and Discussion

Solovjov and Webb established the convergence and viability of the multilayer approach in their paper [101]. This establishes the legitimacy of approximating a slab with a continuous temperature distribution as having a piecewise constant temperature distribution as depicted graphically in Figure 4.3. The question remains how well the k-distribution method and the multi-source k-distribution method predict the radiative heat flux and flux divergence in slab geometries with piecewise constant temperature distributions.

As a limiting case, consider a large step change in temperature. The left half of the slab (50 cm) is at 1000 K. The right half is at 300 K. The medium is 10% CO<sub>2</sub> by mole and is at a uniform pressure of 1 atm. The CO<sub>2</sub> is mixed with a gas that is assumed to be nonparticipating. Spectral line data (centers, half-widths, and intensities) are acquired from the HITRAN 2004 database [82]. The line data is used to generate a high resolution absorption spectrum. Lorentz profiles are used for all line shapes. The same spectrum is used in both the line-by-line solution and in the generation of the k-distribution functions.

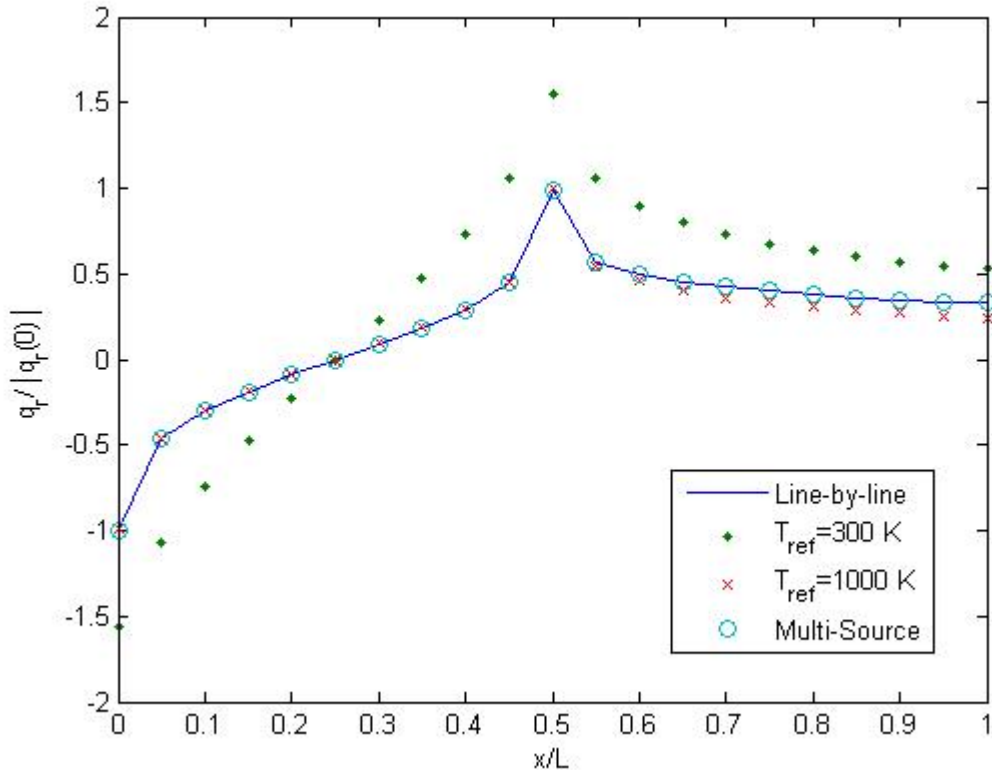


Figure 4.4: Heat flux distribution in a non-isothermal medium bounded by cold black walls; Comparison of MSFSK results to line-by-line and k-distribution results

Figure 4.4 shows the calculated heat flux using the full spectrum k-distribution method with a single reference temperature and using the multi-source k-distribution method. These results are compared to those generated using line-by-line calculations. Using a reference temperature of 300 K gives poor results. The majority of the radiative energy is emitted in the hotter left half of the slab. Using a reference temperature of 300 K is totally incorrect for this spatial region. For this reason, the heat flux is poorly represented in every part of the domain.

Using a reference temperature of 1000 K, the heat flux prediction is quite accurate in the left half of the domain ( $x/L < 1/2$ ). Relative errors are higher in the right half of the domain ( $x/L > 1/2$ ). The fact that this model does a relatively poor job of predicting the behavior of energy emitted from the right half of the medium has little effect since the vast majority of the flux is due to the high temperature emission from the left half of the slab. However, this model also does a poor job of predicting the absorption of energy in the right half of the slab. This leads to potentially large relative errors in predicting the heat flux exiting the right boundary. The thicker the cold region becomes, the more significant this error becomes.

Modest and Zhang analyzed the effect of the length of the cold region on the error in the heat flux at the right wall for several different reference temperature models [116]. They used a higher temperature for the hot zone and a slightly different gas mixture for their test case. However, the general trends should hold true. Five different reference temperatures were used in this study and none were capable of achieving the kind of accuracy reported here using the Multi-Source method. Admittedly, this improvement in accuracy comes at a computational cost. However, for applications for which accuracy is paramount, the multilayer multi-source k-distribution method provides a more efficient alternative to line-by-line calculations. It should also be noted that the MSFSK method is

ideally suited for problems where the actual temperature distribution is piecewise constant. This eliminates the major source of error in the MSFSK method.

This example highlights the difficulty of using the k-distribution method in non-isothermal media. The appropriate choice for a reference temperature is virtually impossible to determine a priori. Furthermore, the error associated with an incorrect choice of reference temperature is unknown. The correct value of the heat flux at any given spatial location is not guaranteed to be bounded by the heat flux calculated using the maximum system temperature as the reference temperature and the heat flux calculated using the minimum system temperature as the reference temperature. As can be seen from Figure 4.4, this error can be substantial.

In contrast, the error introduced by the multilayer approximation has a well-known and easily quantifiable behavior [124, 125]. To demonstrate this fact, consider a slab at a uniform pressure of 1 atm. The only participating species present is CO<sub>2</sub> which has a molar concentration of 10%. The slab is 1m thick and subject to a linear temperature profile.

$$T(x) = 300 + 950x \quad (4.21)$$

The wide range of temperatures presents a challenge for the traditional k-distribution method and it is difficult if not impossible to determine a priori if the k-distribution method will provide reliable results for this problem. As it turns out, the traditional k-distribution method is capable of providing moderate accuracy for this problem when using an optimal global reference temperature. However, this optimal reference temperature is not generally known without comparison to line-by-line results making the method unreliable for general applications.

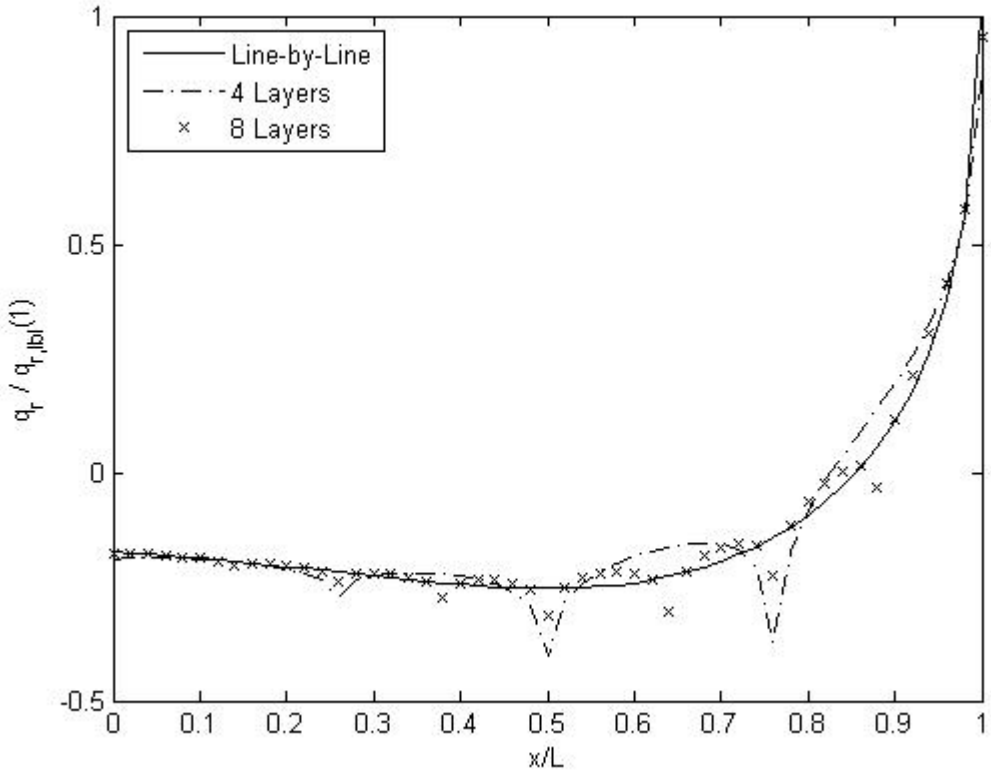


Figure 4.5: Heat flux distribution in a medium with linear temperature profile bounded by cold black walls; comparison of MSFSK and line-by-line results for CO<sub>2</sub> with a molar concentration of 10%

Figure 4.5 shows the accuracy and convergence of the multilayer approximation in a problem with a continuously varying temperature profile and temperature-dependent spectral properties. The line-by-line results for the piecewise constant cases with 4 and 8 layers are not shown since they are indistinguishable from the MSFSK results. The continuous curve labeled ‘Line-by-Line’ in the figure represents the direct line-by-line solution on the fine grid. For these cases, it should be considered the exact solution to the radiative transport equation including temperature-dependent spectral properties.

Consider an additional example with a quadratic temperature profile. Once again large temperature gradients are present making the blind application of the k-distribution method a dubious choice for high-accuracy applications.

$$T(x) = 1000 - 2000 \left( x - \frac{L}{2} \right)^2 \quad (4.22)$$

As a result of symmetry considerations, an odd number of layers is used in this example. There is nothing preventing the use of an even number of layers. The convergence behavior and error estimations properties remain unchanged.

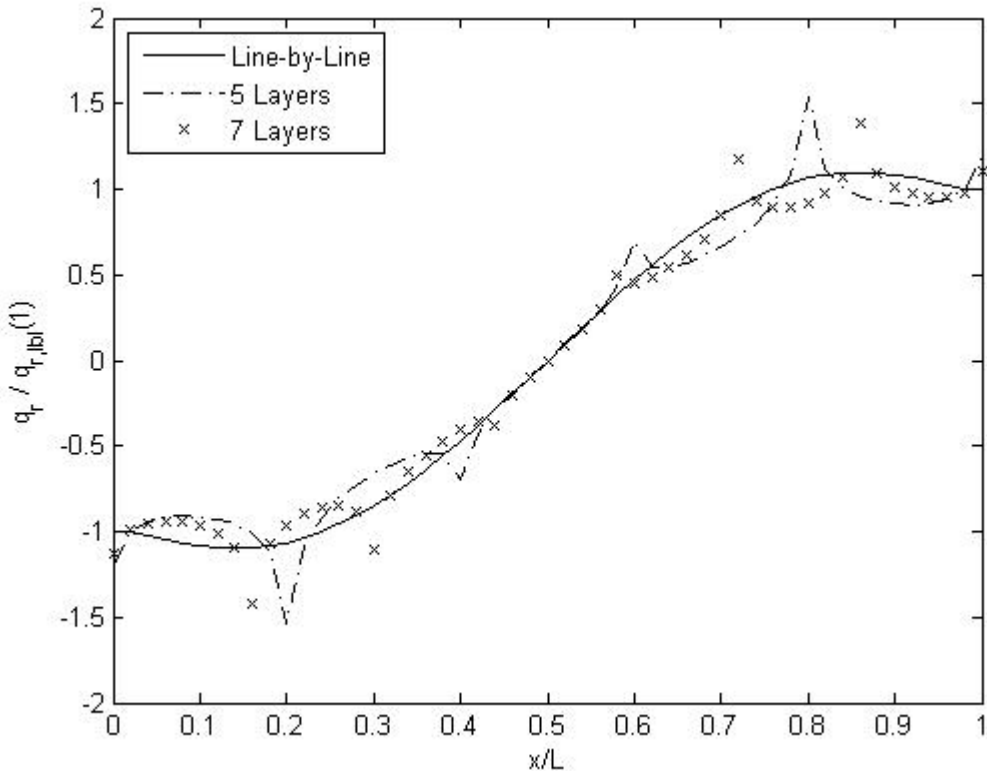


Figure 4.6: Heat flux distribution in a medium with quadratic temperature profile bounded by cold black walls; comparison of MSFSK and line-by-line results for CO<sub>2</sub> with a molar concentration of 10%

Figure 4.6 shows the results for this third example problem. Once again, the only error introduced is that of the multilayer approximation. This is by design. The difficulty of quantifying the error of the k-distribution method in inhomogeneous media is circumvented by approximating any problem as a superposition of sub-problems, each of which is homogeneous. The error introduced by approximating a general problem this way is readily understood and converges predictably as the number of layers increases.

The disadvantage of this approach is the oscillatory nature of the MSFSK solutions. This is readily apparent in Figures 4.5 and 4.6. This is a result of approximating the temperature distribution as piecewise constant. For a monotonic

temperature profile this results in an under prediction of the emission in one part of the layer and an over prediction in another. These oscillations could be eliminated by only approximating the optical properties as piecewise constant as opposed to the entire state vector. However, while potentially appealing for some applications this approach would likely result in a less rigorous error analysis.

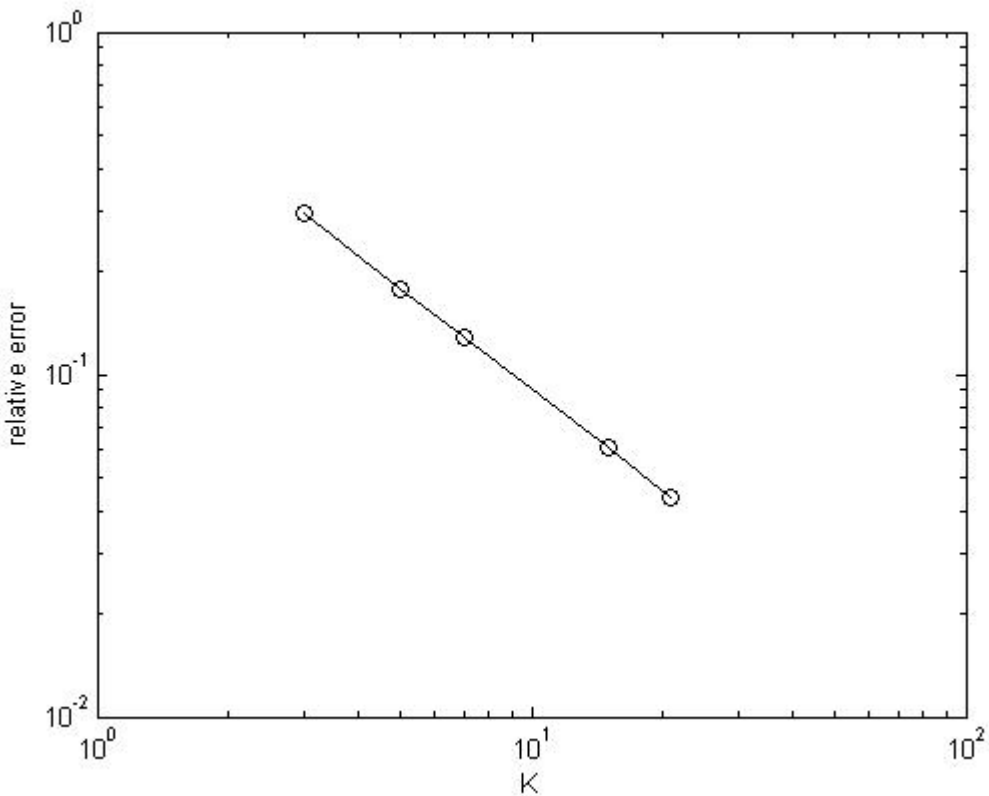


Figure 4.7: Convergence in relative error for the multilayer approximation for quadratic temperature profile example problem;  $L^2$  error of MSFSK heat flux prediction relative to line-by-line prediction for  $\text{CO}_2$  with a molar concentration of 10%

Figure 4.7 shows the convergence rate of the multilayer approximation for a quadratic temperature profile. The relative error in the spatially varying heat flux is calculated using the usual  $L^2$  norm. The consistent and known rate of convergence

allows for the use of a wide array of numerical tricks for estimating the error and improving successive approximations. This behavior has been previously observed and reported for gray gas cases [124].

Another common test case involves finding the steady-state temperature distribution for a system rather than the flux or flux divergence for a system with a known temperature distribution. The multi-source full spectrum k-distribution may be applied to problems of this type as well. Consider a slab of gas that is 10% CO<sub>2</sub> by mole. CO<sub>2</sub> is the only participating species and scattering is negligible. The slab is bounded by back walls whose temperatures are held fixed. The left wall is 1000K and the right wall is 500K. The temperature dependence of the spectral properties is included in the calculation. The temperature distribution corresponding to radiative equilibrium is sought.

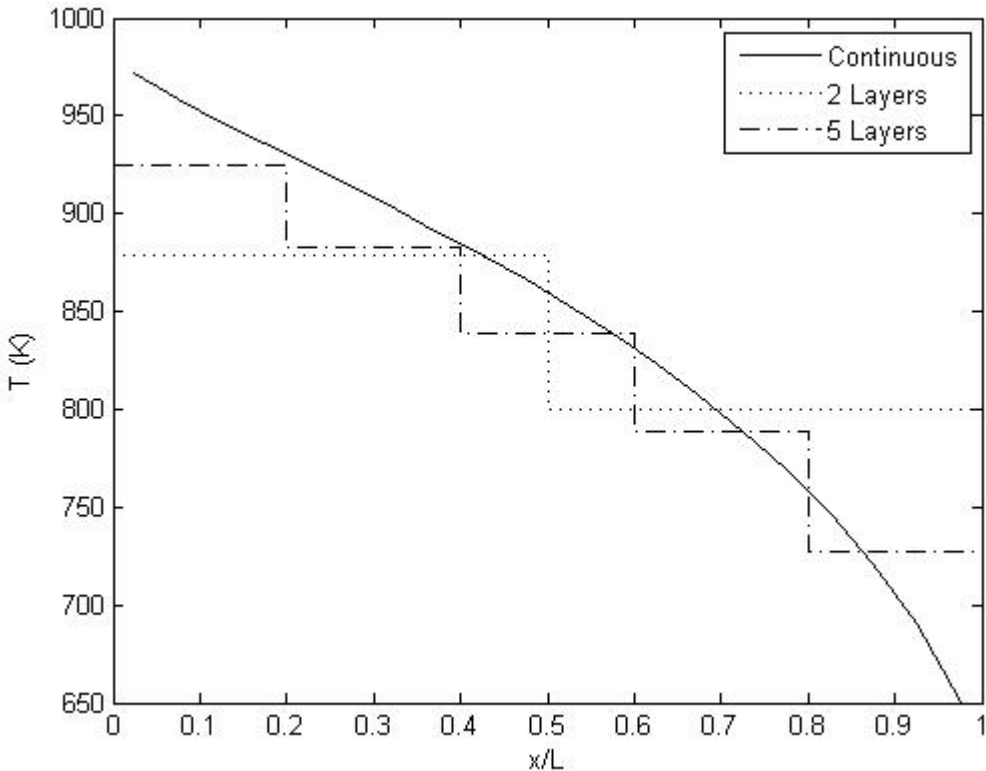


Figure 4.8: Steady-state temperature profiles for a slab with fixed temperature boundary conditions using line-by-line and MSFSK methods

Figure 4.8 contrasts the actual temperature profile calculated using a line-by-line approach with approximate temperature profiles generated by the MSFSK method. It is interesting to note that this is not the same temperature profile one would find by defining two or five homogeneous control volumes and conserving energy over them. The steady-state MSFSK profiles are also not approximations of the continuous curve although they approach that curve in the limit as  $K \rightarrow \infty$ . In the MSFSK method, radiative equilibrium cannot be reached due to the piecewise constant constraint on the temperature profile. Radiative equilibrium is defined as a state where the radiative flux divergence is identically zero everywhere in the domain. Instead, the  $L^2$ -norm of the calculated flux-

divergence on a fine spatial grid is minimized with respect to the temperature values for the K layers.

This approach is not ideal for pure radiation problems. The MSFSK method is intended for use in combined-mode problems for which the fine spatial grid required to accurately evaluate convection phenomena is over-kill for the radiation problem. The resulting method allows for the accurate inclusion of spectral radiative properties while only introducing well-understood discretization errors rather than unknown and unbounded errors resulting from one of many non-gray RTE solution techniques. In this way, non-gray radiation may be included in large-scale combined-mode problems with the confidence of knowing the approximation errors introduced.

The multilayer approach as presented above provides a significant increase in accuracy when compared to other k-distribution based approaches while remaining significantly less computationally expensive than a standard line-by-line solution. Unfortunately, it is not readily applicable to general higher dimensional geometries. Furthermore, the weighting functions used are not problem-independent and must be generated for each geometry decreasing run-time performance. The errors introduced by this method are entirely due to the multilayer approximation. As a result, the method converges linearly as the number of layers increases. This allows the error relative to the line-by-line solution to be estimated. This ability to estimate the error in evaluating the spectral integral is both unique and desirable. However, due to the drawbacks associated with the MSFSK method, another technique is developed. This technique is both applicable to higher-dimensional geometries and completely independent of the problem being studied. It does not however provide increased accuracy relative to a traditional full-spectrum k-distribution method.

## THE STOCHASTIC FULL SPECTRUM K-DISTRIBUTION METHOD

The full spectrum k-distribution is defined as

$$f(T_p, \vec{\phi}; C) = \frac{1}{I_b} \int_0^\infty I_{b\eta}(T_p) \delta(C - C_\eta(\vec{\phi})) d\eta \quad (4.23)$$

The temperature,  $T_p$  is a representative temperature for the Planck function being used as a weighting factor. The state vector,  $\vec{\phi}$  can include components such as the gas temperature (or temperatures in non-LTE systems), absolute pressure, and species concentrations. The function,  $f$  depends upon  $\vec{\phi}$  implicitly through the spectral absorption cross-section,  $C_\eta$ . In practice, the cumulative distribution function corresponding to the full-spectrum correlated k-distribution is more useful.

$$g(T_p, \vec{\phi}; C) = \int_0^C f(T_p, \vec{\phi}; \tilde{C}) d\tilde{C} = \frac{1}{I_b} \int_0^\infty I_{b\eta}(T_p) H(C - C_\eta(\vec{\phi})) d\eta \quad (4.24)$$

There have been several databases developed in order to rapidly evaluate these functions [109]. This transformation from wavenumber space into fractional Planck distribution space involves the effective reordering of the spectral absorption cross-section. This is done independently for each value of the state vector,  $\vec{\phi}$ . The assumption that underlies this process is the so-called scaling approximation. The application of the scaling approximation assumes that despite performing this reordering independently for each value of the state vector that the reordering is consistent throughout the entire spatial domain.

Previous efforts to define the model-form uncertainty associated with the correlated k-distribution method [123, 124] focused on approximating the problem domain so as to eliminate the k-distribution model error and replace it with a more

readily quantified discretization error. The Multi-Source Full Spectrum k-Distribution Method just described is an example of this approach. This technique is currently restricted to 1-D applications and is deemed inadequate for general uncertainty quantification applications at this time. We seek to develop a method for establishing the confidence with which we may rely upon results generated by the k-distribution method in general inhomogeneous media. This requires a deeper understanding of what causes the errors in the k-distribution method.

It is common practice to utilize a correlation assumption between the distribution functions at different gas and Planck temperatures. These empirical correlations represent a way of interpolating between distribution functions generated from high resolution spectral data at a finite combination of gas states and Planck temperatures. Similar interpolation of the additional stochastic parameters suggested here is necessary for solving general problems in a computationally efficient manner. We will not focus on the generation of these correlations but rather on introducing a new parameter derived directly from the high resolution spectral data for quantifying the uncertainty associated with the full-spectrum cumulative k-distribution method.

It is first instructive to break the process of developing the full-spectrum correlated k-distribution function embodied by Equation (4.24) into two parts. The first step is a reordering in wavenumber space so that the absorption coefficient is monotonically increasing. This amounts to a transformation from wavenumber space,  $\eta$  into modified wavenumber space,  $\eta^*$ . The modified wavenumber represents the portion of the spectrum for which the absorption coefficient is less than a particular value. The transformation from wavenumber space to modified wavenumber space constitutes the reordering of the absorption coefficient spectrum. The full-spectrum correlated k-distribution method effectively generates a unique transformation for each value of the

state vector. The scaling approximation assumes that each of the unique transformations is equivalent thereby neglecting any errors introduced. In practice these transformations are not equivalent. This is the major source of error in the correlated k-distribution method. The SFSK method recognizes that these transformations vary with respect to the state vector and quantifies the error introduced by the gradual failure of the scaling approximation.

$$\int_{\{\eta: C_\eta < C\}} f(\eta) d\eta = \int_0^{\eta_C^*} f(\eta^*) d\eta^* \quad \forall f$$

$$\eta_C^* = \int_{\{\eta: C_\eta < C\}} d\eta$$
(4.25)

This transformation is bijective, but not necessarily unique. The choice of transformation does not effect  $C(\eta^*)$  and is a result of the sorting algorithm used. This intermediate variable,  $\eta^*$  is not useful in any computation and only serves to demonstrate the independence of the spectral reordering and the spectral weighting.

The original spectrum is shown in Figure 4.9.

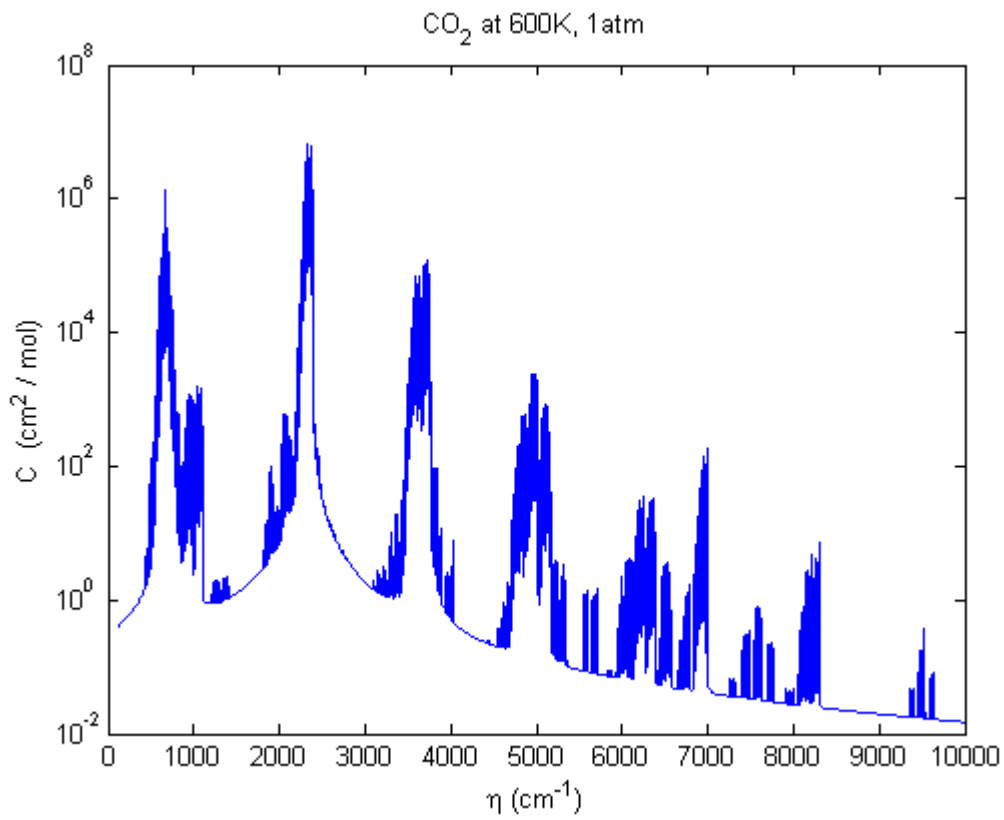


Figure 4.9: Example of CO<sub>2</sub> spectrum in normal wavenumber space

The wavenumbers are reordered in such a way that the absorption cross-section is a monotonically increasing function of the reordered wavenumber,  $\eta^*$ . This property defines the modified wavenumber  $\eta^*$ . The result for the sample spectrum from Figure 4.9 is shown in Figure 4.10.

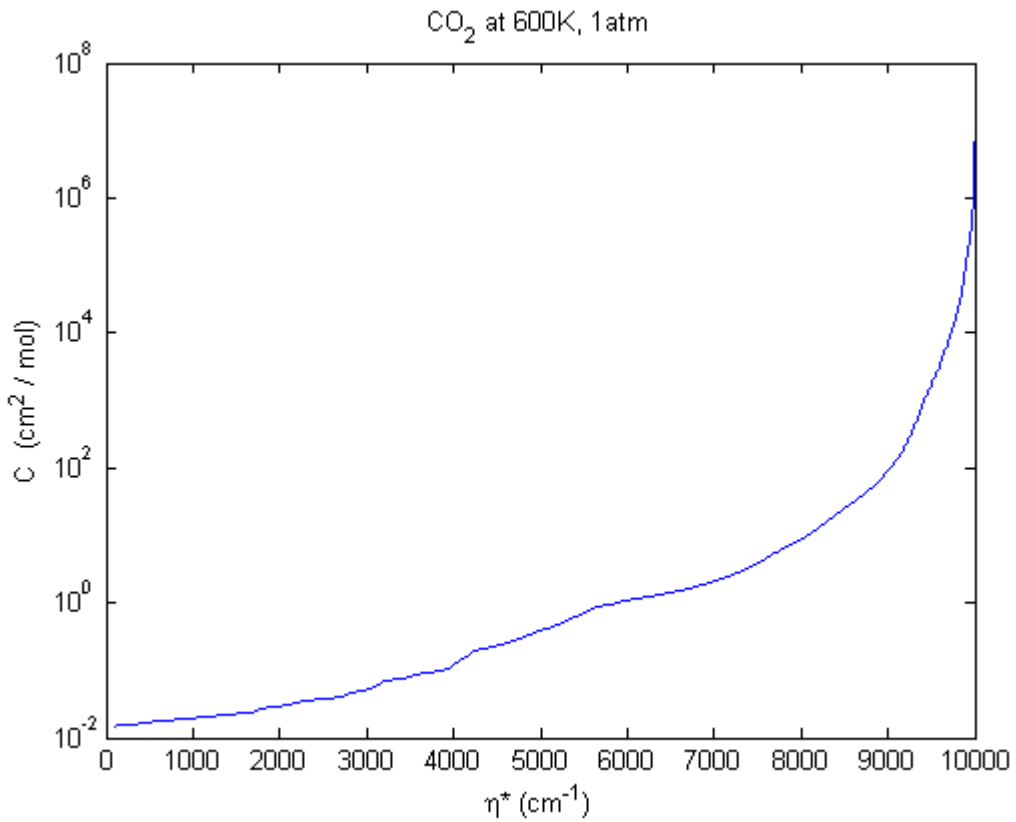


Figure 4.10: CO<sub>2</sub> spectrum in reordered wavenumber space

Unfortunately,  $\eta^*$  is not a very useful variable. While this reordering smooths the absorption coefficient function, it does the opposite for the Planck distribution. The solution to this problem is to absorb the spectral variations of the Planck distribution into the independent variable. This is the second step of the k-distribution process. This step is performed in exactly the same way for both the FSK and SFSK methods. A more formal derivation has been given in the literature [116, 110], but this intuitive description is more convenient for the explanation to follow.

The second step is a scaling of  $\eta^*$ . We weight the modified wavenumber by a fractional Planck distribution at a preselected temperature. Ideally, this weighting function should approximate the distribution of energy within the system which is

generally not spatially invariant and which is likely significantly more complex in reality than a Planck distribution. Fortunately, the usual quantities of interest such as heat fluxes and steady-state temperature distributions are relatively insensitive to the choice of weighting function. Using the gas temperature to generate the Planck distribution weighting function yields Figure 4.11 for our continuing example.

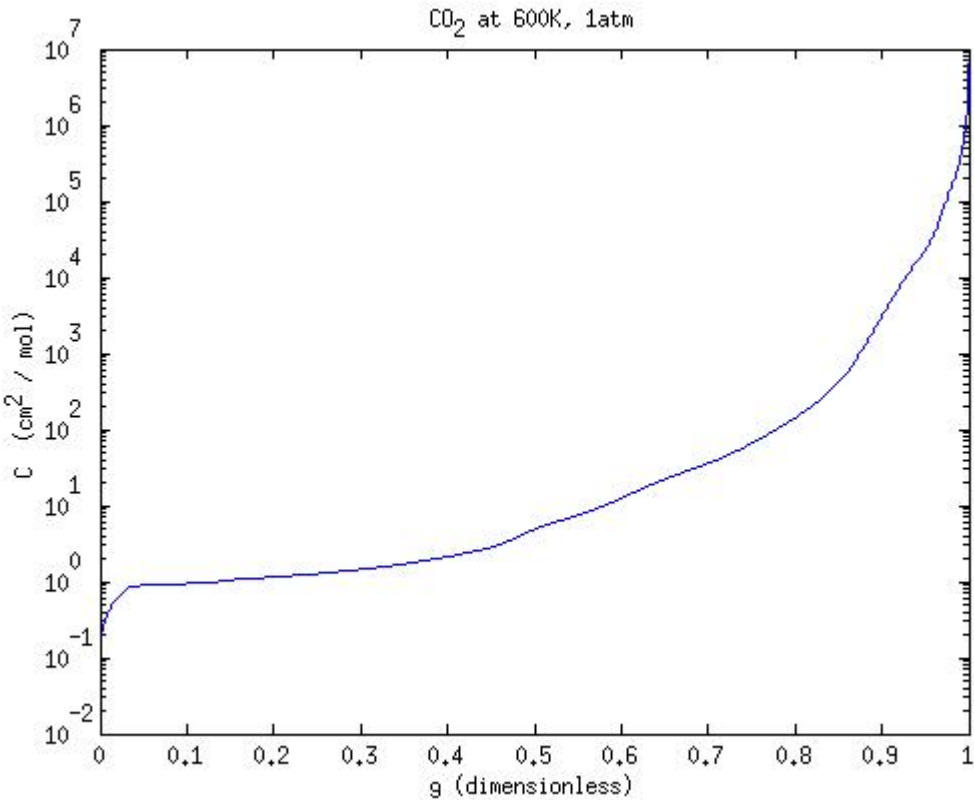


Figure 4.11: Example k-distribution

The choice of weighting function here is analogous to the choice of a spectral flux distribution within an energy group when accounting for spectral self-shielding in a classical multi-group analysis. One would like it to be close to the actual distribution, but it is recognized that the actual solution is relatively insensitive to changes in this

weighting function and that as long as the choice of temperature for the Planck distribution is reasonable that the errors introduced in step two are negligible relative to the errors introduced in step one (for inhomogeneous cases). As will be seen later, the error introduced in step two may become non-negligible when the error from step one is small. However, in these cases the overall error remains small and the proposed error indicator remains a reasonable measure of the error in the k-distribution solution. For this reason, we focus exclusively on the errors associated with the reordering of the spectral absorption coefficient.

As presented, there is no error associated with reordering wavenumber space for a homogeneous problem. The issue arises for inhomogeneous problems where the reordering of wavenumber space is not uniform across the domain. This represents a failure of the so-called scaling approximation.

This is a potentially serious issue since it tends to group optically thick and thin regions of the spectrum together when, in reality they should not interact. For thermal radiation, scattering is generally considered monochromatic. In the classical problem of a hot slab radiating through a cold gas column, this tends to result in a significant overestimation of the total attenuation by the cold gas. In order to eliminate this error, the same reordering in wavenumber may be applied across the entire domain. We define a reference state,  $\overrightarrow{\phi}_{ref}$  with a corresponding spectral absorption coefficient and cumulative k-distribution.

$$g(T_p, \overrightarrow{\phi}_{ref}; C) = \frac{1}{I_b} \int_0^\infty I_{b,\eta}(T_p) H\left(C - C_\eta(\overrightarrow{\phi}_{ref})\right) d\eta \quad (4.26)$$

As a result,  $C\left(g; \overrightarrow{\phi}_{ref}\right)$  is smooth and monotonically increasing. However,  $C\left(g; \vec{\phi}\right)$  is not smooth for a general state. The spectral reordering corresponding to Equation (4.26) is used at all spatial locations, regardless of the local state at those locations. This results in “noisy” k-distributions for every state that is not equivalent to the reference state. It should be emphasized that Equation (4.24) and Equation (4.26) differ in the argument provided. It should be clear that Equation (4.24) depends upon the local gas state and therefore may not be equivalent everywhere within the domain unless the scaling approximation applies. Correlated k-distributions computed using Equation (4.26) do not have this drawback. Unfortunately, they also lack one of the key advantages of the FSK method: the smoothness of the local absorption coefficient with respect to the cumulative distribution variable,  $g$ . Directly evaluating the integral over this  $g$  would be similar to a line-by-line solution and should be avoided. What we seek is a way to estimate the difference between results generated using the curve from Equation (4.24) and those generated from Equation (4.26) without explicitly computing the latter. Figure 4.12 shows the absorption cross-section versus  $g$  for CO<sub>2</sub> at 600K reordered using the same gas at a temperature of 800K as a reference state.

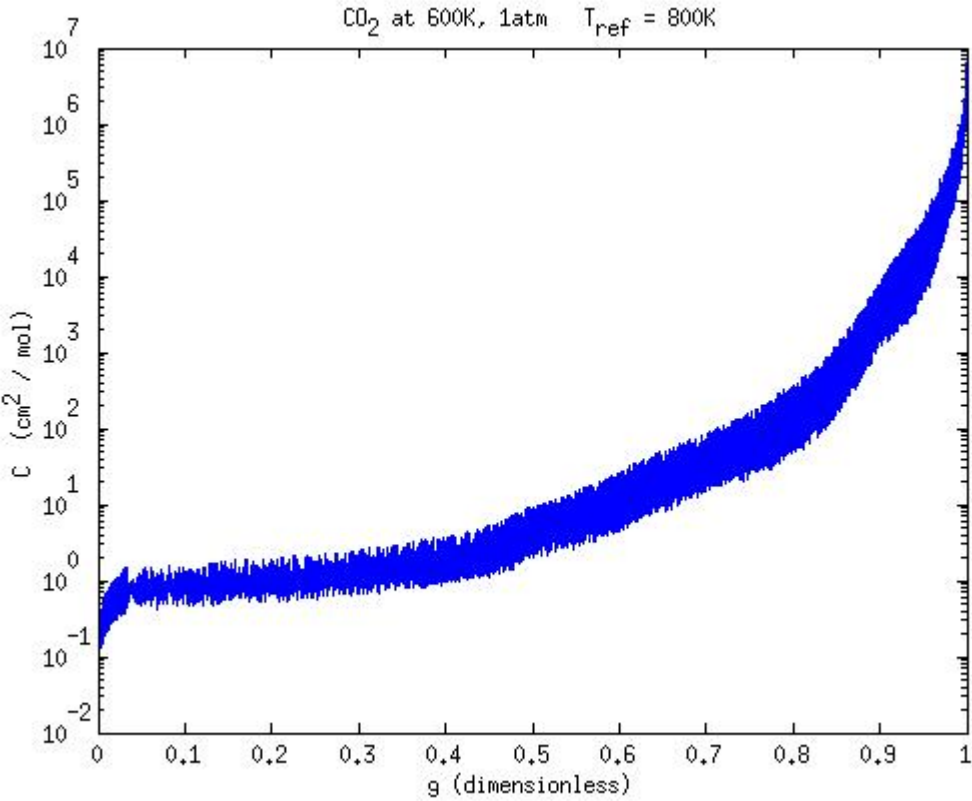


Figure 4.12: Consistent spectral reordering

Figure 4.12 is seen to resemble Figure 4.11 with noise applied to the absorption cross-section. This noise is observed to be multiplicative in nature. In fact, this is the basis for the stochastic full spectrum k-distribution (SFSK) method [126]. For a range of gas and reference temperatures, this “noise” is evaluated as a function of  $g$ . More precisely, we denote the traditional k-distribution generated by smoothing the local absorption coefficient as  $\bar{C}(g)$  and the spectrally consistent k-distribution generated by smoothing the reference state absorption coefficient as  $C(g)$ .

$$\begin{aligned}\bar{C}(g) &= C\left(g; \vec{\phi}_{gas}\right) \\ C(g) &= C\left(g; \vec{\phi}_{ref}\right)\end{aligned}\tag{4.27}$$

The error associated with the inconsistent spectral reordering is modeled. This allows us to estimate the error without ever actually using the spectrally consistent k-distribution.

$$C(g) = \bar{C}(g) \cdot (1 + \varepsilon) \quad (4.28)$$

It is observed that  $\ln(1 + \varepsilon)$  has a consistent and familiar form independent of the local and reference states. Additionally, the mean of the log-noise is approximately 0 for all  $g$ . This is not true for all combinations of  $T_{ref}, T_g$  but remains a reasonable approximation nonetheless. There is some small variation in the magnitude of the noise as a function of  $g$ . As a result,  $(1 + \varepsilon)$  is modeled as a continuous random variable whose probability density function has parameters which are functions of  $T_{ref}, T_g$ , and  $g$ . For convenience of notation, let us define a new variable, the log-error:

$$\gamma(T_{gas}; T_{ref}) = \ln(1 + \varepsilon) \quad (4.29)$$

The error from the example in Figure 4.12 is shown in Figure 4.13.

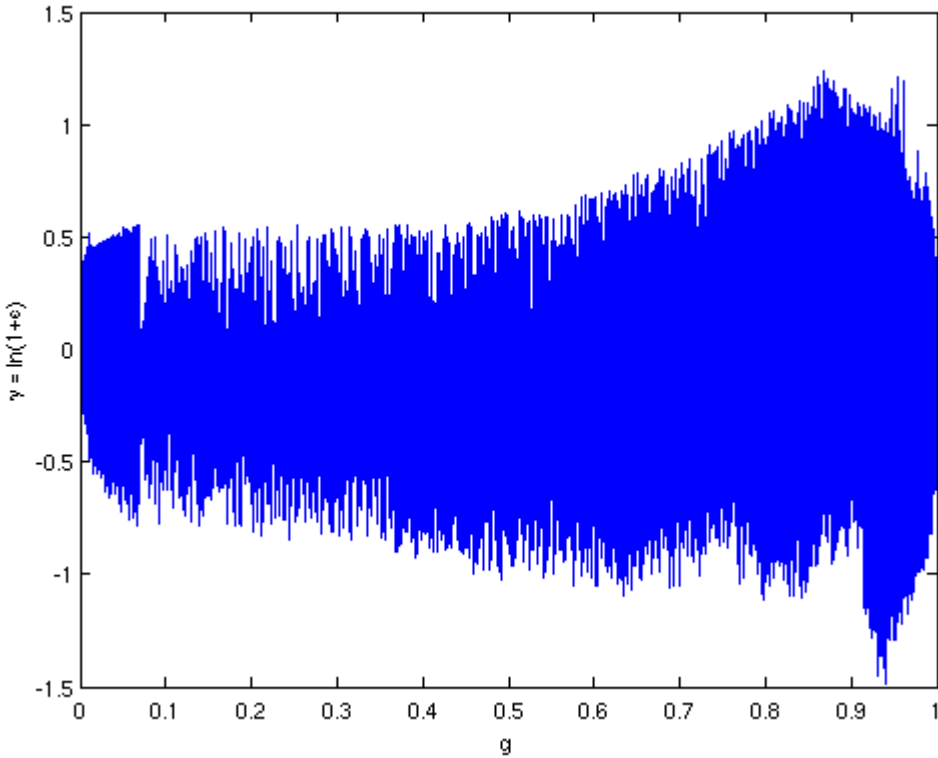


Figure 4.13: Error associated with inconsistent spectral reordering

Clearly, by approximating the physically meaningful error plotted above as the result of a stochastic process with a known probability density function we are losing physics. However, we are greatly reducing computational cost relative to a line-by-line solution or even the multiple fictitious gas models sometimes used to generate accurate solutions of inhomogeneous problems [118, 127, 128]. To gain intuition about the structure of this probability density function, we generate histograms of  $\gamma$  in small enough intervals of  $g$  that we may assume that the error parameters are constant within each interval. A histogram from one such interval is plotted in Figure 4.14. It is also important that these intervals of  $g$  be large enough that a statistically significant number of samples for fitting the probability density function are contained within each one.

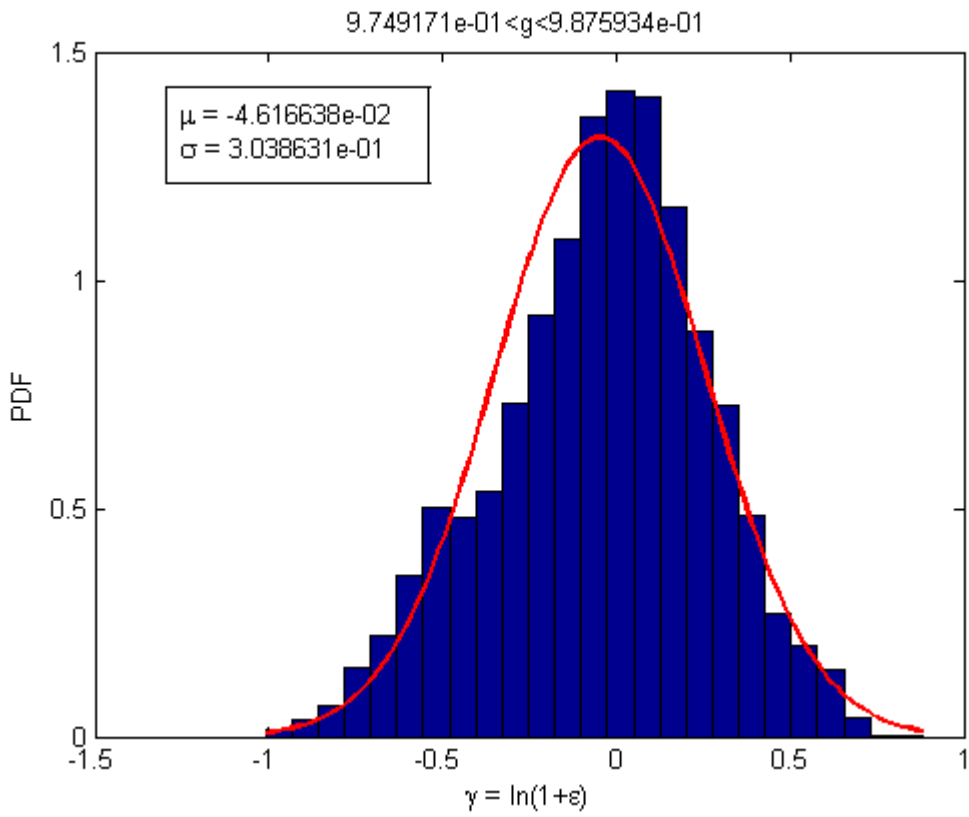


Figure 4.14: Histogram of error due to spectral reordering

### Estimating Parameters for the SFSK Method

The general form of this reduced probability density function is consistent across all of the combinations of gas and reference temperatures examined provided that the reference temperature is not significantly lower than the gas temperature. If the reference temperature is much higher than the gas temperature, the PDF is broader but the results remain self-similar.

$$P(\gamma; \mu, \sigma) = \frac{1}{\sigma\sqrt{2\pi}} e^{\frac{-(\gamma-\mu)^2}{2\sigma^2}} \quad (4.30)$$

The normal distribution has two parameters, the mean and the variance, which must be found as functions of  $T_{ref}$ ,  $T_g$ , and  $g$ . Initially, it was assumed that in order for the results to remain meaningful that the expected value of the noise be the identity:

$$E[\varepsilon] = 0 \quad (4.31)$$

This is equivalent to requiring that the expected absorption coefficient be the absorption coefficient provided by the traditional k-distribution method. This additional requirement places a constraint on the mean and the variance such that there is really only a single degree of freedom for fitting the distribution. The required relationship between the mean and the variance is given by

$$\sigma^2 = -2\mu \quad (4.32)$$

This constraint may only be satisfied when  $\mu \leq 0$ . This restriction on the mean is due to the symmetry of the normal distribution. Since the actual variation occasionally has a positive mean within a range of  $g$ , a problem exists. This problem tends to only manifest itself for small values of  $g$  and is resolved by an alternative estimation of the mean and variance. The variance may be calculated using the following equation.

$$\sigma^2 = \left( \sum_{i=1}^N (\gamma_i - \mu)^2 \right) / N \quad (4.33)$$

Here the  $\gamma_i$  values represent function evaluations for the log-error at each sampling point,  $g_i$ . Combining equations (4.32) and (4.33) yields a quadratic equation which must be satisfied in order for both to hold.

$$0 = \mu^2 - 2(\bar{\gamma} - 1)\mu + \bar{\gamma}^2 \quad (4.34)$$

The over-bar in equation (4.34) represents an averaging over the  $g$ -domain of interest. Enforcing this condition is necessary because the mean value of the noise when calculated in a traditional way is occasionally positive, especially for small values of  $g$ . When the mean of the noise is negative, the actual mean may be used with a variance calculated using equation (4.32). This generally results in a slightly higher variance than the maximum likelihood estimate of variance with the mean and variance treated independently.

When the mean of the noise is positive, equation (4.34) may be used to calculate the appropriate distribution mean. There are generally two negative real roots to choose from. The smaller root is always approximately -2 since  $\bar{\gamma}$  and  $\bar{\gamma}^2$  are usually both very small. The larger root tends to be a small negative number ranging in magnitude between  $10^{-1}$  to machine precision depending upon the relative magnitudes of  $\bar{\gamma}$  and  $\bar{\gamma}^2$ . It is suggested that the more negative root be used as this gives larger values for the variance which may be considered to be a more conservative estimate. However, this approach to approximating the mean and variance is seen to be unnecessarily restrictive.

If the constraint from Equation (4.31) is relaxed, the mean and variance may be found independently by maximum likelihood estimation. It is important to distinguish between the maximum likelihood estimation of the parameters in a normal distribution on  $\gamma$  and the parameters of a log-normal distribution on  $(1+\varepsilon)$ . The latter is the appropriate approach. It is observed that this approach still reproduces the k-distribution predictions for heat flux even if the expected value of the absorption coefficient is slightly different. Since this technique includes more physical information, it is expected

to be better than the approach embodied by Equation (4.34). This expectation is played out in the examples to follow.

Once the uncertainty in the absorption coefficient is determined as a function of  $T_{ref}$ ,  $T_g$ , and  $g$ , the uncertainty is propagated forward to the prediction of the radiative flux divergence. This may be accomplished numerically in a number of ways. The salient point being that the RTE is transformed from a partial differential equation (PDE) to a stochastic partial differential equation (SPDE) with the introduction of the uncertain absorption coefficient parameter. This SPDE may be solved for the distribution of the radiative flux divergence using Monte Carlo methods. Since we are often only interested in the approximate magnitude of the error a relatively small number of samples (10-20) may suffice for an acceptable estimate. Uncertainty quantification of numerical predictions almost always comes at a cost relative to the prediction itself. While the SFSK method represents an order of magnitude increase in computational expense relative to the FSK method it is still many orders of magnitude cheaper than a line-by-line solution. Additionally, the Monte Carlo samples are completely decoupled from each other making this process trivially parallelizable to a certain extent.

It is also important to note that the errors are not independent random variables. As one might expect, they are correlated. We assume that this correlation is independent of  $g$ . This assumption will be discussed in more detail later. We simulate the interdependence of the error using a Gaussian copula. Copulas are used to describe the dependencies between different random variables. The most important theorem on the subject is Sklar's theorem. In our case, the variables are discrete instances of  $\gamma$  as a function of two varying gas temperatures. The reference temperature is included as a parameter. The dependence upon  $g$  is ignored and all of the data from the high resolution spectrum is used as a single sample. The assumption here is that while the

marginal PDFs depend upon  $g$ , the correlation function does not. This assertion is supported by the scatter plot in Figure 4.15.

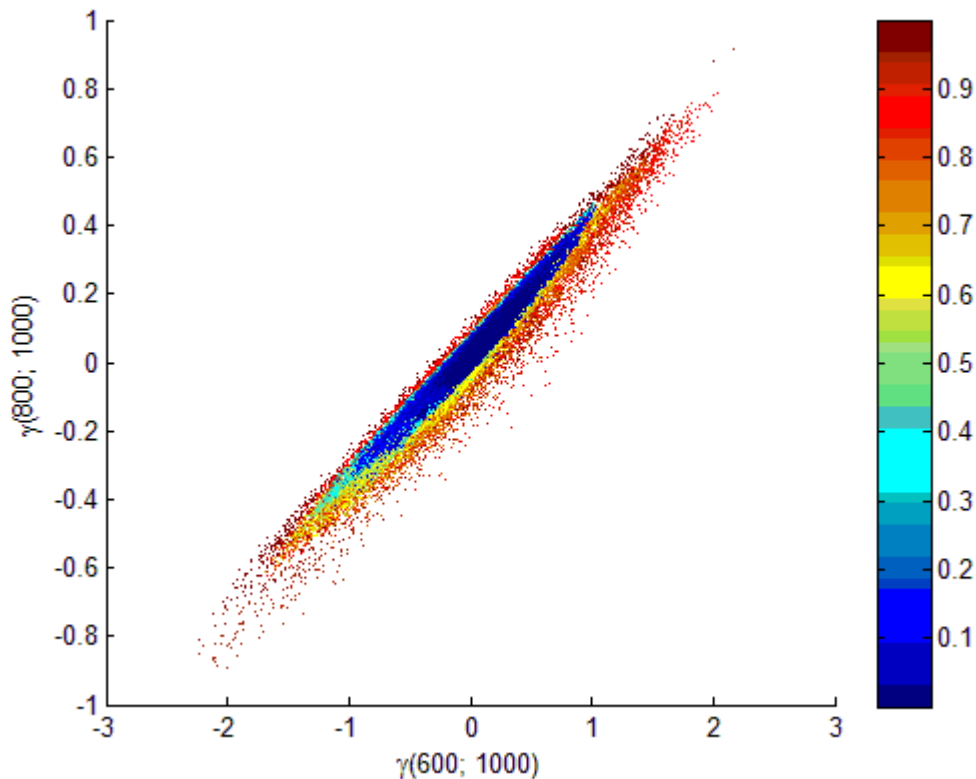


Figure 4.15: Scatter plot of log-error as a function of  $g$

The color-scale in Figure 4.15 represents the value of  $g$  corresponding to each point. The marginal distribution tends to be broader for large  $g$  but the correlation structure tends to remain unchanged.

Rank correlation coefficients represent the degree to which large or small values of one random variable correspond to large or small values of another random variable. This is contrasted with the commonly used Pearson product-moment correlation

coefficient which represents the degree to which two random variables are linearly related.

Copulas are a related concept. First the distributions of the two random variables are replaced by their marginal cumulative distributions. By definition, the resulting random variables are uniformly distributed over  $[0,1]$ . A copula is capable of describing the dependence among any number of such random variables. For a Gaussian copula the dependence is represented in a way that is reminiscent of a multivariate normal distribution. The Gaussian copula only considers pairwise dependence among the variables which is appropriate for our application. More information on rank correlation coefficients and copulas may be found in the literature [129, 130, 131].

The gas temperature space is discretized. For each gas temperature,  $T_{\text{gas}}^{(i)}$  the log-error is transformed using its cumulative distribution function resulting in a random variable that is uniformly distributed on the interval  $[0,1]$ . The rank correlation matrix is then generated. The rank correlation matrix is a discrete representation of the correlation function that relates the errors at any two states. The correlation function has values between -1 and 1. Values approaching  $\pm 1$  signify functional dependence while values approaching 0 indicate independence. Intuitively, the following properties hold:  $\rho(T_{\text{gas}}^{(i)}, T_{\text{gas}}^{(j)}; T_{\text{ref}}) = \rho(T_{\text{gas}}^{(j)}, T_{\text{gas}}^{(i)}; T_{\text{ref}})$ ,  $\rho(T_{\text{gas}}^{(i)}, T_{\text{gas}}^{(i)}; T_{\text{ref}}) = 1$ , and  $\rho(T_{\text{gas}}^{(i)}, T_{\text{ref}}; T_{\text{ref}}) = 0$ . The last property is a direct consequence of the definition of the reference state which dictates that  $\gamma(T_{\text{ref}}; T_{\text{ref}}) = 0$ .

Figure 4.16 shows a contour plot of the absolute value of the correlation function. The sign of the correlation function is seen to obey

$$\text{sign}\left(\rho(T_{\text{gas}}^{(1)}, T_{\text{gas}}^{(2)}; T_{\text{ref}})\right) = \text{sign}\left((T_{\text{gas}}^{(1)} - T_{\text{ref}})(T_{\text{gas}}^{(2)} - T_{\text{ref}})\right) \quad (4.35)$$

In other words, if the two temperature are either both above or both below the reference temperature, their associated errors are positively correlated. If one is above and the other below, their associated errors are negatively correlated. If either temperature is equal to the reference temperature, their associated errors are uncorrelated unless both are equal to the reference temperature in which case their errors are equivalent.

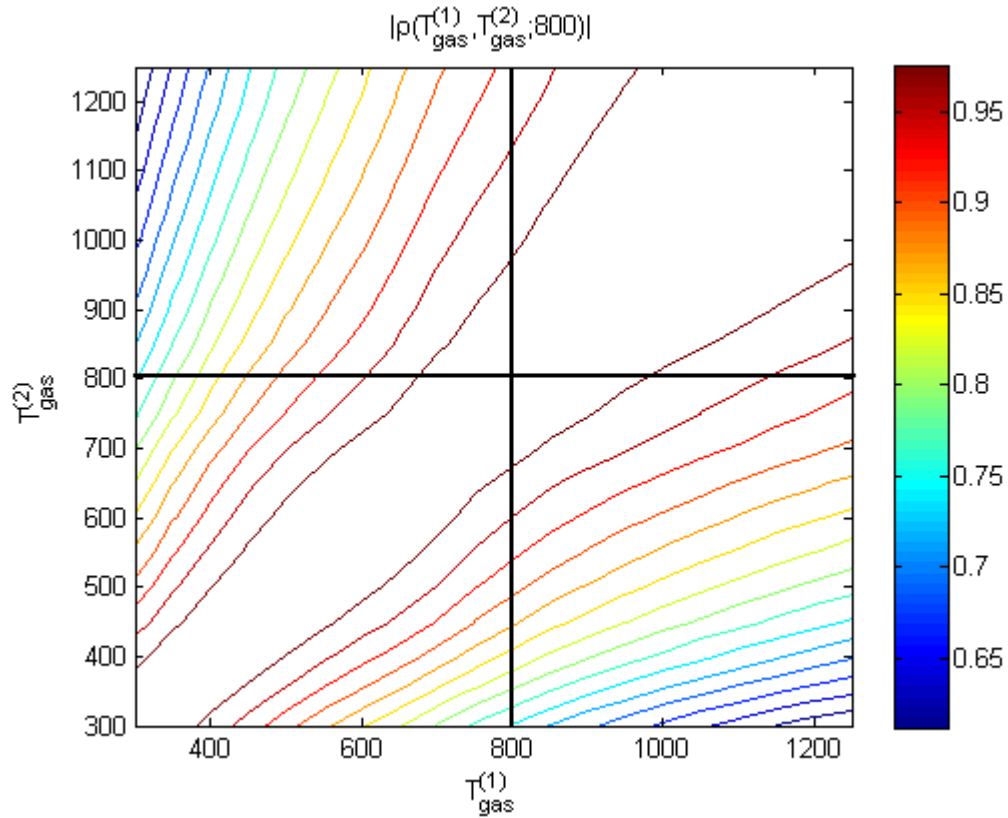


Figure 4.16: Example correlation function

In the current work, the correlation between any two temperatures is found by interpolation. However, it would be possible to establish an approximate functional form for  $\rho(T_{\text{gas}}^{(1)}, T_{\text{gas}}^{(2)}; T_{\text{ref}})$ . For general use, this would be much faster and may be

recommended. The correct form for the empirical relation would need to be determined before any such curve fit could be performed.

When propagating the uncertainty forward to the predicted heat flux, this correlation function may be used to generate random values in  $[0,1]$  with the same dependencies as  $\gamma$ . These values may then be mapped back to instances of the log-error using the appropriate inverse CDF. It is possible to use the empirically determined CDF and inverse CDF for this process. Alternatively, the CDF corresponding to the modeling of the error as log-normal may be used. The former is more precise while the latter is faster and more well-suited for the construction of parameter databases and empirical correlations.

## SFSK Results and Discussion

Examples are now presented to demonstrate the application of this approach for the estimation of errors due to the k-distribution assumptions.

Consider a gas slab at 1atm with a 10% molar concentration of CO<sub>2</sub>. The slab is 1m thick and is bounded on both sides by cold black walls. The left half of the slab has a uniform hot temperature of 1000K. The right half of the slab has a uniform cold temperature of 300K.

$$T(x) = \begin{cases} 1000 & x \leq L/2 \\ 300 & x > L/2 \end{cases} \quad (4.36)$$

This type of problem with large temperature gradients or discontinuities has proven to be extremely challenging for the k-distribution method. Using the high temperature as a reference state, the k-distribution method does an excellent job of predicting the heat flux in the left half of the slab. However, the k-distribution method

tends to significantly over-predict attenuation in the right half of the slab. This is the result of grouping all optically thick spectral regions together when in reality some spectral regions which are optically thick in the hot region are relatively optically thin in the cold region. Essentially, the vast majority of the energy is emitted by optically thick regions in the left half of the slab. In reality, a significant amount of that energy is rapidly attenuated by optically thick spectral intervals in the right half of the slab while a lesser but still significant amount is attenuated more slowly in more optically thin spectral regions.

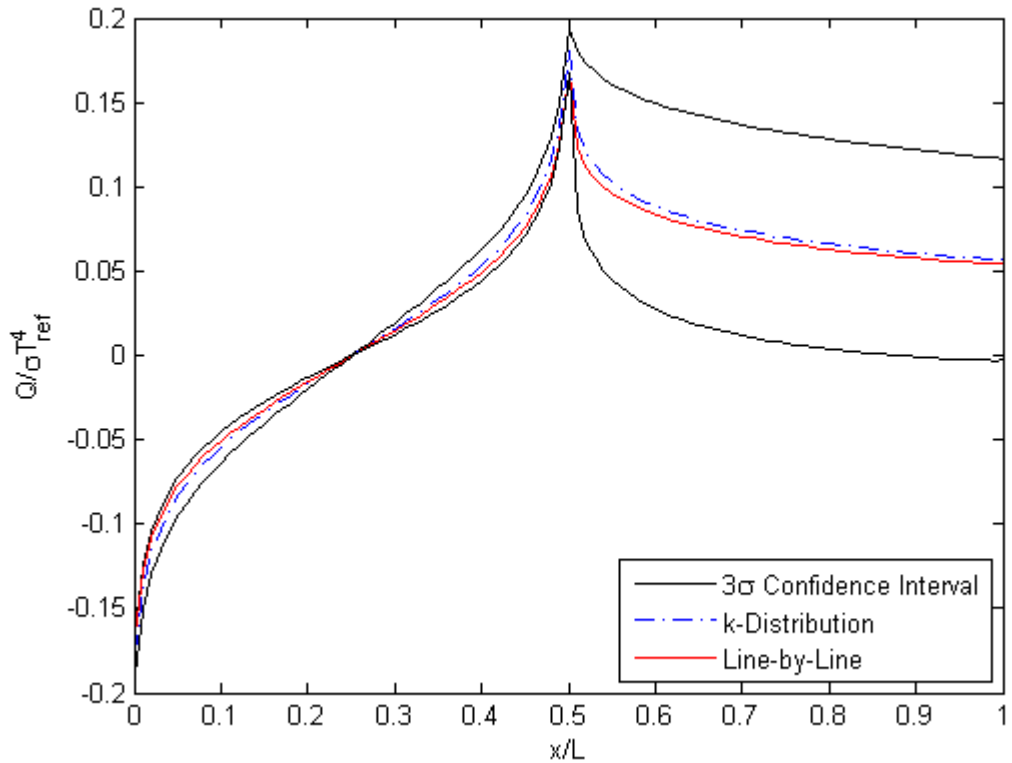


Figure 4.17: Heat flux distribution in slab with large temperature jump

As may be seen from Figure 4.17, the actual heat flux (red line) is everywhere contained within the three standard deviation confidence intervals generated by propagating the uncertainty in the absorption cross-section forward into the predicted heat flux. The reference temperature for this example is 850K. This was chosen to represent the average emissive power.

$$T_{ref}^4 = \frac{\int_0^L T^4(x) dx}{L} \quad (4.37)$$

If a higher reference temperature is chosen, near the hot slab temperature of 1000K the error and uncertainty both decrease in the hot region while increasing in the cold region. Lower reference temperatures produce the opposite effect. This is because the heat flux is dominated by emission from the hot region.

The error in the k-distribution method is exacerbated in this problem by the almost negligibly low emission from the right half of the slab. This makes this problem particularly challenging for the full-spectrum correlated k-distribution method. Normally, over-estimation of the attenuation by the k-distribution method is somewhat offset by an over-estimation of the emission as well. However, it is something to keep in mind for almost purely attenuating problems such as this one.

As a second illustration, consider another slab with the same pressure and concentration with the same vacuum boundary conditions. The slab has a linearly varying temperature profile.

$$T(x) = 300 + 950 \left( \frac{x}{L} \right) \quad (4.38)$$

With a more realistic temperature distribution, the k-distribution does not tend to exclusively under or over predict the heat flux. Consequently, the k-distribution method produces a more accurate result for this problem although the error behaves less predictably. The corresponding confidence interval once again bounds the line-by-line solution providing increasing confidence in our error metric. It should be reiterated that although the confidence intervals bounds the line-by-line solution for this particular case that this is not generally true. The three standard deviation confidence interval represents an error indicator and should not be used as an absolute bound. The error introduced by assuming a spectral intensity distribution is still present and is noticeable when the predicted confidence intervals are extremely narrow.

For this case, any reference temperature greater than approximately 500K resulted in a confidence interval which everywhere bounded both the k-distribution and line-by-line solutions. The average medium temperature (775K), the temperature corresponding to the average emissive power ( $\sim$ 900K), and the maximum medium temperature (1250K) all yielded satisfactory results when used as the reference temperature for this problem.

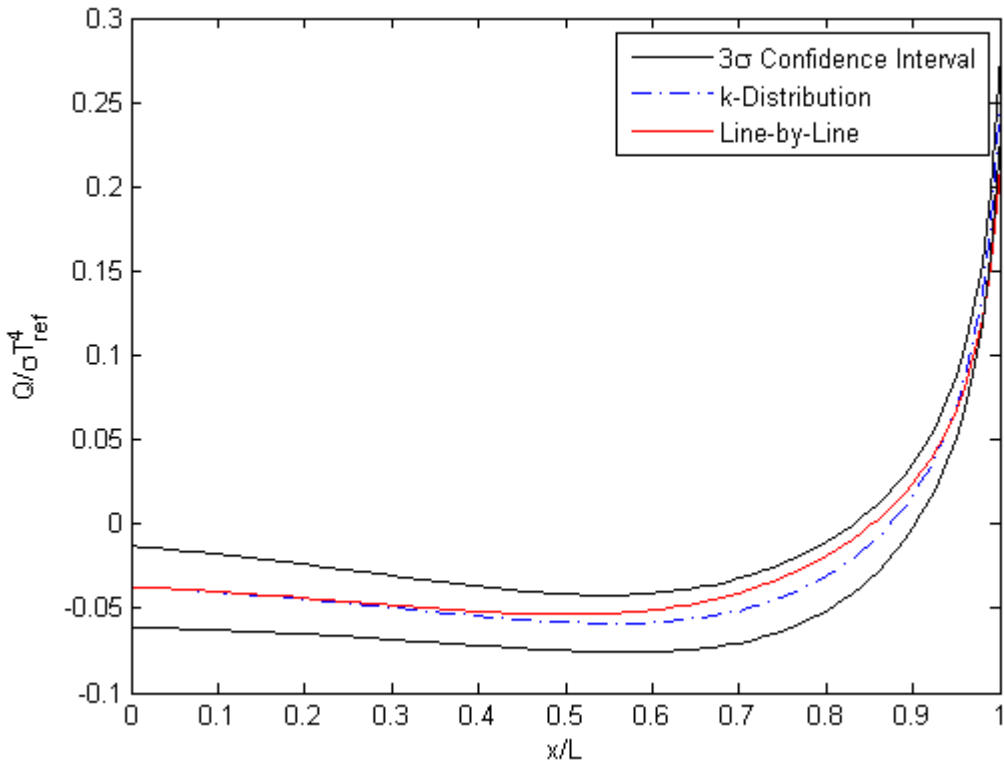


Figure 4.18: Heat flux distribution in slab with linear temperature variation

The reference temperature of 900K corresponding to the average emissive power is used again for this example. The choice of reference temperature can have a significant impact on the k-distribution result. Poor choices of reference temperature may result in large errors in the predicted heat flux. Poor choices of reference temperature also correspond to wide marginal distributions which produce wide confidence intervals and little confidence in the solution. If the reference temperature is too low, the confidence intervals may not bound the line-by-line solution. It is theorized that this is the result of error introduced by using a grossly inaccurate approximation when representing the distribution of energy within the system. Recall that this error was assumed negligible when compared with the error associated with the spectral reordering.

A third example includes a quadratic temperature profile.

$$T(x) = 1000 - 2000 \left( \frac{x}{L} \right)^2 \quad (4.39)$$

The reference temperature corresponding to the average emissive power for this temperature distribution is 850K. Once again, the total pressure is fixed at a constant 1 atmosphere. The mole fraction of CO<sub>2</sub> is 10%. There are no other participating species. The ideal gas law is used to compute the number density of the participating species.

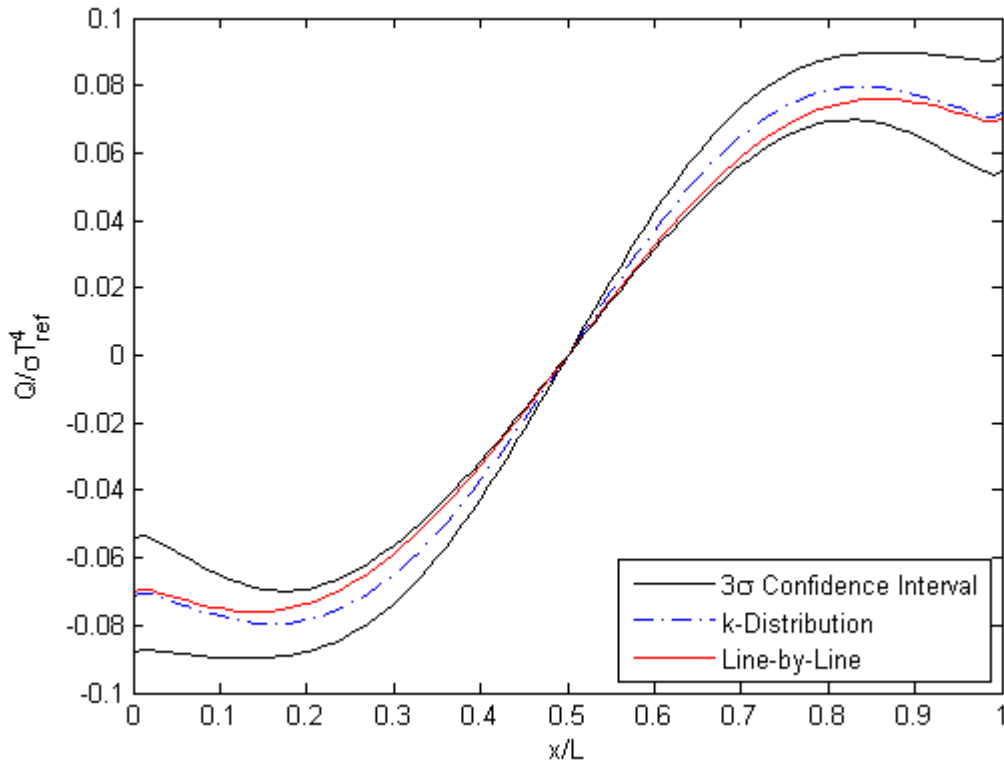


Figure 4.19: Heat flux distribution in slab with quadratic temperature variation

Once again, the confidence interval bounds the error in the heat flux while also approximating it spatially.

Consider a cosine temperature distribution.

$$T(x) = 1250 \cos\left(\frac{x}{L}\right) \quad (4.40)$$

The reference temperature corresponding to the average emissive power for this temperature profile is approximately 1100K. It should be mentioned that for these examples all reference temperatures are rounded to the nearest 50K since those are the temperatures for which error parameters from high-resolution spectral data have been generated. This avoids the need to interpolate in the reference temperature space.

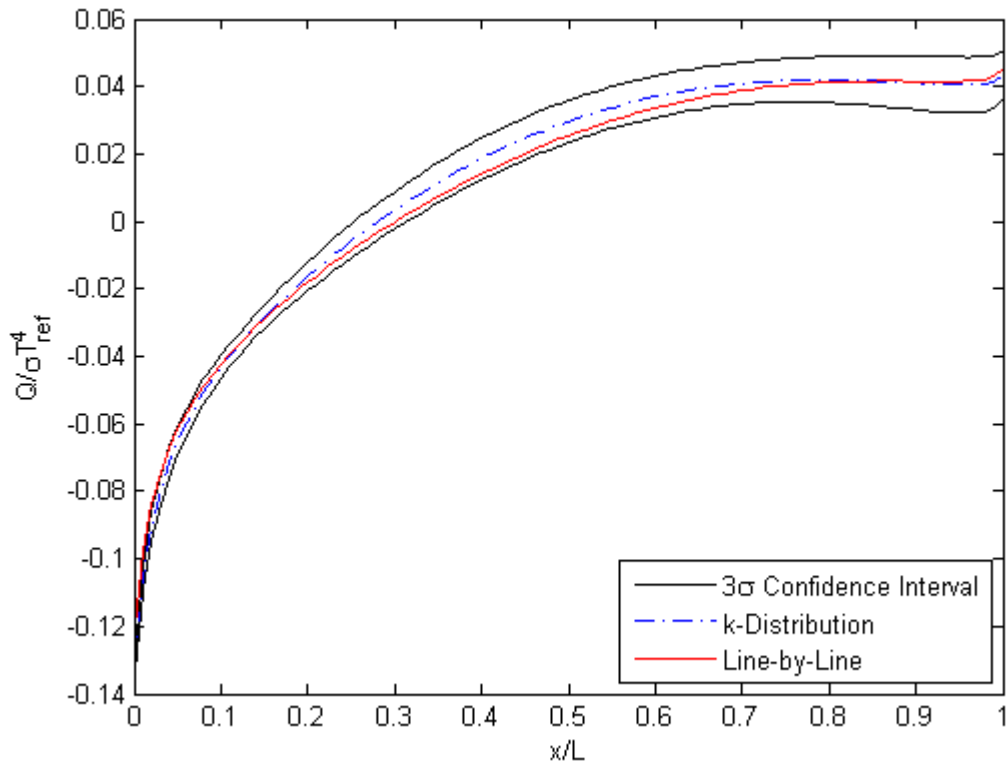


Figure 4.20: Heat flux distribution in slab with cosine temperature variation

For very small values of  $x$ , the confidence interval does not bound the error in this case. While the error is still relatively small here, it is not sufficiently represented by the confidence intervals. This is a result of additional error introduced by the assumption of a known spectral intensity distribution. In the high-temperature region near the wall, the spectral intensity is poorly represented by the assumed Planck distribution. Figure 4.21 contrasts the assumed spectral intensity distribution with the actual spectral intensity found from line-by-line calculations.

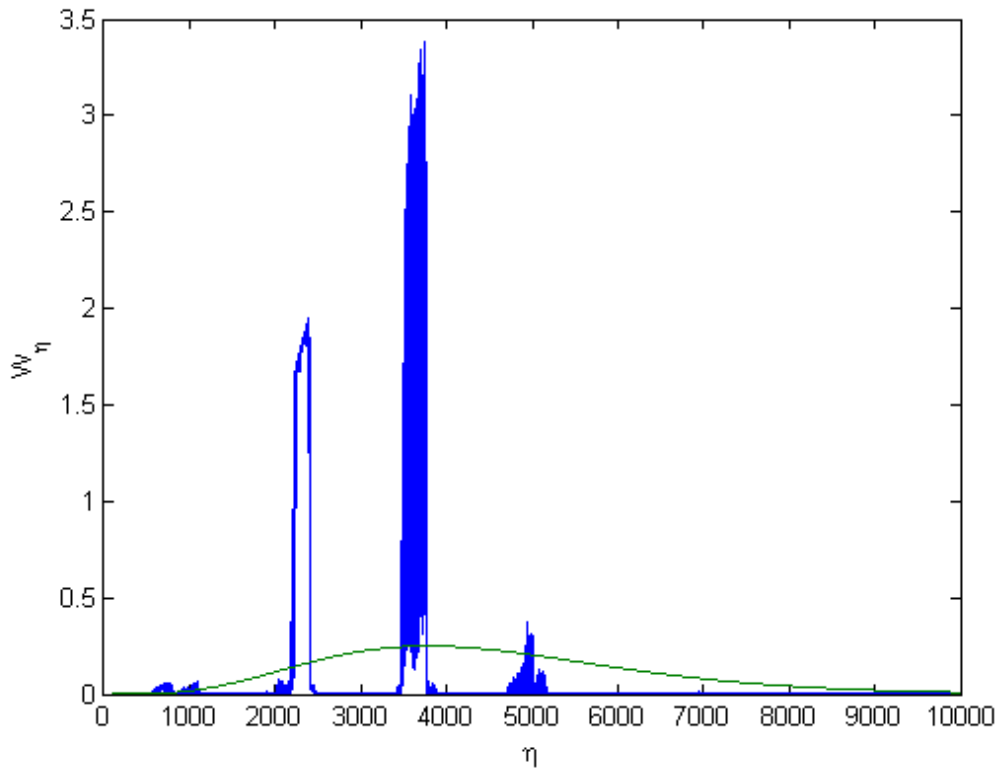


Figure 4.21: Actual vs. assumed spectral intensity at left wall in a slab with a cosine temperature variation; Intensity units are arbitrary

The actual spectral intensity is plotted at the wall. Both curves in Figure 4.21 are normalized so as to integrate to unity. The actual magnitude is unimportant. The quantity of interest here is the relative weighting of the different spectral regions. The discrepancy represented here accounts for the additional error seen in Figure 4.20. Unfortunately, in real applications, the actual spectral intensity is unknown a priori making error introduced in this way difficult to quantify. Fortunately, this error is small and is only significant when other sources of error are also small. It may be appropriate to compensate for this error by setting a minimum width for the proposed confidence intervals.

Consider the sinusoidal temperature profile

$$T(x) = 300 + 950 \sin\left(\frac{\pi x}{L}\right) \quad (4.41)$$

The reference temperature corresponding to the average emissive power for this temperature distribution is approximately 1000K.

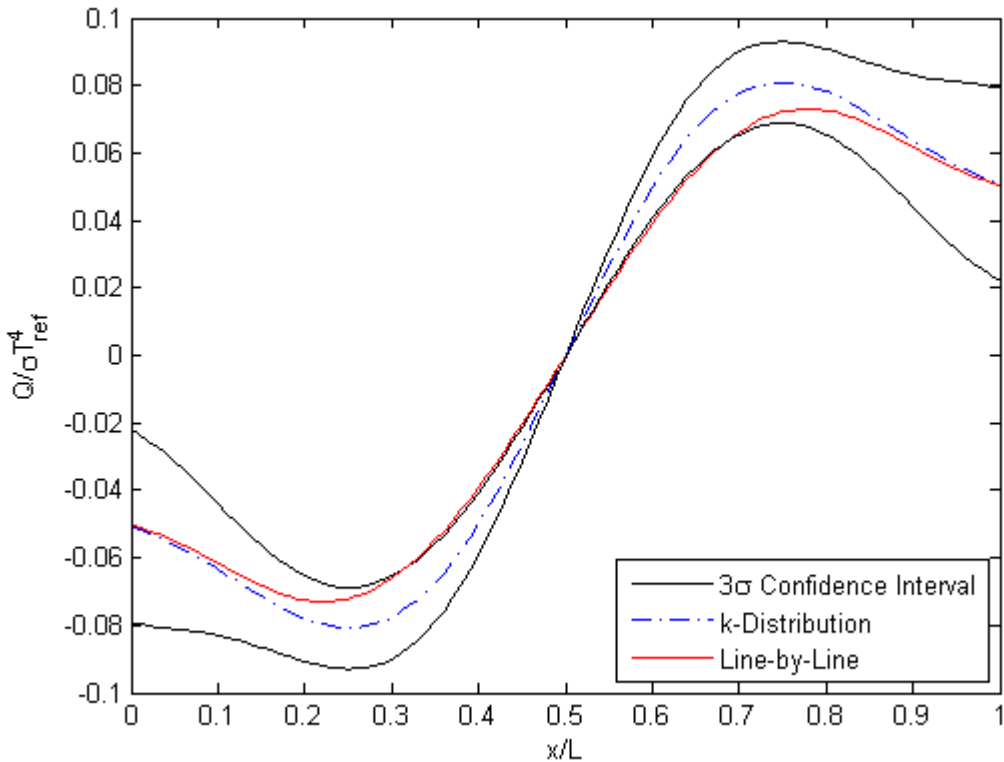


Figure 4.22: Heat flux distribution in slab with sine temperature variation

The broad peak near the center of the domain creates a region just outside it in which the error from both sources is relatively large. Even so, the three standard deviation confidence interval nearly captures all of the error. It also successfully captures the rate at which the error grows as the solution diverges from the symmetry plane.

Consider a temperature distribution that decays exponentially.

$$T(x) = 1250e^{(-2\pi x/\delta L)} \quad (4.42)$$

The reference temperature corresponding to the average emissive power for this temperature distribution is approximately 850K.

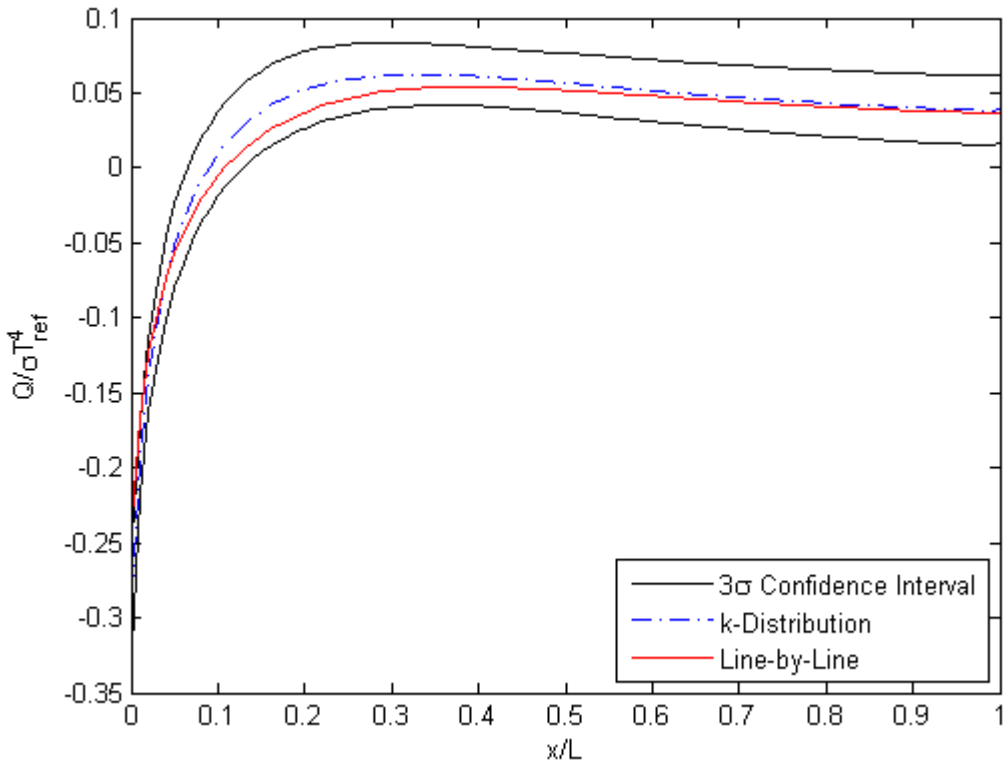


Figure 4.23: Heat flux distribution in slab with exponential temperature variation

Similar to the cosine temperature variation, the error is bounded almost everywhere by the three standard deviation confidence interval. It exceeds this threshold near the peak of the temperature distribution where the magnitude of the heat flux is greatest and the relative error is small.

### SFSK Conclusions

The process of estimating the model-form uncertainty intrinsic to the k-distribution method as a log-normal multiplicative uncertainty in the absorption coefficient is demonstrated. This process is shown to be sufficient for a set of inhomogeneous 1-D example problems with CO<sub>2</sub> as the only participating species. Temperatures in the range from 300-1250K were examined. A database of the

distribution parameters (mean and standard deviation) as functions of gas and reference temperature as well as  $g$  was created. This database was used to solve a number of example problems, six of which are included here. It is expected that the applicability of this technique will extend to CO<sub>2</sub> at other pressures. It is hoped that a similar methodology will be shown to work for other gas species, especially H<sub>2</sub>O and mixtures of CO<sub>2</sub> and H<sub>2</sub>O with pressure and concentration gradients. The inclusion of concentration gradients presents a substantial additional obstacle as it introduces several important questions. Must the database be constructed with concentration as another independent variable? Is it possible to impose some sort of mixture rule? This is a topic of further research.

The restriction on the expected value of the absorption coefficient in Equation (4.31) is seen to be excessively restrictive. The expected value of the heat flux is observed to behave as expected without this additional constraint. Removing this constraint requires the inclusion of two parameters in order to describe the error distribution rather than only one. The freedom afforded by the extra parameter allows for a more accurate portrayal of the error distribution and consequently, a more representative error indicator for the heat flux and flux divergence predictions.

## SPECTRAL INTEGRATION CONCLUSIONS

For 1-D applications where high accuracy is of the utmost importance, the MSFSK method performs well. The consistent convergence properties provide an avenue for quantifying the error due to spectral approximations. For 1-D applications, the error introduced by the approximation of the spectral properties often dwarfs the error introduced by spatial or angular discretization. In the MSFSK method, the dependence of the spectral properties upon the local gas state is not treated directly. Rather than

approximate the dependence of the optical properties upon the state, the state itself is approximated. This circumvents the main problem associated with quantifying the error associated with the spectral integration. However, the MSFSK method remains a computationally expensive method relative to other spectral integration techniques. Furthermore, the MSFSK method is restricted to 1-D applications. When appropriate, the MSFSK method is a good choice. However, the domain of applicability of the method is restrictive enough that its use is not generally advisable. Other, less computationally expensive methods may provide similarly accurate solutions for more general problem spaces.

The full spectrum k-distribution method represents an inexpensive alternative to line-by-line or MSFSK method calculations. The full spectrum k-distribution method is shown to be exact for problems with homogeneous media [116]. It is shown to produce errors when applied to media with temperature, pressure, or concentration gradients except in the case when the spectra remain correlated [110]. Unfortunately, real gas spectra tend not to be correlated across changes in temperature, pressure, or concentration. Some gases such as carbon dioxide have optical properties which are relatively insensitive to changes in pressure. Other gases such as water vapor are more sensitive to pressure variations.

When temperature, pressure, or concentration gradients are present, the full spectrum k-distribution method produces errors due to two different assumptions. The first assumption is that the absorption coefficient spectra at different locations within the medium are correlated. Errors due to this assumption may be estimated by treating the gray-gas absorption coefficients found via the full spectrum k-distribution method as uncertain parameters. This is the stochastic full-spectrum k-distribution (SFSK) method. Propagating this uncertainty to quantities of interest such as the heat flux or radiative flux

divergence term in the energy equation requires the solution of the stochastic radiative transport equation.

The second assumption involves the spectral weighting. The absorption coefficient should be weighted by the incident intensity. Unfortunately, the incident intensity is not known a priori. Instead, a distribution (usually a Planck distribution) is assumed. The temperature at which to evaluate this Planck distribution is selected to represent the average emission from the medium. The temperature corresponding to the average emissive power is a reasonable choice. Errors due to this assumption are generally small but may become significant when other sources of error are similarly small.

The full spectrum k-distribution method is a robust choice for approximating the spectrally integrated intensity. It provides significant computational savings when compared to line-by-line or MSFSK solutions. When uncertainty quantification is desired, the absorption coefficient may be treated as uncertain resulting in confidence intervals for important quantities such as the heat flux or radiative flux divergence. The SFSK method is a robust choice for providing a spatially resolved error indicator to accompany FSK predictions.

## Chapter 5: Summary and Conclusions

The radiative transport equation defines the transport of radiative intensity throughout an absorbing, emitting, and (potentially anisotropically) scattering medium. The radiative intensity is a function of seven independent variables. These variables are time, space, direction, and wavenumber. There may be up to three spatial variables and two directional variables. The characteristic time scale for the radiative transport equation is a characteristic length for the system divided by the speed of light. The temporal derivative term in the radiative transport equation is divided by the speed of light. This characteristic time scale tends to be significantly shorter than the time scales for other heat transfer modes. As a result, the temporal derivative term is commonly neglected and the radiative transport equation is treated as steady-state. When coupled to other heat transfer modes, the energy equation is not necessarily steady-state. In fact, even when only radiation is present, the thermal capacitance in the material energy necessitates the inclusion of time. However, the radiative transport may still be approximated as steady-state at each time step since the radiative intensity distribution equilibrates on a much shorter time scale than any other relevant physics in most problems.

The angular distribution of the radiative intensity may vary from a constant to a Dirac delta. Because of computational constraints, low order approximations of the angular distribution are commonly used. In some cases, the approximate distribution will approach the exact distribution as higher order approximations are used. This is the case for the discrete ordinates and spherical harmonics methods. In practice, very low order angular approximations are common and tests to assure sufficient convergence of the

angular approximation are less common. Such tests are often only concerned with the elimination of ray effects from discrete ordinates solutions.

Other methods rely on assumptions that do not provide an easy extension to higher order approximations. Moment methods such as M1 are examples of this type. Still other methods rely on assumptions that cause them to fail to converge to the exact solution even given an infinite number of terms. The simplified spherical harmonics method will not generally converge to the exact solution as the order of the expansion approaches infinity unless certain additional conditions are met [132]. However, the simplified spherical harmonics expansions have been seen to provide more accurate results than low order spherical harmonics expansions for certain problems. For 1-D applications, the spherical harmonics and simplified spherical harmonics methods are equivalent. The SP<sub>1</sub> and P<sub>1</sub> methods are also equivalent for 2-D and 3-D geometries.

Because each of these approximations assumes a different form for the intensity distribution they produce different results for the same set of conditions. Their accuracy varies with problem parameters such as optical thickness and scattering albedo. As one might expect, each method does best when the actual intensity distribution is similar to the assumed intensity distribution for that method. For low order approximations, the error will be lessened the more isotropic the actual intensity field.

For discrete ordinates methods, discontinuities in the angular intensity distribution cause spurious oscillations known as ray effects. These oscillations tend to produce large errors and can cause stability problems in coupled codes for combined-mode problems. The other methods considered are all fundamentally diffusive. They do not produce spurious oscillations even in the presence of discontinuities. However, they also tend to smooth out any discontinuities and perform poorly in optically thin media. Large relative errors from these methods tend to develop when the actual angular

intensity distribution is highly peaked. An exception to this rule is the simplified spherical harmonics approximations which perform well so long as the solution is locally 1-D. A scenario which might produce a strongly peaked angular intensity is a point source. A more realistic scenario might be a localized volumetric source in an optically thick media without scattering. The optical thickness is a non-dimensional parameter defined as the product of the extinction coefficient and a characteristic length scale. The problem of estimating the heat flux incident on a distant surface due to radiation from a fire through a potentially sooty environment would be one example. The radiant energy reaching the surface from the fire would likely have a highly peaked angular intensity distribution.

A set of three benchmark-type problems is presented. The relative error introduced by some of the more popular angular approximations is found as a function of optical thickness and scattering albedo for each of the cases studied. This study is by no means exhaustive nor is it meant to establish which approximation is ‘best.’ The determination of which angular approximation to use is highly problem-dependent and is best made on a case-by-case basis. The hope is that Chapter 3 might be useful for analysts interested in the order of accuracy expected from each of these angular approximations in scenarios similar to the cases studied. It is the opinion of the author that a more extensive database of benchmark problems and solutions would benefit the community in verification and validation activities. A centralized repository of this information would also be beneficial.

Approximating the spectral distribution of the intensity is approached differently. Because the spectral absorption coefficient and intensity in molecular gases tend to be highly oscillatory and only the spectrally integrated intensity enters into the energy equation, calculation of the exact spectral intensity is considered over-kill for most

applications. Line-by-line solutions which provide a discrete representation of the spectral intensity are too computationally expensive to be practical for general engineering applications. Hundreds of thousands of spectral intervals are often required to achieve an accurate line-by-line solution.

In order to avoid this overwhelming computational expense, there have been numerous alternative methods developed. Narrow- and wide-band models involve choosing a set of wavelength intervals. Within each interval, ‘equivalent’ composite properties are defined. This is generally done by making assumptions about the shape, distribution, and magnitude of the absorption lines within each band. Narrow-band models may be too computationally expensive for some applications while wide-band models do not provide the same degree of accuracy as some other methods such as the full-spectrum k-distribution method.

The k-distribution method takes advantage of the fact that the same absorption coefficient value is reached many times over any sufficiently large spectral interval. Assuming that the absorption coefficient obeys the so-called scaling approximation, a reordering of the wavenumber space so that the absorption coefficient is a monotonically increasing function of the spectral variable is possible. Narrow band k-distribution methods involve performing this mapping within narrow spectral intervals. Within a small enough spectral interval, the scaling approximation is reasonable and the method converges towards the line-by-line solution. Unfortunately, narrow band k-distribution methods are computationally expensive due to the necessity of several gray gases within each spectral interval in addition to the offline computational cost of generating the k-distribution function for each spectral interval. Choosing wider bands can mitigate this computational expense. However, if the bands are too wide the scaling approximation may no longer be valid. The error associated with choosing bands which are too wide is

unknown although it may be approximated using an adaptation of the SFSK method described in Chapter 4.

The full-spectrum k-distribution (FSK) represents the limit of the wide-band k-distribution method as the band width approaches infinity. It treats the entire spectrum as a single band. The spectral reordering is global. The error is greater than that of the narrow band k-distribution method, but the computational cost is significantly less. The error is a result of inaccuracies in two approximations. The first approximation is the scaling approximation. In real gases, the spectral behavior of the absorption coefficient is not generally uniform across the domain if temperature, pressure, or concentration gradients are present. The second approximation involves the assumption of a spectral intensity distribution for the incident radiative flux. The second assumption usually produces small errors if a reasonable spectral distribution is chosen. A Planck distribution at an intermediate reference temperature is usually a good choice. Estimation of the error introduced by the k-distribution method may be approached in a couple of different ways.

In the MSFSK method, the error is estimated indirectly. Rather than approximating the dependence of the optical properties upon the state, the state itself is approximated. This circumvents the main problem associated with quantifying the error associated with the spectral integration. The MSFSK method provides a highly accurate solution to the approximate problem. The solution to the approximate problem converges to the solution of the actual problem in a predictable way which allows for error estimation and convergence analysis. However, the MSFSK method remains a computationally expensive method relative to other spectral integration techniques. Furthermore, the MSFSK method is currently restricted to 1-D applications. For 1-D applications with high demands for accuracy, the MSFSK method is a good choice.

However, the domain of applicability of the method is restrictive enough that its use is not generally advisable. Modifying the MSFSK method in order to extend its domain of applicability is an area of potential future research. For now, other less computationally expensive methods may provide similarly accurate solutions for more general problem spaces.

The FSK method has been shown to be exact for problems with homogeneous media [116]. It represents an inexpensive alternative to line-by-line or MSFSK method calculations. The FSK method is shown to produce errors when applied to media with temperature, pressure, or concentration gradients except in the case when the spectra remain correlated [110]. Unfortunately, real gas spectra tend not to be correlated across changes in temperature, pressure, or concentration. Some gases such as carbon dioxide have optical properties which are relatively insensitive to changes in pressure. Other gases such as water vapor are more sensitive to pressure variations.

When temperature, pressure, or concentration gradients are present, the FSK method produces errors. Errors due to the assumption of a correlated spectrum may be estimated by treating the gray-gas absorption coefficients found via the FSK method as uncertain parameters. Propagating this uncertainty to quantities of interest such as the heat flux or radiative flux divergence term in the energy equation requires the solution of the stochastic radiative transport equation. This results in the stochastic full spectrum k-distribution (SFSK) method. The SFSK method is stochastic rather than deterministic and as such produces a distribution for the quantity of interest rather than a single value. The expected value of the distribution predicted by the SFSK method is FSK prediction. The standard deviation of the SFSK prediction distribution represents a good error indicator for the FSK method.

The FSK method is a robust choice for approximating the spectrally integrated intensity. It provides significant computational savings when compared to line-by-line or MSFSK solutions. When uncertainty quantification is desired, confidence intervals for important quantities such as the heat flux or radiative flux divergence may be found via the SFSK method. This provides a cheaper and more widely applicable technique for estimating the error due to the spectral assumptions than has been previously developed. The development and demonstration of the SFSK method is in the author's view, the largest contribution of this work.

Much work remains in the development of the SFSK method before it may be more widely adopted. Its utility should be demonstrated in more complicated 2-D and 3-D geometries. This is a topic of current research. Empirical correlations should be developed for the mean, variance, and correlation function with respect to temperature, pressure, and concentration. Mixture rules should be developed for different combinations of combustion products. Empirical correlations such as those established for the FSK [115, 117, 133, 134] method would greatly enhance the usability of the SFSK method. The SFSK method potentially enjoys a wide domain of applicability and should be thoroughly tested for many additional applications prior to wider adoption.

## Appendix A

One of the most common schemes for developing sets for the discrete ordinates equation is the level symmetric scheme. If the weights and nodes are chosen to correctly integrate the maximum number of Legendre polynomials in each of the angular variables, the LQ<sub>N</sub> set shown below results.

<b>Level</b>	<b>n</b>	<b><math>\mu_n</math></b>	<b>w<sub>n</sub></b>
<b>S<sub>2</sub></b>	1	0.5773503	1
<b>S<sub>4</sub></b>	1	0.3500212	1/3
	2	0.8688903	
<b>S<sub>6</sub></b>	1	0.2666355	0.1761263
	2	0.6815076	0.1572071
	3	0.9261808	
<b>S<sub>8</sub></b>	1	0.2182179	0.1209877
	2	0.5773503	0.0907407
	3	0.7867958	0.0925926
	4	0.9511897	
<b>S<sub>12</sub></b>	1	0.1672126	0.0707626
	2	0.4595476	0.0558811
	3	0.6280191	0.0373377
	4	0.7600210	0.0502819
	5	0.8722706	0.0258513
	6	0.9716377	
<b>S<sub>16</sub></b>	1	0.1389568	0.0489872
	2	0.3922893	0.0413296
	3	0.5370966	0.0212326
	4	0.6504264	0.0256207
	5	0.7467506	0.0360486
	6	0.8319966	0.0144589
	7	0.9092855	0.0344958
	8	0.9805009	0.0085179

## Appendix B

A wide variety of flux limiters have been proposed and used in the literature. There are doubtless many more that have been used in general practice without publication. A partial list is provided below.

ALEGRA	$\lambda(R) = \frac{2+R}{6+3R+R^2}$
Kershaw	$\lambda(R) = \frac{2}{3+\sqrt{9+4R^2}}$
Levermore (Chapman-Enskog)	$\lambda(R) = \frac{1}{R} \left( \coth R - \frac{1}{R} \right)$
Levermore (Lorentz) <sup>1</sup>	$\lambda = \frac{3(1-\beta^2)^2}{(3+\beta^2)^2}$ $R = \frac{4\beta(3+\beta^2)}{3(1-\beta^2)^2}$
Minerbo (Max Entropy)	$\lambda = \frac{1}{z^2} - \operatorname{csch}^2 z$ $R = \frac{\coth z - \frac{1}{z}}{\frac{1}{z^2} - \operatorname{csch}^2 z}$
Minerbo (Linear)	$\lambda(R) = \begin{cases} \frac{2}{3+\sqrt{9+12R^2}}, & R < 3/2 \\ \frac{1}{1+R+\sqrt{1+2R}}, & R \geq 3/2 \end{cases}$
Pomraning <sup>2</sup>	$\lambda(R) = \frac{1+0.1440R}{3+1.0320R+0.1440R^2}$
Wilson	$\lambda(R) = \frac{1}{3+R}$
Winslow (Cut-Off)	$\lambda(R) = \begin{cases} 1/3, & R < 3 \\ 1/R, & R \geq 3 \end{cases}$

---

<sup>1</sup> This equation includes a typo in the original paper [40] which has propagated through the literature [64] but is corrected here.

<sup>2</sup> This is a rational fit proposed for the Levermore (Lorentz) flux-limiter.

## Appendix C

Definitions of fields provided in HITRAN database

Parameter	Meaning	Length	Type	Comments or Units
$M$	Molecule	2	Integer	
$I$	Isotopologue	1	Integer	
$v$	Wavenumber	12	Real	$\text{cm}^{-1}$
$S$	Intensity	10	Real	$\text{cm}^{-1} / (\text{molecule cm}^{-2})$
$A$	Einstein A-coefficient	10	Real	$\text{s}^{-1}$
$\gamma_{\text{air}}$	Air-broadened half-width	5	Real	$\text{cm}^{-1} \text{ atm}^{-1}$
$\gamma_{\text{self}}$	Self-broadened half-width	5	Real	$\text{cm}^{-1} \text{ atm}^{-1}$
$E''$	Lower-state energy	10	Real	$\text{cm}^{-1}$
$n_{\text{air}}$	Temperature-dependence exponent for $\gamma_{\text{air}}$	4	Real	unitless
$\delta_{\text{air}}$	Air pressure-induced line shift	8	Real	$\text{cm}^{-1} \text{ atm}^{-1}$
$V'$	Upper-state “global” quanta	15	Hollerith	
$V''$	Lower-state “global” quanta	15	Hollerith	
$Q'$	Upper-state “local” quanta	15	Hollerith	
$Q''$	Lower-state “local” quanta	15	Hollerith	
Ierr	Uncertainty indices	6	Integer	
Iref	Reference indices	12	Integer	
*	Flag	1	Character	
$g'$	Upper state statistical weight	7	Real	
$g''$	Lower state statistical weight	7	Real	

## References

- [1] P. J. Coelho, "On the Convergence of the Discrete Ordinates and Finite Volume Methods for the Solution of the Radiative Transfer Equation," in *ASME Verification and Validation Symposium*, Las Vegas, NV, 2013.
- [2] M. T. Heath, Scientific Computing, an Introductory Survey, New York, NY: McGraw-Hill, 2005.
- [3] W. Cheney and D. Kincaid, Numerical Mathematics and Computing, Belmont, CA: Thomson Brooks/Cole, 2008.
- [4] P. Moin, Fundamentals of Engineering Numerical Analysis, New York, NY: Cambridge University Press, 2010.
- [5] J. C. Chai and P. Rath, "Discrete-Ordinates and Finite-Volume Methods for Radiation Heat Transfer," in *Treatment of Thermal Radiation in Heat Transfer Problems*, Guwahati, India, IIT, 2006.
- [6] G. D. Raithby, "Discussion of the Finite-Volume Method for Radiation, and its Application Using 3D Unstructured Meshes," in *Numerical Heat Transfer, Part B*, Taylor & Francis, 1999, pp. 389-405.
- [7] R. D. Russell and L. F. Shampine, "A collocation method for boundary value problems," *Numerische Mathematik*, vol. 19, no. 1, pp. 1-28, 1972.
- [8] H.-Y. Hu and Z.-C. Li, "Combinations of Collocation and Finite-Element Methods for Poisson's Equation," *Computers and Mathematics with Applications*, vol. 51, pp. 1831-1853, 2006.
- [9] A. J. Perella, A class of Petrov-Galerkin finite element methods for the numerical solution of the stationary convection-diffusion equation, Doctoral Thesis, Durham University, 1996.
- [10] M. A. Olshanskii, "A low order Galerkin finite element method for the Navier-Stokes equations of steady incompressible flow: a stabilization issue and iterative methods," *Comput. Methods Appl. Mech. Engrg*, vol. 191, p. 5515–5536, 2002.
- [11] A. N. Brooks and T. J. R. Hughes, "Streamline Upwind/Petrov-Galerkin Formulations for Convection Dominated Flows with Particular Emphasis on the Incompressible Navier-Stokes Equations," *Computer Methods in Applied Mathematics and Engineering*, vol. 32, pp. 199-259, 1982.
- [12] J. Tencer and J. R. Howell, "A Parametric Study of the Accuracy of Several Radiative Transport Solution Methods for a Set of 2-D Benchmark Problems," in *ASME Summer Heat Transfer Conference*, Minneapolis, MN, 2013.
- [13] W. A. Fiveland, "Three-Dimensional Radiative Heat-Transfer Solutions by the Discrete-Ordinates Method," *J. Thermophysics*, vol. 2, no. 4, pp. 309-316, 1988.
- [14] W. A. Fiveland, "Discrete-Ordinates Solutions of the Radiative Transport Equation for Rectangular Enclosures," *ASME Transactions Journal of Heat Transfer*, vol.

- 106, pp. 699-706, 1984.
- [15] W. A. Fiveland, "Discrete Ordinate Methods for Radiative Heat Transfer in Isotropically and Anisotropically Scattering Media," *ASME Journal of Heat Transfer*, vol. 109, no. 3, 1987.
  - [16] R. Koch and R. Becker, "Evaluation of quadrature schemes for the discrete ordinates method," *Journal of Quantitative Spectroscopy & Radiative Transfer*, vol. 84, pp. 423-435, 2004.
  - [17] R. Koch, W. Krebs, S. Wittig and R. Viskanta, "Discrete Ordinates Quadrature Schemes for Multidimensional Radiative Transfer," *J. Quant. Spectrosc. Radiat. Transfer*, vol. 53, no. 4, pp. 252-372, 1995.
  - [18] S. A. Rukolaine and V. S. Yuferev, "Discrete ordinates quadrature schemes based on the angular interpolation of radiation intensity," *J. Quant. Spectrosc. Radiat. Transfer*, vol. 69, pp. 257-275, 2001.
  - [19] E. E. Lewis and W. F. Miller, Jr., *Computational Methods of Neutron Transport*, La Grange Park, Illinois: American Nuclear Society, Inc., 1993.
  - [20] W. A. Fiveland and J. P. Jessee, "Acceleration Schemes for the Discrete Ordinates Method," *Journal of Thermophysics and Heat Transfer*, vol. 10, no. 3, pp. 445-451, 1996.
  - [21] G. D. Raithby and E. H. Chui, "Accelerated Solution of the Radiation-Transfer Equation with Strong Scattering," *Journal of Thermophysics and Heat Transfer*, vol. 18, no. 4, pp. 156-159, 2004.
  - [22] H.-M. Koo, H. Cha and T.-H. Song, "Convergence Characteristics of Temperature in Radiation Problems," *Numerical Heat Transfer, Part B: An International Journal of Computation and Methodology*, vol. 40, no. 4, pp. 303-324, 2001.
  - [23] J. Y. Murthy and S. R. Mathur, "Finite Volume Method for Radiative Heat Transfer Using Unstructured Meshes," *Journal of Thermophysics and Heat Transfer*, vol. 12, no. 3, 1998.
  - [24] S. H. Kang and T.-H. Song, "Finite element formulation of the first- and second-order discrete ordinates equations for radiative heat transfer calculation in three-dimensional participating media," *Journal of Quantitative Spectroscopy & Radiative Transfer*, vol. 109, pp. 2094-2107, 2008.
  - [25] F. Asllanaj, V. Feldheim and P. Lybaert, "Solution of Radiative Heat Transfer in 2-D Geometries by a Modified Finite-Volume Method Based on a Cell Vertex Scheme Using Unstructured Triangular Meshes," *Numerical Heat Transfer, Part B*, vol. 51, pp. 97-119, 2007.
  - [26] B. G. Carlson and K. D. Lathrop, "Transport Theory - The Method of Discrete Ordinates," *Computing Methods in Reactor Physics*, 1968.
  - [27] B. G. Carlson, "On a More Precise Definition of Discrete Ordinates Methods," in *Proc. Second Conf. Transport Theory*, Los Alamos, N.M., 1971.
  - [28] B. G. Carlson, "Transport Theory: Discrete Ordinates Quadrature over the Unit

- Sphere," Los Alamos Scientific Laboratory, Los Alamos, N.M., 1970.
- [29] B. G. Carlson and C. E. Lee, "Mechanical Quadrature and the Transport Equation," Los Alamos Scientific Laboratory, Los Alamos, NM, 1961.
  - [30] K. D. Lathrop and B. G. Carlson, "Discrete Ordinates Angular Quadrature of the Neutron Transport Equation," Los Alamos Scientific Laboratory, 1965.
  - [31] C. E. Lee, "Discrete SN Approximation to Transport Theory," Los Alamos Scientific Laboratory, Los Alamos, NM, 1962.
  - [32] C. Thurgood, A. Pollard and P. Rubini, "Development of TN Quadrature Sets and HEART Solution Method for Calculating Radiative Heat Transfer," in *Int. Symp. on Steel Reheat Furnace Technology*, Hamilton, Ontario, Canada, 1990.
  - [33] J. J. Jarell, An adaptive angular discretization method for neutral-particle transport in three-dimensional geometries, Ph.D Dissertation, College Station, TX: Texas A&M University, 2010.
  - [34] G. Longoni, Advanced quadrature sets, acceleration and preconditioning techniques for the discrete ordinates method in parallel computing environments, Ph.D Dissertation, Gainesville, FL: University of Florida, 2004.
  - [35] S. H. Kim and K. Y. Huh, "A New Angular Discretization Scheme of the Finite Volume Method for 3-D Radiative Heat Transfer in Absorbing, Emitting and Anisotropically Scattering Media," *International Journal of Heat and Mass Transfer*, vol. 43, pp. 1233-1242, 2000.
  - [36] B.-W. Li, J.-H. Zhou, X.-Y. Cao, H.-G. Chen and K.-F. Cen, "The Spherical Surface Symmetrical Equal Dividing Angular Quadrature Scheme for Discrete Ordinates Method," *ASME Journal of Heat Transfer*, vol. 124, no. 3, pp. 482-490, 2002.
  - [37] A. L. Crosbie and R. G. Schrenker, "Radiative transfer in a two-dimensional rectangular medium exposed to diffuse radiation," *J. Quant. Spectrosc. Radiat. Transfer*, vol. 31, no. 4, pp. 339-372, 1984.
  - [38] Z. Altac and M. Tekkalmaz, "Solution of the radiative integral transfer equations in rectangular participating and isotropically scattering inhomogeneous medium," *International Journal of Heat and Mass Transfer*, vol. 47, pp. 101-109, 2004.
  - [39] G. N. Minerbo, "Maximum Entropy Eddington Factors," *J. Quant. Spectrosc. Radiat. Transfer*, vol. 20, pp. 541-545, 1978.
  - [40] C. D. Levermore, "Relating Eddington Factors to Flux Limiters," *J. Quant. Spectrosc. Radiat. Transfer*, vol. 31, no. 2, pp. 149-160, 1984.
  - [41] D. S. Kershaw, "Flux Limiting Nature's Own Way," Lawrence Livermore National Laboratory, Livermore, CA, 1976.
  - [42] T. A. Brunner and J. P. Holloway, "One-dimensional Riemann Solvers and the Maximum Entropy Closure," *J. Quant. Spectrosc. Radiat. Transfer*, vol. 69, pp. 543-566, 2001.

- [43] K. A. Jensen, J.-F. Ripoll, A. A. Wray, D. Joseph and M. El Hafi, "On various modeling approaches to radiative heat transfer in pool fires," *Combustion and Flame*, vol. 148, pp. 263-279, 2007.
- [44] G. L. Olson, L. H. Auer and M. L. Hall, "Diffusion, P1, and other approximate forms of radiation transport," *J. Quant. Spectrosc. Radiat. Transfer*, vol. 64, pp. 619-634, 2000.
- [45] J. -F. Ripoll, "An averaged formulation of the M1 radiation model with mean absorption coefficients and presumed probability density function for turbulent flows," *J. Quant. Spectrosc. Radiat. Transfer*, vol. 83, pp. 493-517, 2004.
- [46] J. -F. Ripoll and A. A. Wray, "A half-moment model for radiative transfer in a 3D gray medium and its reduction to a moment model for hot, opaque sources," *J. Quant. Spectrosc. Radiat. Transfer*, vol. 93, pp. 473-519, 2005.
- [47] A. L. Brown and F. Pierce, "The M1 model: evaluation for predicting thermal radiation from fires," in *ASME 2012 Summer Heat Transfer Conference*, Puerto Rico, USA, 2012.
- [48] T. A. Brunner, *Riemann Solvers for Time-Dependent Transport Based on the Maximum Entropy and Spherical Harmonics Closures*, 2000.
- [49] G. C. Pomraning, "Flux Limiters and Eddington Factors," *J. Quant. Spectrosc. Radiat. Transfer*, vol. 27, no. 5, pp. 517-530, 1982.
- [50] C. D. Levermore and G. C. Pomraning, "A Chapman-Enskog Approach to Flux-Limited Diffusion Theory," *Astrophysical J.*, vol. 248, p. 321, 1981.
- [51] G. C. Pomraning, *J. Quant. Spectrosc. Radiat. Transfer*, vol. 26, p. 385, 1981.
- [52] M. F. Modest and J. Yang, "Elliptic PDE Formulation and Boundary Conditions of the Spherical Harmonics Method of Arbitrary Order for General Three-Dimensional Geometries," *J. Quant. Spectrosc. Radiat. Transf.*, vol. 109, pp. 1641-1666, 2008.
- [53] A. C. Ratzel, P-N Differential Approximation for Solution of One- and Two-Dimensional Radiation and Conduction Energy Transfer in Gray Participating Media, Dissertation, Austin, TX: University of Texas at Austin, 1981.
- [54] G. I. Marchuk and V. I. Lebedev, Numerical Methods in the Theory of Neutron Transport, Chur, Switzerland: Hardwood Academic Publishers, 1986.
- [55] A. C. Ratzel III and J. R. Howell, "Two-Dimensional Radiation in Absorbing-Emitting Media Using the P-N Approximation," *J. Heat Transfer*, vol. 105, no. 2, 1983.
- [56] J. Cai and M. Modest, "Comparisons of Radiative Heat Transfer Calculations Using Spherical Harmonics and k-Distributions," in *ASME Summer Heat Transfer Conference*, Minneapolis, MN, 2013.
- [57] B. Davison, Neutron Transport Theory, London: Oxford Press, 1958.
- [58] T. M. MacRobert, Spherical Harmonics, 3rd ed., New York: Pergamon Press, 1967.

- [59] J. C. Mark, "The spherical harmonics method, part I. Technical Report, Atomic Energy Report No. MT 92," National Research Council of Canada, 1944.
- [60] J. C. Mark, "The spherical harmonics method, Part II. Technical Report, Atomic Energy Report No. MT 97," National Research Council of Canada, 1945.
- [61] R. E. Marshak, "Note on the spherical harmonics method as applied to the Milne problem for a sphere," *Phys Rev*, vol. 71, pp. 443-446, 1947.
- [62] M. F. Modest, Radiative Heat Transfer, New York: McGraw-Hill, Inc., 1993.
- [63] M. Ravishankar, Spherical Harmonics Based Techniques for Solution of the Radiative Transfer Equation, Master's Thesis, Columbus, Ohio: The Ohio State University, 2009.
- [64] M. Frank, "Approximate Models for Radiative Transfer," *Bulletin of the Institute of Mathematics*, vol. 2, no. 2, pp. 409-432, 2007.
- [65] E. M. Gelbard, "Simplified Spherical Harmonics Equations and Their Use in Shielding Problems, Technical Report WAPD-T-1182," Bettis Atomic Power Laboratory, 1961.
- [66] M. F. Modest and S. Lei, "The Simplified Spherical Harmonics Method for Radiative Heat Transfer," in *Eurotherm Conference No. 95: Computational Thermal Radiation in Participating Media IV*, Nancy, France, 2012.
- [67] E. Larsen, J. Morel and J. McGhee, "Simplified PN Approximations to the Equations of Radiative Heat Transfer and Applications," in *Proceedings of the Joint International Conference on Mathematical Methods and Supercomputing in Nuclear Applications*, Portland, Oregon, 1993.
- [68] J. E. Morel, J. M. McGhee and E. W. Larsen, "A 3-D Time-Dependent Unstructured Tetrahedral-Mesh SPn Method," *Nuclear Science and Engineering*, vol. 123, pp. 319-327, 1996.
- [69] D. Mihalas and B. W. Mihalas, Foundations of Radiation Hydrodynamics, Oxford: Oxford University Press, 1984.
- [70] J. E. Morel, *A Grey SPN Infrared Transfer Formulation, Research Memo*, 2008.
- [71] H. Zheng and W. Han, "On Simplified Spherical Harmonics Equations for the Radiative Transfer Equation," *J Math Chem*, vol. 49, pp. 1785-1797, 2011.
- [72] M. Seaid, "Multigrid Newton-Krylov Method for Radiation in Diffusive Semitransparent Media," *Journal of Computational and Applied Mathematics*, vol. 203, pp. 498-515, 2007.
- [73] G. C. Pomraning, "Asymptotic and Variational Derivations of the Simplified Pn Equations," *Ann. Nuclear Energy*, vol. 20, p. 623, 1993.
- [74] E. W. Larsen, G. Thommes, A. Klar, M. Seaid and T. Gotz, "Simplified Pn Approximations to the Equations of Radiative Heat Transfer and Applications," *Journal of Computational Physics*, vol. 183, pp. 652-675, 2002.
- [75] A. Klar, J. Lang and M. Seaid, "Adaptive Solutions of SPN-Approximations to

- Radiative Heat Transfer in Glass," *International Journal of Thermal Sciences*, vol. 44, pp. 1013-1023, 2005.
- [76] A. D. Klose and E. W. Larsen, "Light Transport in Biological Tissue Based on the Simplified Spherical Harmonics Equations," *Journal of Computational Physics*, vol. 220, pp. 441-470, 2006.
  - [77] R. Ciolini, G. Coppa, B. Montagnini and P. Ravetto, "Simplified PN and AN Method in Neutron Transport," *Progress in Nuclear Energy*, vol. 40, no. 2, pp. 237-264, 2002.
  - [78] P. S. Brantley and E. W. Larsen, "The Simplified P3 Approximation," *Nuclear Science and Engineering*, vol. 134, pp. 1-21, 2000.
  - [79] D. I. Tomasevic and E. W. Larsen, "The Simplified P2 Approximation," *Nuclear Science and Engineering*, vol. 122, pp. 309-325, 1996.
  - [80] J. E. Morel, T. A. Wareing, R. B. Lowrie and D. K. Parsons, "Analysis of Ray-Effect Mitigation Techniques," *Nuclear Science and Engineering*, vol. 144, no. 1, pp. 1-22, 2003.
  - [81] W. A. Fiveland and J. P. Jessee, "Comparison of Discrete Ordinates Formulations for Radiative Heat Transfer in Multidimensional Geometries," *Journal of Thermophysics and Heat Transfer*, vol. 9, no. 1, pp. 47-54, 1995.
  - [82] L. S. Rothman, D. Jacquemart, A. Barbe, D. C. Benner, M. Birk, L. R. Brown, M. R. Carleer, C. Chackerian Jr., K. Chance, L. H. Coudert, V. Dana, V. M. Devi, J. M. Flaud, R. R. Gamache, A. Goldman, J. M. Hartmann, K. W. Jucks, A. G. Maki, J. Y. Mandin, S. T. Massie, J. Orphal, A. Perrin, C. P. Rinsland, M. A. H. Smith, J. Tennyson, R. N. Tolchenov, R. A. Toth, J. V. Auwera, P. Varanasi and G. Wagner, "The HITRAN 2004 molecular spectroscopic database," *Journal of Quantitative Spectroscopy & Radiative Transfer*, vol. 96, p. 139–204, 2005.
  - [83] L. S. Rothman, I. E. Gordon, R. J. Barber, H. Dothe, R. R. Gamache, A. Goldman, V. I. Perevalov, S. A. Tashkun and J. Tennyson, "HITEMP, the high-temperature molecular spectroscopic database," *Journal of Quantitative Spectroscopy and Radiative Transfer*, vol. 111, no. 15, pp. 2139-2150, 2010.
  - [84] L. S. Rothman, , I. E. Gordon, Y. Babikov, A. Barbe, C. D. Benner, P. F. Bernath, M. Birk, L. Bizzocchi, V. Boudon, L. R. Brown, A. Campargue, K. Chance, E. A. Cohen, L. H. Coudert, V. M. Devi, B. J. Drouin, A. Fayt, J. -M. Flaud, R. R. Gamache, J. J. Harrison, J. -M. Hartmann, C. Hill, J. T. Hodges, D. Jacquemart, A. Jolly, J. Lamouroux, R. J. Le Roy, G. Li, D. A. Long, O. M. Lyulin, C. J. Mackie, S. T. Massie, S. Mikhailenko, H. S. P. Muller, O. V. Naumenko, A. V. Nikitin, J. Orphal, V. Perevalov, A. Perrin, E. R. Polovtseva, C. Richard, M. A. H. Smith, E. Starikova, K. Sung, S. Tashkun, J. Tennyson, G. C. Toon, V. G. Tyuterev and G. Wagner, "The HITRAN2012 molecular spectroscopic database," *J Quant Spectrosc Radiat Transfer (2013)*, <http://dx.doi.org/10.1016/j.jqsrt.2013.07.002i>.
  - [85] J. Fischer, R. R. Gamache, A. Goldman, L. S. Rothman and A. Perrin, "Total internal partition sums for molecular species on the 2000 edition of the HITRAN

- database," *Journal of Quantitative Spectroscopy and Radiative Transfer*, vol. 82, pp. 401-412, 2003.
- [86] A. Goldman, R. R. Gamache, A. Perrin, J. M. Flaud, C. P. Rinsland and L. S. Rothman, "HITRAN partition functions and weighted transition probabilities," *Journal of Quantitative Spectroscopy and Radiative Transfer*, vol. 66, pp. 455-486, 2000.
  - [87] J. T. Pearson, B. W. Webb, V. P. Solovjov and J. Ma, "Impact of Variable Pressure on the Absorption Line Blackbody Distribution Function and Radiative Transfer in H<sub>2</sub>O, CO<sub>2</sub>, and CO," in *Proceedings of the 7th International Symposium on Radiative Transfer, RAD-13*, Kusadasi, Turkey, 2013.
  - [88] A. Wang and M. F. Modest, "Importance of Combined Lorentz-Doppler Broadening in High-Temperature Radiative Heat Transfer Applications," *ASME J. Heat Transfer*, vol. 126, pp. 858-861, 2004.
  - [89] R. Siegel and J. R. Howell, *Thermal Radiation Heat Transfer*, 5th ed., New York: Taylor & Francis, 2011.
  - [90] W. Malkmus, "Random Lorentz Band Model with Exponential-Tailed S-1 Line Intensity Distribution Function," *JOSA*, vol. 57, no. 3, pp. 323-329, 1967.
  - [91] D. K. Edwards and W. A. Menard, "Comparison of Models for Correlation of Total Band Absorption," *Appl. Opt.*, vol. 3, no. 5, pp. 621-625, 1964.
  - [92] D. K. Edwards, "Radiant Interchange in a Nongray Enclosure Containing an Isothermal Carbon Dioxide-Nitrogen Gas Mixture," *J. Heat Transfer*, vol. 84, no. 1, pp. 1-11, 1962.
  - [93] D. K. Edwards, "Absorption of Infrared Bands of Carbon Dioxide Gas at Elevated Pressures and Temperatures," *J. Opt. Soc. Am.*, vol. 50, no. 6, pp. 617-626, 1960.
  - [94] D. K. Edwards and W. A. Menard, "Correlations for Absorption by Methane and Carbon Dioxide Gases," *Appl. Opt.*, vol. 3, no. 7, pp. 847-852, 1964.
  - [95] D. K. Edwards and W. Sun, "Correlations for Absorption by the 9.4- $\mu$  and 10.4- $\mu$  CO<sub>2</sub> Bands," *Appl. Opt.*, vol. 3, no. 12, pp. 1501-1502, 1964.
  - [96] D. K. Edwards, B. J. Flornes, L. K. Glassen and W. Sun, "Correlation of Absorption by Water Vapor at Temperatures from 300 K to 1100 K," *Appl. Opt.*, vol. 4, no. 6, pp. 715-721, 1965.
  - [97] D. K. Edwards, "Absorption of Radiation by Carbon Monoxide Gas According to the Exponential Wide-Band Model," *Appl. Opt.*, vol. 4, no. 10, pp. 1352-1353, 1965.
  - [98] D. K. Edwards and A. Balakrishnan, "Thermal Radiation by Combustion Gases," *Int. J. Heat Mass Transfer*, vol. 16, no. 1, pp. 25-40, 1973.
  - [99] M. K. Denison and B. W. Webb, "A Spectral Line-Based Weighted-Sum-of-Gray-Gases Model for Arbitrary RTE Solvers," *ASME Journal of Heat Transfer*, vol. 115, pp. 1004-1012, 1993.

- [100] V. P. Solovjov and B. W. Webb, "SLW modeling of radiative transfer in multicomponent gas mixtures," *Journal of Quantitative Spectroscopy & Radiative Transfer*, vol. 65, pp. 655-672, 2000.
- [101] V. P. Solovjov and B. W. Webb, "Multilayer Modeling of Radiative Transfer by SLW and CW Methods in Non-Isothermal Gaseous Medium," *Journal of Quantitative Spectroscopy and Radiative Transfer*, pp. 245-257, 2008.
- [102] V. P. Solovjov and B. W. Webb, "Application of CW local correction approach to SLW modeling of radiative transfer in non-isothermal gaseous media," *Journal of Quantitative Spectroscopy & Radiative Transfer*, vol. 111, pp. 318-324, 2010.
- [103] V. P. Solovjov, D. Lemonnier and B. W. Webb, "The SLW-1 model for efficient prediction of radiative transfer in high temperature gases," *Journal of Quantitative Spectroscopy & Radiative Transfer*, vol. 112, pp. 1205-1212, 2011.
- [104] V. P. Solovjov and B. B. Webb, "A local-spectrum correlated model for radiative transfer in non-uniform gas media," *Journal of Quantitative Spectroscopy & Radiative Transfer*, vol. 73, pp. 361-373, 2002.
- [105] V. P. Solovjov and B. W. Webb, "The cumulative wavenumber method for modeling radiative transfer in gas mixtures with soot," *Journal of Quantitative Spectroscopy & Radiative Transfer*, vol. 93, pp. 273-287, 2005.
- [106] S. Mazumder and M. F. Modest, "Application of the Full Spectrum Correlated-k Distribution Approach to Modeling Non-Gray Radiation in Combustion Gases," *Combustion and Flame*, vol. 129, pp. 416-438, 2002.
- [107] D. T. Pawlak, E. E. Clothiaux, M. F. Modest and J. N. Cole, "Full-Spectrum Correlated-k Distribution for Shortwave Atmospheric Radiative Transfer," *Journal of the Atmospheric Sciences*, vol. 61, pp. 2588-2601, 2004.
- [108] D. T. Pawlak, Development and Evaluation of a Shortwave Full-Spectrum Correlated k-Distribution Radiative Transfer Algorithm for Numerical Weather Prediction, Ph.D Dissertation, Pennsylvania State University, 2004.
- [109] A. Wang and M. F. Modest, "High-accuracy, compact database of narrow-band k-distributions for water vapor and carbon dioxide," *Journal of Quantitative Spectroscopy & Radiative Transfer*, vol. 95, pp. 245-261, 2005.
- [110] M. F. Modest and H. Zhang, "The Full-Spectrum Correlated-k Distribution for Thermal Radiation From Molecular Gas-Particulate Mixtures," *J. Heat Transfer*, p. 30, 2002.
- [111] R. Goody, R. West, L. Chen and D. Crisp, "The Correlated-k Method for Radiation Calculations in Nonhomogeneous Atmospheres," *J. Quant. Spectrosc Radiat. Transf.*, pp. 539-550, 1989.
- [112] A. A. Lacis and V. Oinas, "A Description of the Correlated-k Distribution Method for Modeling Nongray Gaseous Absorption, Thermal Emission, and Multiple Scattering in Vertically Inhomogeneous Atmospheres," *Journal of Geophysical Research*, pp. 2139-2156, 1991.

- [113] A. Maurente, F. H. R. Franca, K. Miki and J. R. Howell, "Application of Joint Cumulative k-Distributions to FSK Radiation Heat Transfer in Multi-component High Temperature Non-LTE Plasmas," *J. Quant. Spectr. & Rad. Trans.*, vol. 113, no. 12, pp. 1521-1535, 2012.
- [114] G. Pal, M. F. Modest and L. Wang, "Hybrid Full-Spectrum Correlated k-Distribution Method for Radiative Transfer in Strongly Nonhomogeneous Gas Mixtures," *ASME Journal of Heat Transfer*, 2008.
- [115] J. T. Pearson, B. W. Webb, V. P. Solovjov and J. Ma, "Updated correlation of the absorption line blackbody distribution function for H<sub>2</sub>O based on the HITEMP2010 database," in *EUROTHERM SEMINAR No. 95 Computational Thermal Radiation in Participating Media IV*, Nancy, France, 2012.
- [116] M. F. Modest and H. Zhang, "The Full-Spectrum Correlated-k Distribution for Thermal Radiation From Molecular Gas-Particulate Mixtures," *ASME Journal of Heat Transfer*, 2002.
- [117] M. F. Modest and R. S. Mehta, "Full spectrum k-distribution correlations for CO<sub>2</sub> from the CDSD-1000 spectroscopic databank," *International Journal of Heat and Mass Transfer*, vol. 47, pp. 2487- 2492, 2004.
- [118] H. Zhang and M. F. Modest, "Scalable Multi-Group Full-Spectrum Correlated-k Distributions for Radiative Transfer Calculations," *ASME Journal of Heat Transfer*, 2003.
- [119] P. Riviere, A. Soufiani and J. Taine, "Correlated-k and Fictitious Gas Methods for H<sub>2</sub>O Near 2.7 mm," *J Quant. Spectrosc. Radiat. Transf.*, pp. 187-203, 1992.
- [120] J. Taine and A. Soufianai, "Gas IR Radiative Properties: From Spectroscopic Data to Approximate Models," *Advances in Heat Transfer*, pp. 295-414, 1999.
- [121] P. Riviere, A. Soufiani and J. Taine, "Correlated-k and Fictitious Gas Model for H<sub>2</sub>O Infrared Radiation in the Voigt Regime," *J. Quant. Spectrosc. Radiat. Transf.*, pp. 335-346, 1995.
- [122] J. Tencer and J. R. Howell, "A Multi-Source Full Spectrum K-Distribution Method for 1-D Inhomogeneous Media," in *Eurotherm Conference No. 95: Computational Thermal Radiation in Participating Media IV*, Journal of Physics: Conference Series 369, 2012.
- [123] J. T. Tencer, "The K-Distribution Method for Radiation Heat Transfer in Non-Isothermal Real Air-Gas Plasmas," *Master's thesis, Mechanical Eng., University of Texas, Austin, TX*, 2011.
- [124] J. Tencer and J. R. Howell, "On Multilayer modeling of radiative transfer for use with the multi-source k-distribution method for inhomogeneous media," in *Proc. ASME 2012 Heat Transfer Conference*, Rio Grande, Puerto Rico, 2012.
- [125] J. Tencer and J. R. Howell, "A multi-source full spectrum k-distribution method for 1-D inhomogeneous media," *J. Quant Spectrosc Radiat Transfer (2013)*, <http://dx.doi.org/10.1016/j.jqsrt.2013.07.008i>.

- [126] J. Tencer and J. R. Howell, "Quantification of Model-Form Uncertainty in the Correlated-k Distribution Method for Radiation Heat Transfer," in *ICHMT 7th International Symposium on Radiative Transfer, RAD-13*, Kusadasi, Turkey, 2013.
- [127] H. Zhang and M. F. Modest, "A Multi-Scale Full-Spectrum Correlated-k Distribution for Radiative Heat Transfer in Inhomogeneous Gas Mixtures," *Journal of Quantitative Spectroscopy and Radiative Transfer*, vol. 73, no. 2-5, pp. 349-360, 2002.
- [128] L. Wang and M. F. Modest, "Treatment of Wall Emission in the Narrow-Band Based Multi-Scale Full-Spectrum k-Distribution Method," *ASME Journal of Heat Transfer*, vol. 129, no. 6, pp. 743-748, 2007.
- [129] R. T. Clemen and T. Reilly, "Correlations and Copulas for Decision and Risk Analysis," *Management Science*, vol. 45, no. 2, pp. 208-224, 1999.
- [130] R. R. Nelsen, *An Introduction to Copulas*, New York: Springer, 1999.
- [131] E. Bouye, V. Durrleman, A. Nikeghbali, G. Riboulet and T. Roncalli, "Copulas for Finance - A Reading Guide and Some Applications," *Groupe de Recherche Opérationnelle, Crédit Lyonnais*, Paris, 2000.
- [132] G. G. M. Coppa, V. Giusti, B. Montagnini and P. Ravetto, "On the Relation Between Spherical Harmonics and Simplified Spherical Harmonics Methods," *Transport Theory and Statistical Physics*, vol. 39, pp. 164-191, 2011.
- [133] H. Zhang and M. F. Modest, "Full-Spectrum k-Distribution Correlations for Carbon Dioxide Mixtures," *Journal of Thermophysics and Heat Transfer*, vol. 17, no. 2, pp. 259-263, 2003.
- [134] M. F. Modest and V. Singh, "Engineering Correlations for Full Spectrum k-Distribution of H<sub>2</sub>O from the HITEMP Spectroscopic Databank," *Journal of Quantitative Spectroscopy and Radiative Transfer*, vol. 93, pp. 263-271, 2005.